Department of Physics
Indian Institute of Technology Guwahati
Ph.D. Thesis

PROPERTIES OF BAND-ENGINEERED TOPOLOGICAL SYSTEMS IN TWO DIMENSIONS

Sayan Mondal

Supervisor: ***Prof. Saurabh Basu***

PROPERTIES OF BAND-ENGINEERED TOPOLOGICAL SYSTEMS IN TWO DIMENSIONS

Sayan Mondal
Roll No.- 186121022

Supervisor: Prof. Saurabh Basu

A Thesis Presented to the
Department of Physics
of
Indian Institute of Technology Guwahati
in Partial Fulfillment of the Requirements for the Degree of
Doctor of Philosophy in Physics

Department of Physics
Indian Institute of Technology Guwahati
Guwahati - 781039, Assam, India

Statement

The work contained in the thesis entitled "*Properties of Band-Engineered Topological Systems in Two Dimensions*" has been carried out at the Department of Physics, Indian Institute of Technology Guwahati, India by me under the supervision of Prof. Saurabh Basu. The material of this thesis has not been submitted elsewhere for any other degree. Works presented in the thesis are all my own unless referenced to the contrary in the text.

Sayan Mondal 7/7/2023

(Sayan Mondal) July 7, 2023
Department of Physics
Indian Institute of Technology Guwahati
Guwahati - 781039, India

Disclaimer

The bibliography included in this thesis is, by no means complete but contains the ones which are consulted thoroughly by me. I apologize for inadvertently missing out some of the research papers, review articles and other scientific documents pertaining to the focus of this thesis which should also have been cited. For illustration purpose some of the figures in this thesis are taken from other sources and properly cited.

Certificate

It is certified that the work contained in the thesis entitled "*Properties of Band-Engineered Topological Systems in Two Dimensions*" by Mr. Sayan Mondal, a Ph.D. student of the Department of Physics, Indian Institute of Technology Guwahati is carried out under my supervision and has not been submitted elsewhere for the award of any other degree.

Saurabh Basu 7/7/2023

(Prof. Saurabh Basu) July 7, 2023
Department of Physics
Indian Institute of Technology Guwahati
Guwahati - 781039, India

Dedicated to my beloved

parents and sister

&

the cherished memory of my

late grandmother and uncle.

Acknowledgment

First and foremost, I would like to express my sincere gratitude to my supervisor, Prof. Saurabh Basu, for his invaluable guidance, support, and expertise throughout the entire research journey. His unwavering commitment to academic excellence and his insightful feedback have been instrumental in shaping the direction and content of my research. I am truly grateful for the time and effort he has dedicated to mentoring me, and I am fortunate to have had the opportunity to work under his supervision.

I would also like to extend my appreciation to the chairman of my doctoral committee Prof. Subharadip Ghosh, doctoral committee members Dr. Pankaj Kumar Mishra and Dr. Biplab Bose for reviewing my progress every year and for their frank comments and valuable suggestions. I am thankful to all other members of the Physics department for their friendly behaviour whenever it was needed.

My sincere gratitude goes to our collaborators Prof. Tarun Kanti Ghosh, Dr. Priyadarshini Kapri, and Dr. Sudin Ganguly. Their invaluable contributions, expertise and enthusiasm have helped me to enrich my research work and broadened my perspectives. In particular, I am grateful to Dr. Priyadarshini Kapri for the countless discussions, brainstorming sessions, and shared experiences, which have played a pivotal role in shaping my research work and broadening my understanding of the subject.

I would like to thank the seniors and juniors of my group members, with special recognition given to Priyadarshini di, Sunayana di, Priyanka di, Shilpi di, Mijanur, Dipendu, Srijata, Koustav, Shreya, and Bishal for their support and cooperation. I am particularly grateful to Shilpi di for her exceptional support, motivation and mentorship. She treated me like a brother and made the research journey not only fruitful but also enjoyable.

I feel fortunate for having Pushpesh (Pandit ji), Mrinal (MKG), Shubhangi, Pushpanjali (Patra), and Partha as friends who made our research years so mem-

orable. Especially, I am grateful to have Pushpesh as a friend. His empathetic nature and willingness to lend an ear or offer a helping hand have been a constant source of comfort and reassurance for me. I also want to extend special thanks to Mrinal for bringing fun and excitement into our lives, both in the battleground of PUBG and in real life at IITG.

My special thanks go to Shyam da, Shamik da, Sourav da, Subhadeep da, and Rony da for their incredible contributions in making my hostel life truly enjoyable. Whether it was during breakfast, lunch, or dinner, all of you played an integral role in creating memorable moments. I am particularly thankful to Shyam da for his unconditional support whenever I needed it.

My childhood friend Sumit deserves special thanks. From primary school onwards, he has been a constant source of support and guidance, always ready to lend a helping hand and offer valuable advice.

Most importantly, I owe a tremendous debt of gratitude to my entire family, with special recognition to my parents and sister. Without their encouragement and unconditional love, my career would not have been possible. I am also incredibly happy to have my pet cats, especially Ghutu & Gulu, for filling my life with joy and happiness. To my dear sister, I wish to express my heartfelt appreciation for always being by my side. Lastly, I am profoundly indebted to my beloved grandma and uncle for their unwavering love and support. No words can adequately convey the impact they have had on my life.

July, 2023

Sayan Mondal

Abstract

We study the evolution of the topological properties of Chern insulators subjected to band engineering for a variety of systems, such as, the honeycomb lattice, dice lattice, bilayer honeycomb lattice etc. Since topology is inextricably related to band properties, engineering band deformities results in the evolution of the topological invariants and may even induce phase transitions. In particular, a honeycomb lattice under deformation demonstrates vanishing of the Dirac electrons, and eventually yields a scenario where the electronic dispersion is linear in one direction and quadratic along the other one. This is known as the semi-Dirac dispersion. A variety of materials and cold atomic systems, demonstrate such a dispersion. Further, the inclusion of the Haldane flux breaks the time-reversal symmetry (TRS) and creates an energy gap in the spectrum which makes the system a topological (Chern) insulator. The topological gap vanishes in the semi-Dirac limit, which, however reopens upon further deformation. The nature of the gaps prior to, and beyond the semi-Dirac limit have distinct features (TRS remains broken all the while), and have been elaborately studied in the thesis. Going a step ahead of the traditional Haldane model, we have considered a third neighbour hopping, in presence of which the system exhibits higher Chern number (C), such as, $C = \pm 2$, along with $C = \pm 1$. Further, a bilayer Haldane system with Bernal stacking exhibits differential behaviour of the bands that are closer to the Fermi level than the ones further away from it. Multiple topological phase transitions are realized for such a bilayer model. Moreover, a dice lattice, which not only is an interesting extension of the honeycomb structure of graphene, it also hosts a flat band that is in general relevant for studying strong electronic correlations. As in the earlier case, the system possesses topological regions with higher Chern numbers, however, it shows topological phase transitions straight from $C = \pm 2$ phases to a $C = 0$ phase (trivial insulator). In all of these cases, we have depicted the phase diagrams to support the topological phase transition occurring therein via the presence or the absence of edge currents in semi-infinite

ribbon geometries, and evolution of the plateau in the anomalous Hall conductivity in presence of band engineering. The corresponding scenario in a quantum spin Hall insulator described by a Kane-Mele model has been explored and the spin resolved bands respond in no different manner to the band deformation as shown via computing the $\mathbb{Z}_2$ invariant. The evolution of the spin Hall response shows vanishing of the quantum spin hall phase in the semi-Dirac limit.

List of Publications

Journal Publications

1. *Topological phase transition induced by band structure modulation in a Chern insulator*
   Sayan Mondal, Priyadarshini Kapri, Bashab Dey, Tarun Kanti Ghosh and Saurabh Basu, J. Phys.: Condens. Matter **33**, 225504, (2021).

2. *Evolution of the Berry phase and topological properties of a band deformed Chern insulator*
   Sayan Mondal and Saurabh Basu, Eur. Phys. J. B **94**, 207 (2021).

3. *Evolution of the Berry phase and topological properties in models for merging Dirac cones*
   Sayan Mondal and Saurabh Basu, Physica E **138**, 115048 (2022).

4. *Vanishing of the quantum spin Hall phase in a semi-Dirac Kane-Mele model*
   Sayan Mondal and Saurabh Basu, Phys. Rev. B **105**, 235409 (2022).

5. *Topological phases of a semi-Dirac Chern insulator in the presence of extended range hopping*
   Sayan Mondal and Saurabh Basu, Phys. Rev. B **105**, 235441 (2022).

6. *Topological features of the Haldane model on a dice lattice: Flat-band effect on transport properties*
   Sayan Mondal and Saurabh Basu, Phys. Rev. B **107**, 035421 (2023).

7. *Band engineered bilayer Haldane model: Evidence of multiple topological phase transitions*,
   Sayan Mondal and Saurabh Basu, Phys. Rev. B **108**, 045307 (2023).

Book Chapter

1. **Sayan Mondal**, Sudin Ganguly, and Saurabh Basu, *Basic Sciences for Sustainable Development*,
   Chapter-*Topology and applications of 2D Dirac and semi-Dirac materials*,
   De Gruyter, (2023). https://doi.org/10.1515/9783111071206

Conference/Workshop Presentations

1. Oral presentation at **2nd IIT Guwahati and TokyoTech Joint Workshop on Condensed Matter and High Energy Physics** - held online on 15th to 18th December, 2020.

2. Oral presentation at **3rd National Conference on Frontiers of Modern Physics (NCFMP 2021)** - held on 26th and 27th November, 2021 in School of basic and Applied Sciences, Adamas University.

3. Oral presentation at **Annual Conference on Quantum Condensed Matter (QMAT 2022)** - held on 18th to 22th September, 2022 in IIT Kanpur.

4. Poster presentation at **Emergent Phenomena in Quantum Materials (E-QMAT 2022)** - held on 12th to 14th October, 2022 in IIT Roorkee.

5. Oral presentation at **APS March Meeting (2023)**- held on 5th to 10th March, 2023 at Caesars forum in Las Vegas, USA.

Contents

List of Figures

List of Tables

Chapter 1

Introduction

The discovery of quantum Hall effect (QHE) in the year 1980 [1] in '*dirty*' two dimension electron gases stimulated an immense amount of research on the topological phases of matter in the scientific community. The QHE displays a series of quantized plateaus in the Hall conductivity in unit of e^2/h, and soon afterwards it is shown than the quantization is described by the Thouless-Kohmoto-Nightingale-den Nijs (TKNN) invariant [2]. This quantization occurs due to the presence of the discrete magnetic Bloch bands [2–7] or the Landau levels [8–11] owing to the presence of an external magnetic flux. Besides the magnetic field-induced Hall effect, there have been attempts to observe such behavior in the absence of magnetic fields, known as the quantum anomalous Hall effect (QAHE), which relies solely on the system's time-reversal symmetry (TRS) breaking [12–15]. The idea of QAHE was first introduced by Haldane [16] in a two-dimensional honeycomb lattice (a paradigmatic model for graphene), where a complex next-nearest-neighbor (NNN) hopping with a phase ϕ (also known as Haldane flux) was included to break the TRS. In this model, the bands are associated with a topological invariant, namely, the Chern number, C. C denotes the TKNN invariant in this case and hence describes the quantization of the Hall conductivity. A Semenoff mass term (usually denoted by Δ) that breaks the sublattice symmetry may also be included (a prototype model for hexagonal Boron Nitride (h-BN)), that causes opening or closing of the spectral gap in the electronic band structure. The phase diagram shows the variation of the Chern number as a function of

Δ and ϕ, and encodes the opening and closing of the band gaps at the Dirac points, where the spectrum shows linear dispersion in the absence of Haldane flux, usually denoted by $\mathbf{K}$ and $\mathbf{K}'$ points in the Brillouin zone (BZ). The value of the Chern number determines the nature of the spectral gap, that is, whether it is a topological (finite) or trivial (zero) gap.

Let us give a general introduction to topology which will aid our subsequent discussions. Topological properties of materials are interwoven with their electronic band structure [17–20]. The topology of a band is characterized by several quantities, including the Berry phase, Berry connection, Berry curvature and the topological invariant, namely, the Chern number as mentioned earlier. In 1984, M.V. Berry first introduced the concept of the Berry phase [21], a quantity that describes how a global phase of a complex vector evolves when carried out along a closed orbit in a planar surface. The complex vector is equivalent to the Berry connection. The Berry connection also facilitates the calculation of Berry curvature, whose non-zero values give an indication of non-trivial topology of the system. There is a close analogy with the electrodynamics, where the Berry connection is equivalent to the vector potential, the Berry phase is equivalent to the magnetic flux and the Berry curvature is equivalent to the magnetic field. In terms of this analogy, we can talk about a particular case, where for a 2D honeycomb lattice, the non-zero Berry phase implies the flux of the magnetic field at the point of degeneracies, namely, the Dirac points. Stated slightly differently, the electrons pick up a phase as it circulates around a closed orbit in the k-space.

Further, the integration of Berry curvature in the first BZ yields Chern number. As stated earlier, the Chern number is the topological invariant that may be non-zero if a system has broken TRS. The corresponding non-zero value gives the quantization of the plateau found in the anomalous Hall conductivity and the number of chiral edge modes in a semi-infinite geometry, such as a ribbon. Further, if we involve the real spin degrees of freedom for the electron, and the TRS remains protected, then we observe vanishing of the Hall conductivity, however, the spin Hall conductivity has a non-zero value. This type of system is characterized by a topological invariant, known as the $\mathbb{Z}_2$ invariant where the system exhibits helical edge modes in a nanoribbon.

After Haldane's groundbreaking work in 1988, people have looked for similar topological phases in various two-dimensional model systems, such as the Lieb lattice [22–25], checkerboard lattice [26], and Kagomé lattice [27–30], buckled lattice [31], acoustic system [32] etc. Notably, experimental realizations of the Haldane model have also been achieved in two-dimensional honeycomb structures, including Fe-based ferromagnetic insulators $X\mathrm{Fe}_2(\mathrm{PO}_4)_2$, where X can be K, Cs, or La [33], the interface between the two trivial ferromagnetic insulators EuO and GdN [34] etc. Additionally, cold atomic systems loaded in the optical lattice (the latter is created by standing-wave laser beams [35–37]), such as an optical honeycomb lattice [38], dice lattice [39] etc, has opened up new possibilities for investigating similar non-trivial topological phases.

One notable feature for a two-dimensional honeycomb lattice is that in the absence of the Haldane flux, the dispersion is linear along both longitudinal directions in the momentum-space (k-space) about the band touching Dirac points ($\mathbf{K}$ and $\mathbf{K}'$) in the BZ. These are known as the massless Dirac systems and the corresponding Hamiltonian represents the electronic properties of graphene at low energies. A related scenario, where the dispersion is linear in one direction and quadratic along the perpendicular one, and is known as the semi-Dirac dispersion [40, 41], also exists in the literature. Here, the electrons behave as a massless fermions along one direction in the BZ and massive particles along the perpendicular direction. Thus it is distinct from the Dirac case where the fermionic behaviour is isotropic. Such anisotropic behaviour has been observed in multilayered structures, such as, $(\mathrm{TiO}_2)_5/(\mathrm{VO}_2)_n$ (n denotes the number of VO_2 layers) with $n = 3$ and $n = 4$ [42, 43], phosphorene under an electric field [44, 45] and pressure [46], graphene under doping and pressure [47, 48], a deformed graphene structure [49], organic salts, such as $\mathrm{BEDT\text{-}TTF}_2\mathrm{I}_3$ under pressure [50, 51], oxidized silicene layers [52], black phosphorene doped by potassium atoms by means of *in situ* [53] etc. In addition, the semi-Dirac dispersion has been investigated for its optical properties [54, 55], thermoelectric properties [55, 59], Floquet states [56–58], magnetic susceptibility, specific heat, Faraday rotation [60], Landau levels, and the transport properties [61–63].

There is a smooth way to connect a Dirac spectrum to a semi-Dirac one which

TH-3205_186121022

is done via band engineering (or a band deformation), and forms the main thrust of this thesis. Since the topological properties are related to the characteristic of the energy bands, band engineering will surely affect the topological properties. However, it is not clear apriori, how it affects, or whether it can induce a phase transition from one topological phase to another. The different chapters presented in this thesis perform a comprehensive study of this topic and explore several interesting features of topological phase transitions that occur in the system.

Let us discuss the details of the band engineering that we have spoken about. All our calculations are limited to 2D honeycomb lattice and its variants, where the transition from a Dirac to a semi-Dirac dispersion can be smoothly achieved via the introduction of an anisotropy among the nearest-neighbour (NN) hopping amplitudes. In such an inhomogeneous hopping scenario, the two Dirac cones situated at the $\mathbf{K}$ and the $\mathbf{K}'$ points shift towards each other. At a certain value of the anisotropy, the Dirac cones merge into one at the $\mathbf{M}$ point in the BZ, where we observe the so-called semi-Dirac dispersion. Several theoretical studies have explored the anisotropy-induced movement and merger of Dirac cones in the crystal lattice [49, 68], and the impact of a continuous deformation of the band structure on physical properties, such as, specific heat, Landau quantization [49], the density of states (DOS) [51], optical conductivity [68], the Hofstadter butterfly [69] etc. Also, the band-deformation has been experimentally realized in several other systems, such as, germanene and stanene [64], different optimized structures [65, 66], such as, α-graphyne, β-graphyne [67] etc. However, the topological properties in the context of band engineering have not been studied and thus left space for us to do a systematic and exhaustive exploration of the topic. It is worth noting that topological phases are achieved by breaking the TRS of the system, either by including a perpendicular magnetic field or via adding the complex second neighbour hopping, namely, the Haldane term. We are interested in the latter. A gap opens up in the spectrum of Dirac case at the $\mathbf{K}$ and $\mathbf{K}'$ points, however, what happens in the semi-Dirac case remains to be explored.

Further, the Haldane model demonstrate the non-trivial phases with the Chern numbers $C = +1$ and -1. A related and topical issue is that if there is a way to increase the value of the topological invariant C, which encodes a larger val-

ues of the Hall conductivity and hence should be realizable at high temperatures. Intuitively, a multi-band system should be able to yield larger Chern numbers. However, we have observed that there is an alternative way to achieve higher Chern number by including a longer range hopping in our system [70]. Such further neighbour hopping increases the number of Dirac cones in the dispersion spectrum. The system becomes a topological insulator in presence of the Haldane flux and shows higher Chern numbers (for example, $C = \pm 2, \pm 3$ etc). Interestingly, such extended hopping can also be added in the semi-Dirac system, which may show higher Chern numbers, and the may yield topological phase transition where the Chern number discontinuously changes from one allowed value to another (including $C = 0$). Such higher values of the Chern numbers are realized beyond the 2D honeycomb lattice, and are found in a star lattice (decorated honeycomb structure) [71], multi-orbital triangular lattice with third neighbor hopping [72], the spin-orbit coupled honeycomb lattice [73, 74], ultracold atomic gases on a triangular lattice [75, 76], magnetic-doped topological insulators [77], Cr-doped thin laminar sheets of $\mathrm{Bi}_2(\mathrm{Se}, \mathrm{Te})_3$ [78], in a classical system created by means of acoustic components [79] etc. Experimentally, higher Chern numbers have been realized in multilayered structures of magnetically doped, and undoped topological insulators [80], $\mathrm{MnBi}_2\mathrm{Te}_4$ at high temperature [81, 82] etc.

One may also achieve higher Chern numbers in multi-band systems which may be found in coupled bilayer systems [83–86], Moiré lattices [87–91] etc. A bilayer graphene (in presence of Haldane flux) is one of such candidate. In the absence of the Haldane flux, an interlayer coupling among the two layers plays a crucial role in determining the electronic properties at the low energies. The dispersion spectrum progressively becomes quadratic in nature at the low energies as the interlayer coupling is enhanced. Interestingly, one may also look for the behaviour of the electrons in the semi-Dirac limit for a bilayer graphene. Inclusion of a Haldane flux will create a non-trivial gap and the corresponding scenario needs to be ascertained for the semi-Dirac case.

Further, a dice lattice is a suitable candidate which exhibits higher Chern numbers [92]. The spectrum shows three bands, including a flat band owing to the presence of an additional sublattice at the center of hexagon [93–105].

TH-3205_186121022

Except for the flat band, the rest of the two bands are identical to that of a honeycomb lattice. It is known that in presence of Haldane flux, the valence and the conduction bands acquire larger Chern numbers, namely, $C = \pm 2$. However, the flat band shows zero Chern number. One notable feature of the flat band is that it exhibits dissipationless properties, and may provide a perfect platform for investigating strong electronic correlations, the kinetic energy of the particles being entirely quenched. In a way, they are analogous to the Landau levels with regards to their non-dispersive nature. There have been theoretical predictions regarding several intriguing phenomena, including Wigner crystallization in honeycomb structures [106], a large critical temperature for superconductivity [107], and fractional Chern insulators [108, 109]. On the experimental front, flat bands have been observed in photonic crystals [110], optical lattices [111], and metamaterials [112]. However, the band structure for semi-Dirac dice lattice has not been explored. In particular, the effect on the non-trivial phases due to the Haldane flux in a band deformed dice lattice, that is, the semi-Dirac limit has not been studied and constitutes a topic for us to investigate.

In the above discussed models, the electron spin is not included into consideration. This is because most experimental situations correspond to spin-polarized behaviour, making the role of electron spin inconsequential. Here, we include the electron spin in the Haldane model which is known as the Kane-Mele model [113, 114]. One important consequence of the inclusion of a spin is restoration of the lost TRS. With TRS being intact, the QHE will vanish. However, this yields another topological state of matter, namely, the quantum spin Hall (QSH) state. A spin-orbit coupling of a special type, namely, the Rashba spin-orbit coupling (RSOC) [115], which is usually present (and may be strong) in systems with broken inversion symmetry (described below) can now be incorporated. This restores TRS and has interesting consequences for technological applications of the spintronic devices.

The RSOC appears in a system where the surface inversion symmetry is not preserved which leads to a non-zero potential gradient [116, 117]. Such potential gradient can be controlled by using an external gate voltage, allowing for control of RSOC [118, 119]. The strength of RSOC can be enhanced by significant amount

[120] and it is used in different type of devices, such as, spin interference based devices [121, 122], spin field effect transistor [123] etc. However, the RSOC in graphene is very weak ($\sim$ few meV). Nonetheless, it can be enhanced by using the proximity effect of heavy adatoms, such as, Au, Ni, Pb, Ir or Co etc to values as large as 100meV [124–133].

Further, the QSH phase in the Kane-Mele model is defined by a non-zero topological invariant, known as the $\mathbb{Z}_2$ invariant (instead of the Chern number which is a $\mathbb{Z}$ invariant). This category of insulators are called as $\mathbb{Z}_2$ topological insulators and they posses a finite spin Hall conductivity [114]. The RSOC and a sublattice symmetry breaking staggered potential, namely, the Semenoff mass gives rise to a phase diagram displaying topological phase transitions where the $\mathbb{Z}_2$ invariant shows a discontinuous jump from a value 1 to 0. However, these phases of the semi-Dirac system have not been explored.

In experiments, the non-zero spin Hall conductivity has been observed in a variety of materials, including CdTe-HgTe [134, 135], Cl-doped ZnSe [136], FePt/Au devices [137], Pt [138], GaAs [139], Pt/Au lateral spin valve structures [140] etc. These observations provide opportunities to manipulate the spin degree of freedom for achieving dissipationless transport, which is a crucial aspect of spintronics.

Motivated by the above scenario, we wish to explore topological phases in band-engineered systems. We shall study both Chern insulating phase and quantum spin Hall phase in various systems in presence of band deformation. Later, we will see how the band structure is intimately related to topological phases of matter, which in turn affects the conducting properties and the edge modes of the system.

1.1 Topological invariants

Topology is a mathematical subject that examines quantities that remain unchanged during continuous transformations. These quantities are referred to as topological invariants. For example, one can transform a single hole donut into a coffee cup, but the number of holes (which is one in this case) remains the same, which is a topological invariant. Such invariants play a crucial role in distinguishing topological and trivial phases.

In condensed matter systems, the role of topology first came into light after the discovery of integer quantum Hall effect [1]. As already stated, the plateaus are associated with topological invariants known as the Chern numbers [141, 142]. In this section, we will see computation of such topological invariants from the band properties. However, we begin form Berry phase for a better understanding of the topological invariants.

1.1.1 Berry phase

In quantum mechanics, the state of a system is described by a set of vectors in the Hilbert phase. Multiplication by a complex phase does not change any information, as the phase cancels out in expectation values and only the expectation values are physically relevant. In that sense, a phase in the wave vector does not have any physical importance. However, the relative phase between two vectors can not be neglected which was shown by Berry in 1984 [21]. Since, if a system evolves in a cyclic manner, a phase can accumulate in the observable quantity. This phase is known as the Berry phase (also known as the Berry-Pancharatnam phase).

We consider a set of vectors, $|\Psi_1\rangle, |\Psi_2\rangle, ...|\Psi_N\rangle$ in the Hilbert space. Say, the vectors are arranged in a loop. The phase difference between two vectors is given by,

$$\begin{aligned} \gamma_{12} &= -\arg\langle\Psi_1|\Psi_2\rangle \\ \implies e^{-i\gamma_{12}} &= \frac{\langle\Psi_1|\Psi_2\rangle}{|\langle\Psi_1|\Psi_2\rangle|} \\ \implies \gamma_{12} &= i\ \ln\left[\frac{\langle\Psi_1|\Psi_2\rangle}{|\langle\Psi_1|\Psi_2\rangle|}\right] \end{aligned} \tag{1.1}$$

Now, the Berry phase is defined by the net relative phase in one complete cycle, which is,

$$\begin{aligned} \gamma &= \gamma_{12} + \gamma_{23} + ... + \gamma_{N1} \\ \implies \gamma &= i\ \ln\left[\frac{\langle\Psi_1|\Psi_2\rangle}{|\langle\Psi_1|\Psi_2\rangle|}\frac{\langle\Psi_2|\Psi_3\rangle}{|\langle\Psi_2|\Psi_3\rangle|}...\frac{\langle\Psi_N|\Psi_1\rangle}{|\langle\Psi_N|\Psi_1\rangle|}\right] \end{aligned} \tag{1.2}$$

In the continuum case, the vectors are dependent on certain parameter, say $\boldsymbol{\zeta}$. Further, we assume a curve $\mathcal{L}$ that depends on the parameter $\boldsymbol{\zeta}$, and the components of $|\Psi(\boldsymbol{\zeta})\rangle$ are smooth along $\mathcal{L}$. Then the relative phase between two vectors at $\boldsymbol{\zeta}$ and $\boldsymbol{\zeta} + \mathrm{d}\boldsymbol{\zeta}$ lying in curve $\boldsymbol{\zeta}$ is given by,

$$\Delta\gamma = i \ \ln\left[\frac{\langle\Psi(\boldsymbol{\zeta})|\Psi(\boldsymbol{\zeta}+\mathrm{d}\boldsymbol{\zeta})\rangle}{|\langle\Psi(\boldsymbol{\zeta})|\Psi(\boldsymbol{\zeta}+\mathrm{d}\boldsymbol{\zeta})\rangle|}\right] \tag{1.3}$$

We do a Taylor series expansion of $\ln\left[\langle\Psi(\boldsymbol{\zeta})|\Psi(\boldsymbol{\zeta}+\mathrm{d}\boldsymbol{\zeta})\rangle\right]$ upto first order in $\mathrm{d}\boldsymbol{\zeta}$ which yields,

$$\begin{aligned}
&\ln\left[\langle\Psi(\boldsymbol{\zeta})|\Psi(\boldsymbol{\zeta}+\mathrm{d}\boldsymbol{\zeta})\rangle\right] = \ln\left[\langle\Psi(\boldsymbol{\zeta})|\Psi(\boldsymbol{\zeta})\rangle + \langle\Psi(\boldsymbol{\zeta})|\boldsymbol{\nabla}_{\boldsymbol{\zeta}}|\Psi(\boldsymbol{\zeta})\rangle\cdot\mathrm{d}\boldsymbol{\zeta}\right] \\
\implies &\ln\left[\langle\Psi(\boldsymbol{\zeta})|\Psi(\boldsymbol{\zeta}+\mathrm{d}\boldsymbol{\zeta})\rangle\right] = \ln\left[1 + \langle\Psi(\boldsymbol{\zeta})|\boldsymbol{\nabla}_{\boldsymbol{\zeta}}|\Psi(\boldsymbol{\zeta})\rangle\cdot\mathrm{d}\boldsymbol{\zeta}\right] \\
\implies &\ln\left[\langle\Psi(\boldsymbol{\zeta})|\Psi(\boldsymbol{\zeta}+\mathrm{d}\boldsymbol{\zeta})\rangle\right] \simeq \langle\Psi(\boldsymbol{\zeta})|\boldsymbol{\nabla}_{\boldsymbol{\zeta}}|\Psi(\boldsymbol{\zeta})\rangle\cdot\mathrm{d}\boldsymbol{\zeta}
\end{aligned} \tag{1.4}$$

we also get a similar expression for the denominator of Eq. 1.3. However, since it is the modulus of a complex number and under infinitesimal change ($\mathrm{d}\boldsymbol{\zeta} \to 0$), it is close to zero. Therefore, $\Delta\gamma$ can be written as,

$$\Delta\gamma = i\ \langle\Psi(\boldsymbol{\zeta})|\boldsymbol{\nabla}_{\boldsymbol{\zeta}}|\Psi(\boldsymbol{\zeta})\rangle\cdot\mathrm{d}\boldsymbol{\zeta} \tag{1.5}$$

since the Berry phase is sum of all such phase around a closed path, Φ_B can be expressed as,

$$\Phi_B = i \oint_{\mathcal{L}} \langle\Psi(\boldsymbol{\zeta})|\boldsymbol{\nabla}_{\boldsymbol{\zeta}}|\Psi(\boldsymbol{\zeta})\rangle\cdot\mathrm{d}\boldsymbol{\zeta} \tag{1.6}$$

We shall use this expression to compute Berry phase. The quantity in the integrand is known as the Berry connection which is denoted by $\mathcal{A}$, that is,

$$\mathcal{A} = i\langle\Psi(\boldsymbol{\zeta})|\boldsymbol{\nabla}_{\boldsymbol{\zeta}}|\Psi(\boldsymbol{\zeta})\rangle \tag{1.7}$$

One can also compute the curl of $\mathcal{A}$, which can be denoted by $\boldsymbol{\Omega}$. and is known as the Berry curvature.

$$\boldsymbol{\Omega} = \boldsymbol{\nabla}\times\mathcal{A} \tag{1.8}$$

In a condensed matter system, the Bloch wave vector of a Hamiltonian is used

to compute Berry connection, which further helps to compute Berry phase and Berry curvature [143]. The momentum, $\mathbf{k}$ is used as the parameter $\boldsymbol{\zeta}$ and the curve $\mathcal{L}$ lie in the BZ. The calculations of Berry curvature are illustrated in the next section.

1.1.2 Berry curvature

We show the Berry curvature for a two-dimensional system whose band structure lies in the k_x-k_y plane. Therefore, the Berry curvature is a function of k_x and k_y which is given by,

$$\begin{aligned}\Omega &= [\nabla \times \mathcal{A}]_z \\ &= \frac{\partial \mathcal{A}_y}{\partial k_x} - \frac{\partial \mathcal{A}_x}{\partial k_y}\end{aligned} \tag{1.9}$$

Here only the z-component of Ω is non-zero since $\mathcal{A}$ is independent of any k_z variable. Now, the above expression may be simplified in the following way.

$$\begin{aligned}\Omega_z &= \frac{\partial \mathcal{A}_y}{\partial k_x} - \frac{\partial \mathcal{A}_x}{\partial k_y} \\ &= i\,\frac{\partial}{\partial k_x}\langle \Psi(\mathbf{k})|\frac{\partial}{\partial k_y}\Psi(\mathbf{k})\rangle - [x \longleftrightarrow y] \\ &= i\,\left\langle \frac{\partial}{\partial k_x}\Psi(\mathbf{k})\middle|\,\frac{\partial}{\partial k_y}\Psi(\mathbf{k})\right\rangle + i\,\left\langle \Psi(\mathbf{k})\middle|\,\frac{\partial^2}{\partial k_x \partial k_y}\Psi(\mathbf{k})\right\rangle - [x \longleftrightarrow y] \\ &= i\,\left\langle \frac{\partial}{\partial k_x}\Psi(\mathbf{k})\middle|\,\frac{\partial}{\partial k_y}\Psi(\mathbf{k})\right\rangle - i\,\left\langle \frac{\partial}{\partial k_y}\Psi(\mathbf{k})\middle|\,\frac{\partial}{\partial k_x}\Psi(\mathbf{k})\right\rangle \\ &= -2\ \mathrm{Im}\left\langle \frac{\partial}{\partial k_x}\Psi(\mathbf{k})\middle|\,\frac{\partial}{\partial k_y}\Psi(\mathbf{k})\right\rangle\end{aligned} \tag{1.10}$$

where we have used the relation $\frac{\partial^2}{\partial k_x \partial k_y} = \frac{\partial^2}{\partial k_y \partial k_x}$. If we have a Hamiltonian that is written in the form $H = \mathbf{h}(\mathbf{k}) \cdot \boldsymbol{\sigma}$, where $\boldsymbol{\sigma}$ is the 2×2 Pauli matrix vector, then Ω can be written in a simplified form. In order to derive it, we rewrite the fourth line

of Eq. 1.10 in the following way,

$$\begin{aligned}\frac{1}{i}\Omega &= \langle\partial_x\Psi_+|\partial_y\Psi_+\rangle - \langle\partial_x\Psi_+|\partial_y\Psi_+\rangle \\ &= \sum_{n=\pm}\langle\partial_x\Psi_+|\Psi_n\rangle - [x\leftrightarrow y] = \langle\partial_x\Psi_+|\Psi_-\rangle\langle\Psi_-|\partial_y\Psi_+\rangle - [x\leftrightarrow y]\end{aligned} \tag{1.11}$$

where $\Psi_\pm$ are the two eigen vectors corresponding to the 2×2 Hamiltonian. For brevity, $\frac{\partial}{\partial k_x}$ and $\frac{\partial}{\partial k_y}$ are written as ∂_x and ∂_y respectively. The left part of the second line is obtained by inserting the complete set of states, $I=\sum_{n=\pm}|\Psi_n\rangle\langle\Psi_n|$, while the right part is obtained using the relation $\langle\partial_x\Psi_+|\Psi_+\rangle\langle\Psi_+|\partial_y\Psi_+\rangle - [x\leftrightarrow y]=0$. Next we apply the first order perturbation theory to write the eigen vectors of $H(\mathbf{k}')=H(\mathbf{k}+\delta\mathbf{k})=H(\mathbf{k})+\delta x^\lambda\delta_\lambda H$ in terms of those of $H(\mathbf{k})$ which is given by,

$$|\Psi_+(\mathbf{k}')\rangle = |\Psi_+\rangle + \frac{\langle\Psi_-|\delta x^\lambda\,\partial_\lambda H|\Psi_+\rangle}{E_+-E_-}|\Psi_-\rangle = |\Psi_+\rangle + \frac{\langle\Psi_-|\delta x^\lambda\,\partial_\lambda\hat{\mathbf{h}}\cdot\boldsymbol{\sigma}|\Psi_+\rangle}{E_+-E_-}|\Psi_-\rangle \tag{1.12}$$

This equation implies,

$$\langle\Psi_-|\partial_y\Psi_+\rangle = \frac{1}{2}\langle\Psi_-|\partial_y\,\hat{\mathbf{h}}\cdot\boldsymbol{\sigma}|\Psi_+\rangle \tag{1.13}$$

We use this in Eq. 1.11 which is simplified further in the following way,

$$\begin{aligned}\frac{1}{i}\Omega &= \langle\partial_x\Psi_+|\Psi_-\rangle\langle\Psi_-|\partial_y\Psi_+\rangle - [x\leftrightarrow y] \\ &= \frac{1}{4}\Big[\langle\Psi_+|\partial_x\,\hat{\mathbf{h}}\cdot\boldsymbol{\sigma}|\Psi_-\rangle\langle\Psi_-|\partial_y\,\hat{\mathbf{h}}\cdot\boldsymbol{\sigma}|\Psi_+\rangle - [x\leftrightarrow y]\Big] \\ &= \frac{1}{4}\sum_{n=\pm}\Big[\langle\Psi_+|\partial_x\,\hat{\mathbf{h}}\cdot\boldsymbol{\sigma}|\Psi_n\rangle\langle\Psi_-|\partial_y\,\hat{\mathbf{h}}\cdot\boldsymbol{\sigma}|\Psi_n\rangle - [x\leftrightarrow y]\Big] \\ &= \frac{1}{4}\Big(\langle\Psi_+|[\partial_x\,\hat{\mathbf{h}}\cdot\boldsymbol{\sigma},\partial_y\,\hat{\mathbf{h}}\cdot\boldsymbol{\sigma}]|\Psi_+\rangle\Big) = \frac{i}{2}\epsilon_{ijk}(\partial_x\,\hat{\mathbf{h}}_i)(\partial_y\,\hat{\mathbf{h}}_j)\langle\Psi_+|\sigma_k|\Psi_-\rangle \\ &= \frac{i}{2}\epsilon_{ijk}(\partial_x\,\hat{\mathbf{h}}_i)(\partial_y\,\hat{\mathbf{h}}_j)\hat{\mathbf{h}}_c = \frac{i}{2}\hat{\mathbf{h}}\cdot(\partial_x\,\hat{\mathbf{h}}\times\partial_y\,\hat{\mathbf{h}})\end{aligned} \tag{1.14}$$

To derive the third line from the second line of the above equation, the fact $\langle\Psi_+|\partial_x\,\hat{\mathbf{h}}\cdot\boldsymbol{\sigma}|\Psi_+\rangle\langle\Psi_+|\partial_y\,\hat{\mathbf{h}}\cdot\boldsymbol{\sigma}|\Psi_+\rangle - [x\leftrightarrow y]=0$ have been used. Finally, the

simplified form of Berry curvature can be written as,

$$\Omega_z(\mathbf{k}) = \frac{\mathbf{h}}{2|\mathbf{h}|^3} \cdot \left(\frac{\partial \mathbf{h}}{\partial k_x} \times \frac{\partial \mathbf{h}}{\partial k_y} \right). \tag{1.15}$$

The derivation of the above formula can be found in Ref. [144] and is included here for completeness. It should be noted that we have not introduced any band index to Ω in Eqs. 1.10 and 1.15. The band index arises because of several eigenvalues of a Hamiltonian. For example if we have a $n \times n$ Hamiltonian then we get n number of eigenvalues and n different Ω for each of the eigenvalue. So, we write another form of the Berry curvature which shows a direct involvement of different eigenvalues and can be expressed as,

$$\mathbf{\Omega}^n = -\mathrm{Im} \sum_{n' \neq n} \frac{\langle \Psi_n | \boldsymbol{\nabla} H | \Psi_{n'} \rangle \times \langle \Psi_{n'} | \boldsymbol{\nabla} H | \Psi_n \rangle}{(E_n - E_{n'})^2} \tag{1.16}$$

where the summation is taken over all eigen solutions excluding the one with the degeneracy. In the above expression, we have dropped the momentum variable k for brevity. It should be noted that once again we are left with only the z-component $\mathbf{\Omega}^n$ for a two-dimensional system.

1.1.3 Chern number

Chern number is defined as a sum of the Berry curvature for a system living on a torus. For a two dimensional system, the Brillouin zone (BZ) has a torus geometry, as the momenta have periodicity (say, 2π) and hence k_x and $k_x + 2\pi$, and k_y and $k_y + 2\pi$ are equivalent. Therefore the integration of Berry curvature over the first BZ yields Chern number.

$$C = \frac{1}{2\pi} \iint_{\mathrm{BZ}} \Omega_z(\mathbf{k}) \mathrm{d}^2\mathbf{k} \tag{1.17}$$

where Ω_z can be obtained from Eq. 1.10 or 1.15. The Chern invariant is not defined in case of any degeneracy in a system which is evident from Eq. 1.16 as the denominator vanishes, thereby leading to a divergence of Berry curvature.

In a condensed matter system, the Chern number is associated with a partic-

ular band and if it is non-zero, then the system is called as a Chern insulator or the topological insulator. The Chern insulator demonstrates topological properties, such as, quantized Hall conductivity, non-zero edge current etc. However, to achieve such non-trivial phases, we need to break the TRS and also there must be gap in the dispersion spectrum to avoid any degeneracy. We shall elaborate this later in the context of the Haldane model. Here we present another method which is used for the numerical computation of Chern number as illustrated in Ref. [145].

In our two-dimensional system, we assume the BZ spans from zero to k^x_{max} along the x direction, and from zero to k^y_{max} along the y direction. This zone is discretized into N points in both directions. Each point within the Brillouin zone is represented by the following coordinates,

$$k_j = (k^x_j, k^y_j) = \left(j\frac{k^x_{\text{max}}}{N}, j\frac{k^y_{\text{max}}}{N} \right) \tag{1.18}$$

To proceed, we make the assumption that the wave function Ψ exhibits periodicity on the lattice. In other words, we have $|\Psi(k_j + N_\mu \hat{\mu})\rangle = |\Psi(k_j)\rangle$, where $\hat{\mu}$ represents a vector in the μ direction. Now, the link variable is defined as,

$$U_\mu(k_j) = \frac{\langle \Psi(k_j)|\Psi(k_j + \Delta_\mu)\rangle}{|\langle \Psi(k_j)|\Psi(k_j + \Delta_\mu)\rangle|} \tag{1.19}$$

Here, Δ_μ denotes the width of the discretized momentum along the μ direction, given by $\Delta_\mu = k^\mu_{\text{max}}/N$. The link variables remain well-defined as long as the inner product in the denominator is non-zero.

Next, we evaluate the lattice field strength using the following formula:

$$F_{xy}(k_j) = \ln \frac{U_x(k_j)U_y(k_j + \Delta_x)}{U_x(k_j + \Delta_y)U_x(k_j)} \tag{1.20}$$

Finally, to determine the Chern number, we sum the field strengths over all the discretized points within the Brillouin zone, that is,

$$C = \frac{1}{2\pi i}\sum_j F_{xy}(k_j). \tag{1.21}$$

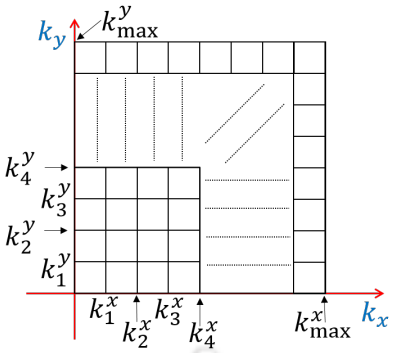

FIG. 1.1: A Brillouin zone is depicted which extends from zero to $k^x_{\max}$ in the x-direction and from zero to $k^y_{\max}$ in the y-direction. This zone is divided into N points in each direction.

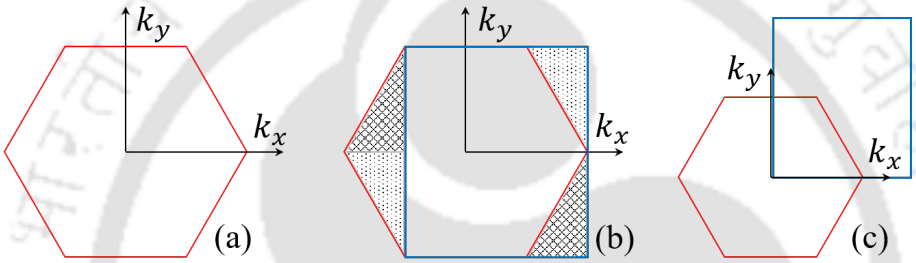

FIG. 1.2: The Brillouin zone of a honeycomb lattice is depicted in (a). In (b), the BZ is transformed into a rectangular shape and displayed in blue. To avoid any singularity at $(k_x, k_y) = (0, 0)$, the BZ can be further shifted as shown in (c).

It should be noted that we need a rectangular BZ in order to apply the above formula. If the BZ is not rectangular, one may transform into a rectangular shape by using reciprocal lattice vectors. For example, the BZ of honeycomb lattice has the hexagonal structure as shown in Fig. 1.2(a). Next the BZ is turned into a rectangular shape as shown in Fig. 1.2(b) by blue color. Two different shaded regions imply they are euivalent to each other. Further, to avoid any divergence at $(k_x, k_y) = (0, 0)$, the BZ is shifted to a new position as shown in Fig. 1.2(c).

We have used both Eqs. 1.17 and 1.21 to compute Chern numbers in all of the systems we considered.

1.1.4 $\mathbb{Z}_2$ topological invariant

In this section, we show the calculation of another topological invariant known as the $\mathbb{Z}_2$ invariant. It is an invariant which describes the quantum spin Hall

phase of a system. Such systems are different from the Chern insulators as they exhibit quantized spin Hall conductivity and spin filtered edge currents in a ribbon geometry, while the conductivity in the charge sector vanishes. In order to achieve a spin Hall insulating phase, the TRS should remain intact in the system. We have described such non-trivial phases elaborately later in the context of Kane-Mele model. In the following, we have presented the Fu-Kane method to calculate the $\mathbb{Z}_2$ invariant [147].

We consider a one-dimensional system with lattice constant $a = 1$ and length $L = N_c$ with periodic boundary conditions and $2N$ occupied bands. The normalized eigenstates of the nth band can be written as

$$|\Psi'_{k,n}\rangle = \frac{1}{\sqrt{N_c}} e^{ikx} |\Psi_{k,n}\rangle \tag{1.22}$$

To describe the topological properties of this system, the Wannier charge centers (WCCs) are employed. The polarization is determined by summing the center of charge of the Wannier states associated with the $R = 0$ unit cell across all bands. This can be written as,

$$P_\rho = \sum_n \langle 0, n|r|0, n\rangle = \sum_n \frac{i}{2\pi} \int_{-\pi}^{\pi} \langle \Psi_{k,n}|\nabla_k|\Psi_{k,n}\rangle = \sum_n C_n \tag{1.23}$$

where C_n represents the Chern number of the nth band. It should be noted that the charge polarization is defined only up to a lattice constant. However, by adiabatically changing $H(t)$ from an initial value t_1 to a final value t_2 and ensuring the continuity of $|\Psi_{k,n}(t)\rangle$, the change in charge polarization can be expressed as

$$P_\rho[t_1] - P_\rho[t_2] = \frac{1}{2\pi} \left[\oint_{c_2} \mathrm{d}k \mathcal{A}(t, k) - \oint_{c_1} \mathrm{d}k \mathcal{A}(t, k) \right] \tag{1.24}$$

where $c_{2(1)}$ denotes the loop for $k = -\pi$ to π at a fixed $t = t_{1(2)}$. The integrand is the Berry connection and is given by,

$$\mathcal{A}(t, k) = i \sum_n \langle \Psi_{k,n}(t)|\nabla_k|\Psi_{k,n}(t)\rangle. \tag{1.25}$$

Now, the change in charge polarization can be computed and has the following

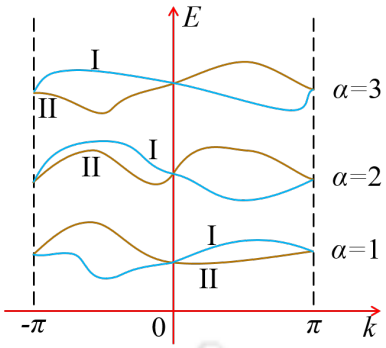

FIG. 1.3: The Kramers pairs of bands for a one-dimensional system are displayed.

form,

$$P_\rho[t_1] - P_\rho[t_2] = \frac{1}{2\pi}\int_{\tau_{1,2}} \mathrm{d}t\ \mathrm{d}k\ \Omega(t,k) \tag{1.26}$$

where $\Omega(t,k)$ is the Berry curvature which can be written as,

$$\Omega(t,k) = i\sum_n [\langle\nabla_t\Psi_{k,n}(t)|\nabla_k\Psi_{k,n}(t)\rangle - \langle\nabla_k\Psi_{k,n}(t)|\nabla_t\Psi_{k,n}(t)\rangle] \tag{1.27}$$

Considering a total period T, the quantity $P_\rho(T) - P_\rho(0)$ in the above equation corresponds to the integral over an entire torus in t and k space, representing an integer known as the first Chern number. It's worth noting that the system possesses time-reversal invariance, resulting in a total of zero Chern number.

Now, in order to calculate the $\mathbb{Z}_2$ invariant, Fu and Kane introduced a division of the total charge polarization $P\rho$ into two parts to account for the presence of Kramers Pairs. Let us assume we have $2N$ bands, where each pair is labelled by $\alpha = 1, ..., N$. The bands corresponding to each α are assigned with indices $s = \mathrm{I}, \mathrm{II}$ as depicted in Fig. 1.3. One advantage of Kramers Pairs is that the time-reversed Bloch waves at k are related to the Bloch waves at $-k$ up to a phase factor, that is,

$$|\Psi^{\mathrm{I}}_{-k,\alpha}\rangle = -e^{i\chi_{k,\alpha}}\Theta|\Psi^{\mathrm{II}}_{k,\alpha}\rangle \tag{1.28}$$

$$|\Psi^{\mathrm{II}}_{-k,\alpha}\rangle = e^{i\chi_{-k,\alpha}}\Theta|\Psi^{\mathrm{I}}_{k,\alpha}\rangle \tag{1.29}$$

where Θ represents the time-reversal operator with the property $\Theta^2 = -1$. The

partial polarization associated with the splitting $s = \mathrm{I}, \mathrm{II}$ is denoted as

$$P^s = \frac{1}{2\pi}\int_{-\pi}^{\pi} \mathrm{d}k \mathcal{A}^s(k) \tag{1.30}$$

where,

$$\mathcal{A}^s(k) = i\sum_{\alpha}\langle \Psi^s_{k,\alpha}|\nabla_k|\Psi^s_{k,\alpha}\rangle. \tag{1.31}$$

The $\mathbb{Z}_2$ invariant is defined as the difference between the partial polarizations, namely, the time-reversal polarization, denoted by $P_\theta = P^{\mathrm{I}} - P^{\mathrm{II}}$. Since the system exhibits time-reversal invariance, only the integration over half a period is necessary to compute this invariant. Consequently, the $\mathbb{Z}_2$ invariant for such time-reversal invariant systems can be precisely expressed as,

$$\nu = [P_\theta(T/2) - P_\theta(0)] \mod 2. \tag{1.32}$$

We have used Eq. 1.32 for computing the $\mathbb{Z}_2$ invariant in this thesis.

1.2 Topological Insulator

Earlier we have mentioned two topological invariants which depends on the TRS. However, the topological phases may also depend on other symmetries, such as the chiral symmetry, particle-hole symmetry etc. To have a clear insight, we present a periodic table of topological insulators [157] as shown in table 1.1. This is also known as the periodic table for topological insulators and superconductors. The operators for time-reversal, particle-hole and chiral symmetries are denoted by Θ, Ξ and Π respectively. The dimension of the system is denoted by d. The values ± 1 and zero in each symmetry column are obtained by squaring the respective unitary operators. For example, $\Theta^2 = \pm 1$ represent the presence of TRS, while $\Theta^2 = 0$ implies the absence of TRS. The topological phases in each symmetry class are denoted by the invariants $\mathbb{Z}$, $\mathbb{Z}_2$ and zero. It should be noted that in the periodic table, the Chern numbers and the winding numbers are denoted by $\mathbb{Z}$. However, we have used C to denote the Chern number throughout the thesis.

Our work is based on two different systems. One is the class A Haldane

TABLE. 1.1: The periodic table [157] for topological insulators and superconductors is presented. The ten symmetry classes are denoted using Altland Zirnbauer notation [158]. The classification depends on the TRS, the particle-hole symmetry and the chiral symmetry whose operators are denoted by θ, Ξ and Π respectively. ± 1 and 0 in the symmetry column denote the presence and absence of symmetry respectively and the values are obtained upon squaring the operators. d denotes the dimension of the system and topological invariants are $\mathbb{Z}$ and $\mathbb{Z}_2$ which repeat in $d+8$ interval. Adopted from Ref. [157].

	Symmetry			d							
AZ	Θ	Ξ	Π	1	2	3	4	5	6	7	8
A	0	0	0	0	$\mathbb{Z}$	0	$\mathbb{Z}$	0	$\mathbb{Z}$	0	$\mathbb{Z}$
AIII	0	0	1	$\mathbb{Z}$	0	$\mathbb{Z}$	0	$\mathbb{Z}$	0	$\mathbb{Z}$	0
AI	1	0	0	0	0	0	$\mathbb{Z}$	0	$\mathbb{Z}_2$	$\mathbb{Z}_2$	$\mathbb{Z}$
BDI	1	1	1	$\mathbb{Z}$	0	0	0	$\mathbb{Z}$	0	$\mathbb{Z}_2$	$\mathbb{Z}_2$
D	0	1	0	$\mathbb{Z}_2$	$\mathbb{Z}$	0	0	0	$\mathbb{Z}$	0	$\mathbb{Z}_2$
DIII	-1	1	1	$\mathbb{Z}_2$	$\mathbb{Z}_2$	$\mathbb{Z}$	0	0	0	$\mathbb{Z}$	0
AII	-1	0	0	0	$\mathbb{Z}_2$	$\mathbb{Z}_2$	$\mathbb{Z}$	0	0	0	$\mathbb{Z}$
CII	-1	-1	1	$\mathbb{Z}$	0	$\mathbb{Z}_2$	$\mathbb{Z}_2$	$\mathbb{Z}$	0	0	0
C	0	-1	0	0	$\mathbb{Z}$	0	$\mathbb{Z}_2$	$\mathbb{Z}_2$	$\mathbb{Z}$	0	0
CI	1	-1	1	0	0	$\mathbb{Z}$	0	$\mathbb{Z}_2$	$\mathbb{Z}_2$	$\mathbb{Z}$	0

model [16], which is characterized by the non-zero Chern number that denotes chiral edge modes. The two-dimensional system that shows quantum Hall state, belongs to this symmetry class. The other one we have studied is the Kane-Mele model [113] which belongs to class AII symmetry and has non-zero $\mathbb{Z}_2$ topological invariant. This in turn implies the presence of the helical edge modes in a system with open boundaries and demonstrates quantum spin Hall phase.

There are also other topological insulators in different dimensions that have entries in the periodic table, such as, a quantum Hall state in $d = 4$ dimensions that belongs to class A or AII symmetries [148], a $\mathbb{Z}$ invariant superfluid ^{3}HeB that belongs to the DIII symmetry class in $d = 3$ dimensions [149–154], SSH model of BDI symmetry in $d = 1$ dimension [155], the $\mathbb{Z}_2$ ($d = 1$) and $\mathbb{Z}$ ($d = 2$) topological superconductors [156] of class D etc. However, these have not been explored in this thesis.

1.3 Spin-orbit coupling

The spin-orbit interaction is the coupling between the spin and the orbital angular momentum of a particle. This interaction leads to the splitting of degenerate energy levels. It arises due to the presence of a magnetic field or an electric field. When an electron moves in a magnetic field, it experiences a Lorentz force $\mathbf{F} = -e\mathbf{p} \times \mathbf{B}/m_e$ and acquires a Zeeman energy E_{B}. Now, if an electron moves through the strong electric field of a nucleus, it would experience a magnetic field in its own inertial frame [159]. The Hamiltonian that describes such spin-orbit splitting is given by,

$$H_{\mathrm{SO}} = \frac{-\hbar}{4m_e^2c^2}\boldsymbol{\sigma} \cdot \mathbf{p} \times \boldsymbol{\nabla} V_0 \tag{1.33}$$

where m_e is the electron mass, c denotes the velocity of light, $\boldsymbol{\sigma}$ is the Pauli matrix, $\mathbf{p}$ is the momentum and V_0 is the electric potential [160]. In crystals, the above form may be approximated by,

$$H_{\mathrm{SO}} = \zeta_{\mathrm{SO}}\mathbf{L} \cdot \mathbf{S}, \tag{1.34}$$

where ζ_{SO} is the interaction strength, $\mathbf{L}$ represents the orbital angular momentum operator and $\mathbf{S}$ denotes the spin angular momentum operator [160]. The corresponding energies of this Hamiltonian are non-degenerate. Hence, the SOC leads to the formation of energy sub-levels that exhibit different energies depending on the orientation of the total angular momentum vector. This phenomenon is known as fine structure splitting.

There are different types of spin-orbit coupling, such as, Dresselhaus spin-orbit coupling [161, 162], Rashba spin-orbit coupling [115] etc. Our main focus is the Rashba spin-orbit coupling which we shall explain in the following section.

1.3.1 Rashba spin-orbit coupling

If an electron experiences a strong electric field, or the potential gradient, then another spin-orbit interaction takes place. Such potential gradient exists in two dimensional system because of lack of inversion symmetry. The advantage of such confinement potential is that one can control it by means of an external

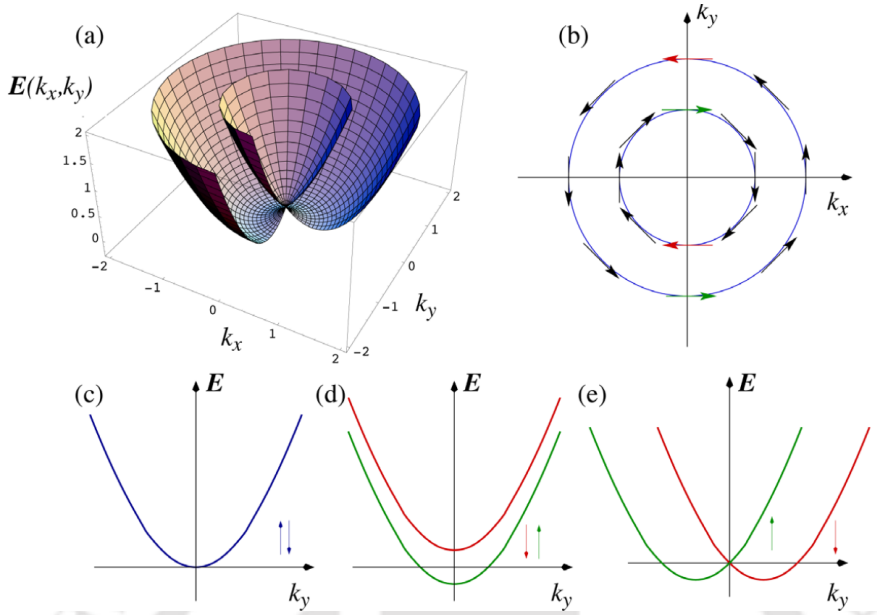

FIG. 1.4: The energy spectra of 2DEG in the presence of RSOC are shown in (a). In (b), the Fermi energy contours are depicted. The energy spectra in the absence of both RSOC and Zeeman energy are presented in (c), in the presence of Zeeman energy in (d), and in the presence of RSOC in (e). These figures are adopted from Ref. [164].

gate voltage, which finally allows one to tune the spin-orbit coupling (SOC). This type of SOC was first proposed by E. I. Rashba in 1960 [115] and is known as Rashba SOC. It may be noted that the magnitude of RSOC also relies on the crystal composition found in quantum wells, exhibiting its maximum value in narrow gap III - V semiconductors such as InGaAs, InAs etc. In the following, we have described a short derivation for the RSOC in a continuum model.

The Rashba Hamiltonian for a two-dimensional electron gas (2DEG) can be described using the following form [115].

$$H_{\mathrm{R}} = \alpha_{\mathrm{R}}(\boldsymbol{\sigma} \times \mathbf{p}) \cdot \hat{\mathbf{z}} \tag{1.35}$$

where α_{R} is the strength of the SOC, $\boldsymbol{\sigma} = (\sigma_x, \sigma_y, \sigma_y)$ denote the spin-1/2 Pauli matrices and $\mathbf{p} = -i\hbar\boldsymbol{\nabla}$ is the momentum operator. In the absence of any Zeeman coupling and elastic scattering, the total Hamiltonian reads,

$$H = \frac{\mathbf{p}^2}{2m} + \alpha_{\mathrm{R}}(\boldsymbol{\sigma} \times \mathbf{p}) \cdot \hat{\mathbf{z}} = \frac{p_x^2 + p_y^2}{2m} + \alpha_{\mathrm{R}}(\sigma_x p_y - \sigma_y p_x) \tag{1.36}$$

The diagonalization of the above Hamiltonian gives the following energy spectrum [163].

$$E(\mathbf{k}) = \frac{\hbar^2\mathbf{k}^2}{2m} \pm \alpha_{\mathrm{R}}\hbar|\mathbf{k}| \tag{1.37}$$

where $|k| = \sqrt{k_x^2 + k_y^2}$ and the $\pm$ sign refers to two different spin-filtered bands. The associated eigen vectors of the Hamiltonian corresponding to the bands are given by,

$$\psi = e^{i(k_x x + k_y y)} \frac{1}{\sqrt{2}} \begin{pmatrix} 1 \\ \pm i e^{-i\theta} \end{pmatrix} \tag{1.38}$$

where $\theta = \tan^{-1}\frac{k_y}{k_x}$. It may be noted that the spin states are orthogonal to the direction of motion. When an electron traverses in the x-direction, the spinor component of the eigenvector assumes the form $(1,\ i)$, implying that the spin up and spin down are entangled in the y-direction. Conversely, when the electron moves along the y-direction, the eigenvectors take the form $(1,\ 1)$, indicating that the spin up and spin down states are confined within the x-direction (refer to Fig. 1.4).

The three dimensional depiction of the energy spectra corresponding Eq. 1.37 is shown in Fig. 1.4(a). While in Figs. 1.4(c)-1.4(e), the spectra is shown as a function of k_y and k_x being fixed at zero. When $\alpha_{\mathrm{R}} = 0$, there is no splitting of energy, that is, the bands are degenerate and coincide with each other (see Fig. 1.4(c)). The degeneracies are lifted in presence of an external magnetic field and the splitting is known as the Zeeman splitting (see Fig. 1.4(d)). RSOC also removes the spin degeneracy with the exception at $k_y = 0$ as presented in Fig. 1.4(e), however, it does not open any gap. Fig. 1.4(b) demonstrates the Fermi energy with the spin states.

1.4 Anomalous Hall conductivity

The anomalous Hall conductivity appears to be non-zero when the system has a non-zero Chern number. The term 'anomalous' is added to distinguish it from the original Hall conductivity which arises due to the presence of the magnetic field. In our work we have not included any magnetic field, and so we have dealt with

anomalous Hall conductivity. To compute it, we first obtain the Berry curvature, $\Omega_z(k_x, k_y)$ of a system using either Eq. 1.10 or Eq. 1.15, and then use the following formula [165–167],

$$\sigma_{xy} = \frac{\sigma_0}{2\pi} \sum_{\lambda} \int_{\text{occ.}} \frac{\mathrm{d}k_x \mathrm{d}k_y}{(2\pi)^2} f\left[E_\lambda(k_x, k_y)\right] \Omega_z(k_x, k_y) \tag{1.39}$$

where $E_\lambda(k_x, k_y)$ denotes the electronic energies with λ being the band index. $\sigma_0 (= e^2/h)$ sets the scale for σ_{xy}. $f[E]$ is the Fermi-Dirac distribution function which has the following form:

$$f[E] = \frac{1}{1 + e^{\beta(E - E_F)}}$$

where E_F is the Fermi energy and $\beta = 1/(k_B T)$ is the inverse temperature. It should be noted that the summation in Eq. 1.39 is taken over all the bands. For example, in the case of dice lattice we have three bands and hence we calculate the Berry curvature for all the three bands. After that the integration is carried out over the occupied states, that is, the states below the Fermi level, E_F are taken into account.

1.5 Graphene

Throughout this thesis, we have performed calculations on a 2D honeycomb lattice (and its variations), which forms a paradigmatic model for graphene. A short discussion on graphene and the *Berry-o-logy* associated with it yields a smooth connection to the main objective of the thesis.

Graphene is two-dimensional carbon allotrope with the honeycomb lattice structure. It is the first two-dimensional material and was discovered by Novoselov *et al* in 2004 [168]. The carbon atoms in graphene are sp^2 hybridized, which means the atoms are σ-bonded in a planar triangular manner which is responsible for the honeycomb structure. Moreover, graphene exhibits remarkable mechanical and thermal properties. It is the strongest material ever measured, with a tensile strength reaching approximately 120 GPa [169]. Its high thermal

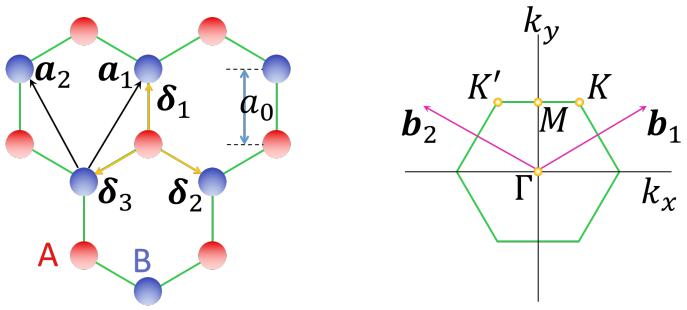

FIG. 1.5: In the left panel, the lattice structure of graphene is shown, where the red and blue circles represent the A and B sublattices respectively. The Brillouin zone is depicted in the right panel.

conductivity of $\sim$ 5000 W/(m·K) makes it a promising candidate for thermal applications [170]. Further, the high carrier mobility [171] and ballistic transport properties of graphene make it a potential candidate for conventional silicon-based materials in high-speed transistors [172] and integrated circuits [173]. These astounding properties of graphene allows one to implement it in electronics [174], photonics [175], energy storage devices [176], biosensors [177], batteries [178] etc.

Now, we describe the crystal structure of graphene. It is hexagonal with two atoms per unit cell. We have denoted them as A and B sublattices as shown in the left panel of Fig. 1.5. We can write the primitive lattice vectors in different ways. We show one of them by the black arrows $\mathbf{a}_1$ and $\mathbf{a}_2$ in Fig. 1.5, which are given by,

$$\mathbf{a}_1 = \frac{a_0}{2}\left(\sqrt{3}, 3\right); \quad \mathbf{a}_1 = \frac{a_0}{2}\left(-\sqrt{3}, 3\right) \tag{1.40}$$

where a_0 is the nearest neighbour distance. The values of a_0 for graphene is $a_0 = 1.42\text{Å}$ [179]. The nearest neighbour vectors, $\boldsymbol{\delta}_i$s are defined to point from A to B sublattice and are written as follows.

$$\boldsymbol{\delta}_1 = a_0(0, 1); \quad \boldsymbol{\delta}_2 = \frac{a_0}{2}\left(\sqrt{3}, -1\right); \quad \boldsymbol{\delta}_3 = \frac{a_0}{2}\left(-\sqrt{3}, -1\right) \tag{1.41}$$

The reciprocal lattice vectors are denoted by $\mathbf{b}_1$ and $\mathbf{b}_2$ which are given by,

$$\mathbf{b}_1 = \frac{2\pi}{3a_0}\left(\sqrt{3}, 3\right); \quad \mathbf{b}_2 = \frac{2\pi}{3a_0}\left(-\sqrt{3}, 3\right) \tag{1.42}$$

The first Brillouin zone (BZ) of graphene is also hexagon as shown in the right panel of Fig. 1.5. The special points in the BZ are shown via $\mathbf{\Gamma}$, $\mathbf{K}$, $\mathbf{M}$ and $\mathbf{K}'$ points which are,

$$\mathbf{\Gamma} = (0,0);\ \ \mathbf{K} = \left(\frac{2\pi}{3\sqrt{3}a_0}, \frac{2\pi}{3a_0}\right);\ \ \mathbf{M} = \left(0, \frac{2\pi}{3a_0}\right);\ \ \mathbf{K}' = \left(-\frac{2\pi}{3\sqrt{3}a_0}, \frac{2\pi}{3a_0}\right) \quad 1.43$$

The locations are shown by yellow dots in the BZ. We shall describe the importance of such special points later in the discussion of band structure. Owing to large kinetic energy of the electrons (and one conduction electron per C atom), a tight-binding description suits the best.

The tight-binding Hamiltonian of graphene can be written as,

$$H = t\sum_{\langle ij\rangle}(c_i^\dagger c_j + \text{h.c.}) \quad 1.44$$

where $\langle ij\rangle$ denotes the two nearest neighbour (NN) sites with indices i and j, $c_i^\dagger(c_i)$ is the creation (annihilation) operator corresponding to site i. Now, we Fourier transform the operators in order to compute the dispersion relation, using the following form,

$$c_{\mathbf{k}} = \frac{1}{\sqrt{N}}\sum_i e^{-i\mathbf{k}\cdot\mathbf{r_i}}c_i \quad 1.45$$

It yields the following form of the Hamiltonian in momentum space,

$$\begin{aligned} H(\mathbf{k}) &= h_x(\mathbf{k})\sigma_x + h_y(\mathbf{k})\sigma_y \\ &= \mathbf{h}(\mathbf{k})\cdot\boldsymbol{\sigma} \end{aligned} \quad 1.46$$

where σ_is are the 2×2 Pauli matrices and h_is have following expressions,

$$h_x(\mathbf{k}) = \left\{ t\cos k_y + 2t\cos\frac{k_y}{2}\cos\frac{\sqrt{3}k_x}{2} \right\} \quad 1.47$$

$$h_y(\mathbf{k}) = \left\{ -t\sin k_y + 2t\sin\frac{k_y}{2}\cos\frac{\sqrt{3}k_x}{2} \right\} \quad 1.48$$

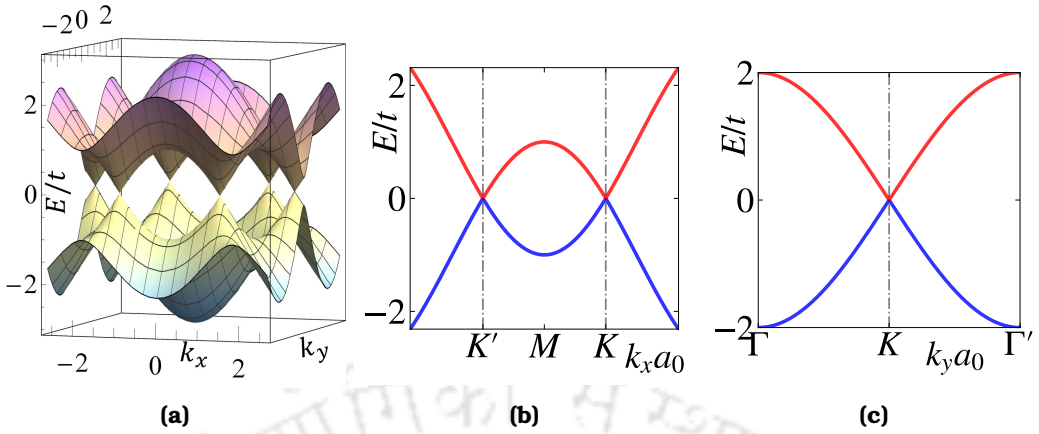

FIG. 1.6: The band structure of graphene is shown in (a) where the bands touch each other at six points. Two-dimensional depictions of the band structure are presented in (b) and (c) which are along the k_x and k_y axes respectively. In (b), the value of $k_y a_0$ is fixed at $2\pi/3$, while in (c), the value of $k_x a_0$ is fixed at zero.

By diagonalizing the above Hamiltonian, we get the dispersion relation as

$$E_{\pm}(\mathbf{k}) = \pm t\sqrt{3 + 2\cos(\sqrt{3}ak_x) + 4\cos(\sqrt{3}ak_x/2)\cos(3ak_y/2)} \qquad 1.49$$

where the $\pm$ sign refers to the conduction and valence bands respectively. We plot the band structure in Fig. 1.6. As can be seen, there are six points in the Brillouin zone (BZ), where the conduction band touches the valence band. However, only two points are important and they are denoted as the $\mathbf{K}$ and the $\mathbf{K}'$ points. The rest four points can be obtained from these two points using a combination of the reciprocal lattice vectors (see Eq. 1.42). Further, the band structure about these points are linear at the low energies, and hence the electron behave as a massless Dirac Fermions. The velocities are found to be 300 times lower than the speed of light.

Further, to obtain a low energy dispersion, one may use the Taylor series expansion about the $\mathbf{K}$ and the $\mathbf{K}'$ points. This yields the following form of the Hamiltonian.

$$H_{\mathbf{K},\mathbf{K}'} = v_F(\tau_z\, q_x\, \sigma_x + q_y\, \sigma_y) \qquad 1.50$$

where $\mathbf{q}$ is the small momentum about the $\mathbf{K}$ and $\mathbf{K}'$ points, that is, $\mathbf{q} = \mathbf{k} - \mathbf{K}$ (or $\mathbf{k} - \mathbf{K}'$). τ_z has values ± 1 which represent two different valleys ($\mathbf{K}$ and $\mathbf{K}'$) and

$v_F = 3ta_0/2$ is the velocity of the electrons. The corresponding eigensolutions are,

$$E_{\pm}(\mathbf{q}) = \pm v_F|q|; \quad \Psi_{\pm}(\mathbf{q}) = \frac{1}{\sqrt{2}}\begin{pmatrix} 1 \\ \pm e^{i\theta_q} \end{pmatrix} \tag{1.51}$$

where $\theta_q = \tan^{-1}(q_y/q_x)$. The above dispersion verifies the fact that the band structure is linear along both k_x and k_y directions (see Figs. 1.6(b) and 1.6(c)).

Now we compute the topological invariant of the system. First we evaluate the expression for Berry connection using Eq. 1.7 and the low energy eigenvector corresponding to Eq. 1.51. Since, the low energy spectrum shows circular symmetry, $\boldsymbol{\nabla_q}$ may be taken as, $\boldsymbol{\nabla_q} = \hat{q}\frac{\partial}{\partial q} + \hat{\theta}_q \frac{1}{q}\frac{\partial}{\partial \theta_q}$. The Berry connection is given by,

$$\begin{aligned} \mathcal{A}_{\pm} &= i\left\langle \Psi_{\pm}\right| \hat{q}\frac{\partial}{\partial q} + \hat{\theta}_q \frac{1}{q}\frac{\partial}{\partial \theta_q} \left|\Psi_{\pm}\right\rangle \\ &= \frac{i}{2}\left\langle \begin{pmatrix} 1 & \pm e^{-i\theta_q} \end{pmatrix} \middle| \begin{pmatrix} 0 \\ \pm ie^{i\theta_q}\ \hat{\theta}_q \end{pmatrix} \right\rangle = \mp\frac{1}{2}\frac{\hat{\theta}_q}{q} \end{aligned} \tag{1.52}$$

Now the Berry phase for graphene can be computed using the line integral of Eq. 1.6.

$$\Phi_B = \mp \oint_{\mathcal{L}} \frac{1}{2}\frac{\hat{\theta}_q}{q} \mathrm{d}\boldsymbol{\zeta} = \mp \int_0^{2\pi} \frac{1}{2}\frac{\hat{\theta}_q}{q} \cdot (\mathrm{d}q\ \hat{q} + q\ \mathrm{d}\theta_q\ \hat{\theta}_q) = \mp \int_0^{2\pi} \frac{1}{2}\frac{\mathrm{d}\theta_q}{q} = \mp\pi \tag{1.53}$$

where the path $\mathcal{L}$ is circular around the $\mathbf{K}$ point and $\mathrm{d}\zeta$ denotes the infinitesimal momentum vector. We obtain $\Phi_B = \mp\pi$ for the conduction and valence bands respectively. Similarly, when we consider the $\mathbf{K}'$ point, Φ_B has the same magnitude but with opposite signs [180]. This aids us in defining a topological charge which is ± 1 at the two Dirac points.

1.5.1 Cyclotron effective mass for graphene

Here we calculate the cyclotron mass of the electrons which depends on the band dispersion. The cyclotron mass [181] is calculated by obtaining the area of the orbit corresponding to a particular energy described by the particle and can be

expressed as [182],

$$m^* = \frac{\hbar^2}{2\pi}\left(\frac{\partial S(E)}{\partial E}\right) \tag{1.54}$$

where $S(E)$ is the area enclosed by the particle trajectory expressed as a function of the electron energy. Since the dispersion is isotropic, the trajectory electrons become circular. Therefore, the area of the orbit is $S(E) = \pi E^2/v_F^2$. This yields the effective mass to be proportional to E, namely,

$$m^* = \frac{\hbar^2 E}{v_F^2}. \tag{1.55}$$

This linear dependence of m^* on E or rather on the momentum k has been observed in graphene by imaging the cyclotron orbit in scanning microscopy experiments [183, 184].

1.6 Haldane model

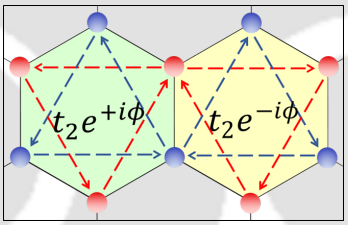

FIG. 1.7: This figure demonstrates the direction dependent complex NNN hopping. For NNN hopping in the clockwise (counter-clockwise) direction ϕ is positive (negative).

Now we discuss the Haldane model which demonstrates the quantum Hall effect without an external magnetic field [16]. Only requirement is to break the time reversal symmetry of the system, which was done by adding a complex next-nearest neighbour (NNN) hopping in the honeycomb lattice. The Hamiltonian of the system in presence of such hopping can be written as,

$$H = \left[t\sum_{\langle ij\rangle} c_i^\dagger c_j + t_2 \sum_{\langle\langle ik\rangle\rangle} e^{i\phi_{ik}} c_i^\dagger c_k + \text{h.c.}\right] + \Delta\sum_i \xi_i c_i^\dagger c_i \tag{1.56}$$

where the first term is the NN hopping as described in Eq. 1.44, the second term is the complex NNN hopping (refer to Fig. 1.7) with an amplitude t_2 and phase

ϕ_{ik}. The sign of ϕ_{ik} depends on the direction of the hopping and can be computed from the relation of $\mathrm{sgn}(\mathbf{d}_{ij} \times \mathbf{d}_{jk})_z$. Here $\mathbf{d}_{ij}$ is a vector that connects site i to its NN site j. This implies that ϕ acquires a positive (negative) value when the electron hops in the anticlockwise (clockwise) direction. The term $e^{\phi_{ik}}$ breaks the TRS since it flips the direction of hopping. The third term is the onsite potential (also known as Semenoff mass) where $\xi_i = \pm 1$ alters the sign of potential Δ at the A and B sublattices respectively. Now, we Fourier transform the operators to write the Hamiltonian in momentum space as follows.

$$H(\mathbf{k}) = h_x(\mathbf{k})\sigma_x + h_y(\mathbf{k})\sigma_y + h_z(\mathbf{k})\sigma_z + h_0(\mathbf{k})\sigma_0 = \mathbf{h}(\mathbf{k}) \cdot \boldsymbol{\sigma} + h_0(\mathbf{k})\sigma_0 \qquad 1.57$$

where σ_z is the z-component of the Pauli matrix and σ_0 is the 2×2 identity matrix. The expressions for h_x and h_y are identical to Eqs. 1.47 and 1.48 respectively, while those for h_z and h_0 are given by,

$$h_z(\mathbf{k}) = \Delta - 2t_2 \sin\phi \left\{ 2\sin\frac{\sqrt{3}k_x}{2}\cos\frac{3k_y}{2} - \sin\sqrt{3}k_x \right\} \qquad 1.58$$

and,

$$h_0(\mathbf{k}) = 2t_2 \cos\phi \left\{ 2\cos\frac{\sqrt{3}k_x}{2}\cos\frac{3k_y}{2} + \cos\sqrt{3}k_x \right\}. \qquad 1.59$$

The dispersion relation can be written as,

$$E(\mathbf{k}) = h_0(\mathbf{k}) \pm \sqrt{h_x(\mathbf{k})^2 + h_y(\mathbf{k})^2 + h_z(\mathbf{k})^2}, \qquad 1.60$$

Now, we calculate the energy as a function of k_x and k_y, and show the band structure in Fig. 1.8. The values of ϕ is taken to be $\pi/2$ where the NNN hoppings become purely imaginary, and also the particle hole symmetry remains preserved. For the moment we keep Δ at zero, and later we will see how Δ changes the band structure. From Fig. 1.8, it is clear that gaps open up at the Dirac points and hence the system becomes an insulator. The magnitude of the gap can be obtained by substituting the momenta corresponding to the $\mathbf{K}$ and $\mathbf{K}'$ points in

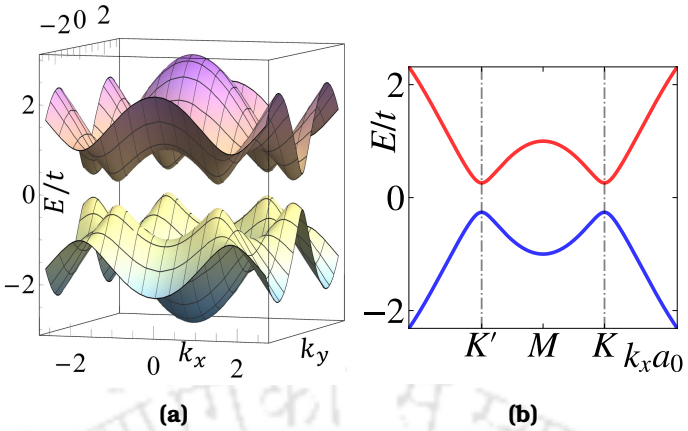

FIG. 1.8: A 3D band structure corresponding to the Haldane model is depicted in (a), showcasing the presence of gaps at six Dirac points. In (b), a 2D depiction of the band structure as a function of $k_x a_0$ is presented, with $k_y a_0$ fixed at $2\pi/3$.

the dispersion relation given in Eq. 1.60. It can also be checked by evaluating the low energy Hamiltonian about the Dirac points given by,

$$H_{\mathbf{K},\mathbf{K}'} = v_F(\tau_z q_x \sigma_x + q_y \sigma_y) + (\beta\tau_z + \Delta)\sigma_z \tag{1.61}$$

where $\tau_z = \pm 1$ refers to the $\mathbf{K}$ and the $\mathbf{K}'$ points, and $\mathbf{q}$ is the small momenta about these points. $\beta = 3\sqrt{3}t_2 \sin\phi$ is independent of momenta and describes the amount of the gap. The low energy dispersion is given by,

$$E_{\pm}(\mathbf{q}) = \pm\sqrt{v_F^2 q_x^2 + v_F^2 q_y^2 + (\beta\tau_z + \Delta)^2} \tag{1.62}$$

This dispersion relation clarifies that the amount of band gap is $2\beta = 6\sqrt{3}t_2$ when $\Delta = 0$. The bandwidth still remains at $6t$ similar to the case of graphene. Once we switch on Δ, an imbalance in the band gap is induced since τ_z takes opposite signs at the two valleys. Hence, by tuning Δ, one can close the energy gap at only one valley while keeping the gap at other valley opened. We have discussed this in the subsequent section, after the discussion of the Berry curvature.

1.6.1 Berry curvature

Here we compute the Berry curvature, Ω numerically using Eq. 1.10. The corresponding spectrum is shown in Fig. 1.9 for various values of Δ and t_2. It may be

noticed that Ω is highly concentrated around the Dirac points, that is, around the maxima positions of the valence bands. For $t_2 = 0$ and $\Delta \neq 0$, the magnitudes at the $\mathbf{K}$ and $\mathbf{K}'$ points are equal, but have opposite signs (see Fig. 1.9(a)). Since the Semenoff mass Δ breaks the inversion symmetry, it creates an imbalance in Ω at the two Dirac points. If we switch on t_2 for $\Delta = 0$, Ω acquires identical magnitudes and same sign at the $\mathbf{K}$ and the $\mathbf{K}'$ points (see Fig. 1.9(b)). Now we keep t_2 fixed and turn on Δ, and Ω becomes unequal at the $\mathbf{K}$ and the $\mathbf{K}'$ points as shown in Fig. 1.9(c). The reason for getting such unequal amplitudes is that the band gap is lesser at the $\mathbf{K}$ point as compared to that at the $\mathbf{K}'$ point, and Ω depends on the band gap. When Δ flips its sign, the gap at the $\mathbf{K}'$ point becomes larger, and hence Ω has a greater value at the $\mathbf{K}'$ point as compared to that at the $\mathbf{K}$ point (see Fig. 1.9(d)).

These were the calculations from the full tight-binding Hamiltonian. However, an analytical expression of Ω can be obtained from the low energy Hamiltonian in Eq. 1.61. First we rewrite the eigen systems of the Hamiltonian as follows.

$$\Psi_{\pm}(\mathbf{q}) = \frac{1}{\sqrt{2}} \begin{bmatrix} \sqrt{1 + \frac{\beta}{E_{\pm}}} \\ \pm\sqrt{1 - \frac{\beta}{E_{\pm}}} e^{i\theta_q} \end{bmatrix} ; \; E_{\pm}(\mathbf{q}) = \pm\sqrt{v_F^2 q_x^2 + v_F^2 q_y^2 + \beta^2} \tag{1.63}$$

where $\theta_q = \tan^{-1}(q_x/q_y)$. Now we use Eq. 1.15 to obtain the following expressions for Ω, namely,

$$\Omega_{\pm}(\mathbf{q}) = \pm \frac{v_F^2(\beta + \tau_z\Delta)}{2\left[v_F^2 q_x^2 + v_F^2 q_y^2 + (\tau_z\beta + \Delta)^2\right]^{\frac{3}{2}}} \tag{1.64}$$

where the $\pm$ sign refers to the conduction and the valence bands respectively. The above equation clarifies the fact that Ω is maximum around the $\mathbf{K}$ and the $\mathbf{K}'$ points as can be checked by substituting $q_x = q_y = 0$. The value of Ω diminishes as one goes away from those points. Further, when $\beta = 0$ (or $t_2 = 0$), Ω acquires opposite signs at the $\mathbf{K}$ and the $\mathbf{K}'$ points as described earlier.

Further, the expressions for the Berry connection can be evaluated using Eq. 1.7 and is given by,

$$\boldsymbol{\mathcal{A}}_{\pm} = \pm\frac{1}{2}\left(1 \pm \frac{\beta + \tau_z\Delta}{|E_{\pm}|}\right)\frac{\hat{\theta}_q}{q} \tag{1.65}$$

Finally the Berry phase can be computed using Eq. 1.6 which yields $\Phi_B = \mp 2\pi$.

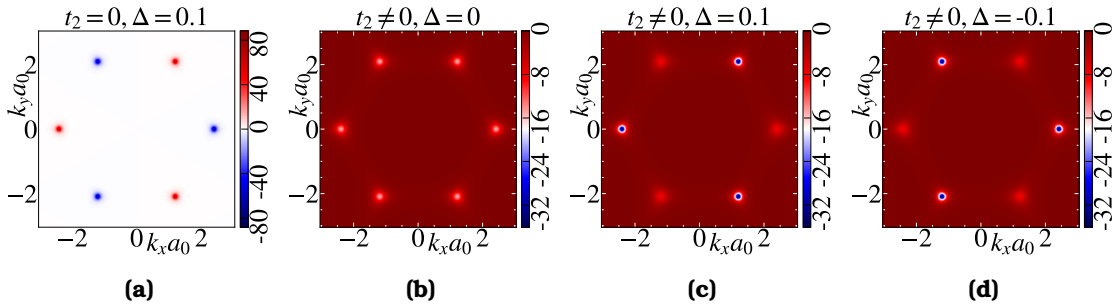

FIG. 1.9: The Berry curvature is plotted in absence of t_2 in (a) for $\Delta = 0.1t$. In (b), (c), and (d), the Berry curvature is shown for a non-zero t_2 with $\Delta = 0$, $\Delta = 0.1t$, and $\Delta = -0.1t$, respectively. The value of ϕ is fixed at $\pi/2$.

1.6.2 Chern number: Phase diagram

In this section, we check the nature of the band gap by calculating the Chern number of the system. It is done by integrating the Berry curvature obtained numerically using Eq. 1.17 over the first BZ. It is found that the Chern number has a value $C = 1$ in this case. As long as the NNN hopping retains its imaginary part, that is, for $0 < \phi < \pi$, C remains at one. At $\phi = 0$ and $\phi = \pi$, only the real part of NNN hopping term is included in the Hamiltonian (since $e^{i\phi} = 1$ for $\phi = 0$ and $\phi = \pi$) which switches off $h_z(\mathbf{k})$ in Eq. 1.58 and the system becomes a semi-metal. For $-\pi < \phi < 0$, the Chern number reverses its sign ($C = -1$), since $h_z(\mathbf{k})$ reverses its sign which result in the sign change of the Berry curvature. This implies that $C = -1$ for $(2n+1)\pi < \phi < (2n+2)\pi$ and $-(2n+1)\pi < \phi < -2n\pi$, while $C = +1$ for $2n\pi < \phi < (2n+1)\pi$ and $-(2n+2)\pi < \phi < -(2n+1)\pi$ with $n = 0, 1, 2, \ldots$.

Further, we incorporate the onsite potential Δ to observe the interplay of topological phases between Δ and the Haldane flux ϕ. Hence we obtain the Chern number phase diagram in the $\Delta - \phi$ plane which is shown in Fig. 1.10(a). As can be seen, there are two coloured regions. The one in cyan in $\phi > 0$ region represents the $C = +1$ phase, while the red one in $\phi < 0$ region denotes the $C = -1$ phase. The white region signifies the trivial insulating regime with $C = 0$. There exists a semi-metallic phase between the trivial and non-trivial regimes in the phase diagram. This is shown by purple curve. The equations of these curves are given by,

$$\Delta/t_2 = \pm 3\sqrt{3}\sin\phi \qquad 1.66$$

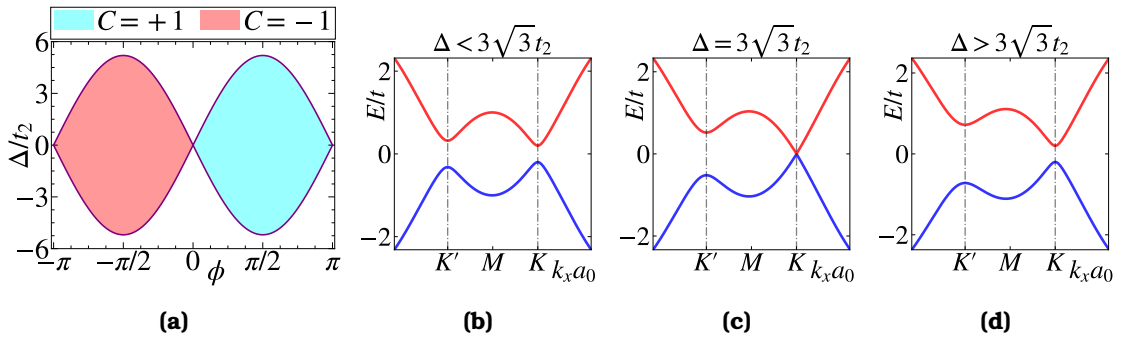

FIG. 1.10: The phase diagram corresponding to the Haldane model is presented in (a). The red and cyan regions represent the non-trivial phase with Chern numbers $C = -1$ and $C = +1$, respectively. The white region denotes the trivial phase with a zero Chern number. The band structures for three different values of Δ are presented in (b) for $\Delta < 3\sqrt{3}t_2$, (c) for $\Delta = 3\sqrt{3}t_2$, and (d) for $\Delta > 3\sqrt{3}t_2$. The value of ϕ for these three band structures is taken as $\pi/2$.

Here the term $3\sqrt{3}$ multiplied by t_2 represent the magnitude of half-energy gap when $\phi = \pi/2$. Therefore, at $\phi = \pi/2$, if we keep $\Delta = 3\sqrt{3}t_2$, then the gap at the **K** point closes and the system becomes a semi-metal as shown in Fig. 1.10(c). For $\Delta > 3\sqrt{3}t_2$, the gap opens up again (see Fig. 1.10(d)) and the system becomes an insulator. For a negative value of Δ, the gap closes at the **K′** point. The computation of Chern number shows that for $\Delta < |3\sqrt{3}t_2|$ the Chern number has value one ($C = 1$), that is, the system is a topological insulator. While for $\Delta > |3\sqrt{3}t_2|$ the Chern number vanishes and system becomes a trivial insulator.

1.6.3 Cyclotron effective mass for Haldane model

We calculate the cyclotron mass of the electrons using the following relation [182],

$$m^* = \frac{\hbar^2}{2\pi}\left(\frac{\partial S(E)}{\partial E}\right) \tag{1.67}$$

where $S(E)$ is the area enclosed by the particle trajectory expressed as a function of the electron energy. The dispersion spectra of the Haldane model is isotropic at the low energies. Hence, the isoenergy contours are circular whose area is $S(E) = \pi(E^2 - \beta^2)/v_F^2$. Therefore the effective mass can be obtained as,

$$m^* = \frac{\hbar^2 E}{v_F^2}. \tag{1.68}$$

This linear dependence of m^* on E is identical to that observed in graphene. It can be noticed that although the NNN hopping t_2 is non-zero, however, the effective mass is still linear in E. This is because the band structure is isotropic at the low energies for both graphene and the Haldane model.

1.7 Kane-Mele model

So far we have not included the electronic spin in the calculation. In this section, we incorporate that in the Haldane model, which yields a wonderful dividend, namely, bringing back TRS, as we shall see later. It was first done by Kane and Mele [113, 114] whose tight-binding Hamiltonian can be written as,

$$H = t\sum_{\langle ij\rangle} c_i^\dagger c_j + i\lambda_{\rm SO}\sum_{\langle\langle il\rangle\rangle}\chi_{il}c_i^\dagger s_z c_l + i\lambda_{\rm R}\sum_{\langle ij\rangle} c_i^\dagger(\mathbf{s}\times\hat{\mathbf{d}}_{ij})_z c_j + \lambda_{\rm v}\sum_i \xi_i c_i^\dagger c_j \quad \text{1.69}$$

where the first term is the NN hopping which was already appeared in graphene and Haldane model. Here the operator $c_i^\dagger$ consists of two spinor operators and are written as, $c_i^\dagger \equiv (c_{i\uparrow}^\dagger \;\; c_{i\downarrow}^\dagger)$. The second term represents the NNN hopping similar to the Haldane model. However, the quantity ϕ_{il} is replaced by $\frac{\pi}{2}\chi_{il}$. This means that the flux is taken to be $\pi/2$, and the magnitude of χ_{il} follows the same rule described by ϕ_{il} in the Haldane model (refer to the description of Eq. 1.56 in Sec. 1.6). It may be noticed that a z-component of the Pauli matrix, s_z is added in the NNN hopping term which represents the real spin degree of freedom of electrons. Because of s_z, the flux takes opposite signs corresponding to the two different spins, namely, $+\frac{\pi}{2}$ for $\uparrow$-spin and $-\frac{\pi}{2}$ for $\downarrow$-spin. This term is now called the intrinsic spin-orbit coupling term as it couples the electron spin s_z with the chirality of the electron χ_{il} and the strength is $\lambda_{\rm SO}$. The third term is the nearest-neighbour Rashba spin-orbit coupling term with the strength $\lambda_{\rm R}$. s denotes the Pauli matrix vector and $\hat{\mathbf{d}}_{ij}$ is the unit vector that connects the site i to its NN site j (direction is from site i to site j). The fourth term is the staggered sublattice potential. ξ_i is $+1$ and -1 for A and B sublattices respectively. Hence, the last term causes a sign difference in the onsite potential corresponding to two different sublattices. Therefore, except the Rashba SOC term, all the terms in the

Hamiltonian have already been appeared in the Haldane model. For $\lambda_{\rm R} = 0$, the Kane-Mele Hamiltonian can be written as a sum of Haldane Hamiltonian of two different spins, that is, $H_{\rm KM} = H^{\uparrow}_{\rm Haldane}(\phi = \pi/2) + H^{\downarrow}_{\rm Haldane}(\phi = -\pi/2)$. It is also noticeable that the NNN hopping, t_2 and the onsite potential, Δ of the Haldane model have been replaced by $\lambda_{\rm v}$ and $\lambda_{\rm SO}$ in the Kane-Mele model.

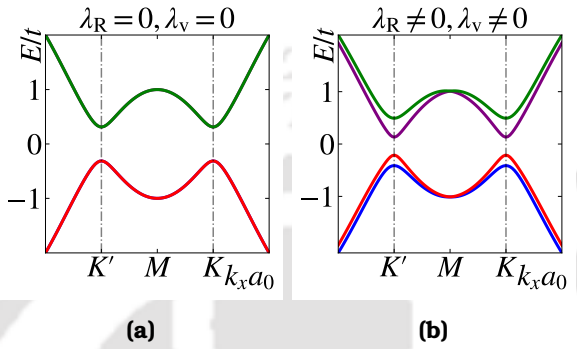

FIG. 1.11: The Band structure of Kane-Mele model is displayed for (a) $\lambda_{\rm R} = \lambda_{\rm v} = 0$ and (b) $\lambda_{\rm R} = 0.05t$, $\lambda_{\rm v} = 0.1t$.

Although the second term resembles a Haldane like term, it preserves the TRS. This is because the time-reversal operator flips the direction of hopping as well as the spins, resulting in two negative signs. Consequently, there is no net change of sign due to the time-reversal operation. To have a clear insight, we write the low energy Hamiltonian about the $\mathbf{K}$ and the $\mathbf{K}'$ points which is given by,

$$H_{\mathbf{K},\mathbf{K}'} = v_F\left(\tau_z\sigma_x q_x + q_y\sigma_y\right)s_0 + \lambda_{\rm SO}\sigma_z\tau_z s_z + \frac{\lambda_{\rm R}}{2}\left(\tau_z\sigma_x s_y - \sigma_y s_x\right) + \lambda_{\rm v}\sigma_z s_0, \quad \textbf{1.70}$$

where both $(\sigma_x, \sigma_y, \sigma_z)$ and (s_x, s_y, s_z) are 2×2 spin-1/2 Pauli matrices, however, they represent sublattice and spin degrees of freedom respectively. s_0 is a 2×2 identity matrix which again denotes the spin degree of freedom. Now, the time-reversal operator is given by, $\mathcal{T} = is_y\tau_x\kappa$. This reverses the sign of both τ_z and s_z (second term in the above Hamiltonian), but leaves σ_z unaltered, that is, under time reversal, $\tau_z \to -\tau_z$, $\sigma_z \to \sigma_z$, $s_z \to -s_z$. Therefore, there is no net change of sign in the second term and hence the TRS remains intact in the system. As a result, the system does not show any quantum Hall effect, instead it shows quantum spin Hall effect.

Before discussing such phenomenon, we first present the band structure of the

system as depicted in Fig. 1.11. There are four bands in the dispersion spectrum because of two sublattices and two spin degrees of freedom. However, when both λ_R and λ_v are zero, the conduction bands corresponding to two different spins (true for the two valence bands as well) coincide with each other. That is why in Fig. 1.11(a) we observe only two bands. Non-zero value of either λ_R or λ_v, or both lead to separation of the spin-resolved bands as shown in Fig. 1.11(b).

1.7.1 Phase diagram: $\mathbb{Z}_2$ invariant

Despite the similarity of the bands for each spin with those of the Haldane model, they displays unique behaviour. Because, the ↑- and ↓-spins have complex NNN hopping phases of $\phi = +\pi/2$ and $-\pi/2$ respectively, they possess opposite masses at the Dirac points. It results in a spin-dependent Chern number (C_μ), with $C_\uparrow = +1$ and $C_\downarrow = -1$. The total Chern number, $\sum_{\mu=\uparrow,\downarrow} C_\mu = 0$, is preserved due to time-reversal symmetry. However, the difference between the Chern numbers is

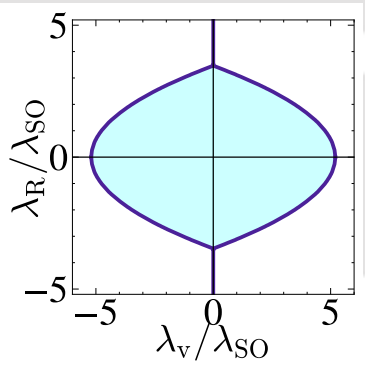

FIG. 1.12: The phase diagram of the Kane-Mele model is presented, where the colored region denotes the spin Hall phase with $\mathbb{Z}_2 = 1$. The white region represents the trivial phase with $\mathbb{Z}_2 = 0$.

non-zero. This indicates that the system can be defined with another topological invariant, and is known as the $\mathbb{Z}_2$ invariant. This type of insulators are categorized as a $\mathbb{Z}_2$ topological insulator. The difference between the Chern numbers for spin-↑ and spin-↓ electrons is given by $C^s = C_\uparrow - C_\downarrow = 2$. The $\mathbb{Z}_2$ invariant can be calculated using $C^s/2$ mod 2, which is equal to 1 [146, 147]. Now, we turn on the staggered sublattice potential λ_v and the Rashba SOC λ_R. Now the previous method can not be used to compute the $\mathbb{Z}_2$ invariant because the Rashba term

mixes the spin degrees of freedom with the sublattice degrees of freedom and hence $C_\uparrow(C_\downarrow)$ can not be computed separately. We use the method described in Sec. 1.1.4 to compute the $\mathbb{Z}_2$ invariant for various values of λ_{R} and λ_{v} and plotted it in Fig. 1.12. The region enclosed by the curve (the blue region) has a $\mathbb{Z}_2$ invariant of 1, while it vanishes outside. Therefore, the system shows non-trivial spin Hall insulating phase ($\mathbb{Z}_2 = 1$) inside the curve, while it is a trivial insulator ($\mathbb{Z}_2 = 0$) in the outside region.

1.7.2 Cyclotron effective mass for Kane-Mele model

To compute the Cyclotron effective mass, it is necessary to establish an equation for the electronic energy about the Dirac points. This equation can be derived through the diagonalization of the Hamiltonian presented in Eq. 1.70. However, diagonalizing a 4×4 Hamiltonian is a challenging task, making it difficult to obtain the desired energy expression. Alternatively, when λ_{R} is set to zero, we can derive an analytical expression with an identical form to that of the Haldane model. Consequently, the Cyclotron effective mass m^* remains the same as that in the Haldane model, exhibiting a linear variation with respect to E.

1.8 Semi-Dirac system

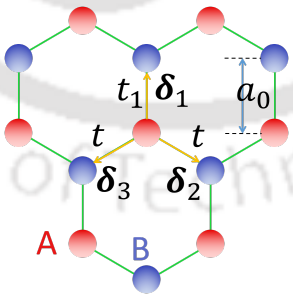

FIG. 1.13: A honeycomb lattice with the nearest neighbour hopping is presented. The NN hopping t_1 is along the $\boldsymbol{\delta}_1$ direction, while it is t along the $\boldsymbol{\delta}_2$ and $\boldsymbol{\delta}_3$ directions.

In a previous observation, it was noted that the dispersion spectrum of graphene displays isotropy around the band touching points, resulting in a linear spectrum in all directions. Some systems exist that display anisotropic dispersions, which

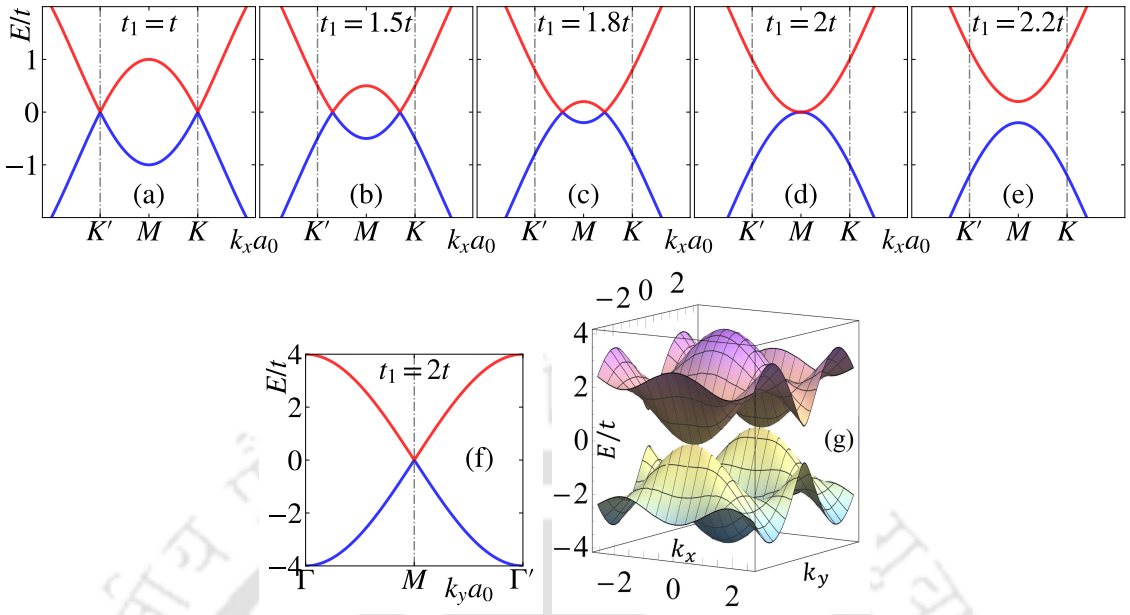

FIG. 1.14: The band structure along the k_x axis is shown for (a) $t_1 = t$, (b) $t_1 = 1.5t$, (c) $t_1 = 1.8t$, (d) $t_1 = 2t$, and (e) $t_1 = 2.2t$. The spectrum along the k_y axis is shown in (f) specifically for $t_1 = 2t$. A 3D depiction of the dispersion spectrum for $t_1 = 2t$ is presented in (g).

show interesting properties. The anisotropic dispersion in the honeycomb lattice can also be achieved if the NN hopping along a specific direction (say, $\boldsymbol{\delta}_1$ direction) is adjusted to twice that for rest of the NN hoppings. This results in movement of Dirac cones and their merger into one at an intermediate $\mathrm{M}\left(0, \frac{2\pi}{3a}\right)$ point. The dispersion exhibits linearity in one direction and quadratic behaviour along the other, which is called the semi-Dirac dispersion. It causes electrons to behave as both massive fermions and massless Dirac particles simultaneously in orthogonal directions. The tight-binding Hamiltonian of the system can be written as,

$$H = \sum_{\langle ij \rangle} (t_{ij} c_i^\dagger c_j + \text{h.c.}) \tag{1.71}$$

where t_{ij} is the anisotropic nearest neighbour hopping. $t_{ij} = t_1$ when the sites i and j lie along the $\boldsymbol{\delta}_1$ direction, while $t_{ij} = t$ when they lie along the $\boldsymbol{\delta}_{2,3}$ directions as depicted in Fig. 1.13. Similar to the case of graphene, we Fourier transform the operators and the k-space Hamiltonian becomes $H(\mathbf{k}) = h_x(\mathbf{k})\sigma_x + h_y(\mathbf{k})\sigma_y =$

$\mathbf{h}(\mathbf{k}) \cdot \boldsymbol{\sigma}$. The expressions for h_is are

$$h_x(\mathbf{k}) = \left\{ t_1 \cos k_y + 2t \cos \frac{k_y}{2} \cos \frac{\sqrt{3}k_x}{2} \right\}, \tag{1.72}$$

and

$$h_y(\mathbf{k}) = \left\{ -t_1 \sin k_y + 2t \sin \frac{k_y}{2} \cos \frac{\sqrt{3}k_x}{2} \right\} \tag{1.73}$$

The dispersion relation is written as

$$E_{\mathbf{k}} = \pm \sqrt{2t^2 + t_1^2 + 2t^2 \cos \sqrt{3}k_x a + 4tt_1 \cos(3k_y a/2) \cos(\sqrt{3}k_x a/2)} \tag{1.74}$$

Now we show the band structure for various values of t_1 in Fig. 1.14. It can be noticed that for the isotropic case, that is, for $t_1 = t$ we observe the band structure of graphene. As the value of t_1 is increased, the Dirac cones at the $\mathbf{K}$ and $\mathbf{K}'$ points migrate towards each other (see Figs. 1.14(b) and 1.14(c)). They finally merge at the $\mathbf{M}$ point for a particular value of t_1, namely, $t_1 = 2t$, where the dispersion is quadratic along the k_x-direction (Fig. 1.14(d)) and linear along the k_y-direction (Fig. 1.14(f)). For the values of t_1 beyond $2t$, a gap opens up at the $\mathbf{M}$ point as shown in Fig. 1.14(e). In this transition process, the bandwidth of the system also increases and is equal to $2(t_1 + 2t)$. A three-dimensional depiction of the spectrum corresponding to $t_1 = 2t$ is presented in Fig. 1.14(g).

The low energy Hamiltonian of the semi-Dirac systems ($t_1 = 2t$) about the $\mathbf{M}$ point is given by,

$$H_{\mathbf{M}} = \alpha_x k_x^2 \sigma_x + v_y k_y \sigma_y \tag{1.75}$$

where $\alpha_x = \frac{3ta_0^2}{4}$ and $v_y = 3ta_0$. $\mathbf{q}$ is the small momenta about the $\mathbf{M}$ point, that is, $\mathbf{q} = \mathbf{k} - \mathbf{M}$. The corresponding eigensolutions have the following form,

$$E(\mathbf{q}) = \pm \sqrt{\left(\alpha_x q_x^2\right)^2 + (v_y q_y)^2}; \quad \Psi_{\pm}(\mathbf{q}) = \frac{1}{\sqrt{2}} \begin{pmatrix} 1 \\ \pm e^{i\theta_q} \end{pmatrix} \tag{1.76}$$

where $\theta_q = \tan^{-1} \frac{v_y k_y}{\alpha_x k_x^2}$. The dispersion relation clearly verifies the anisotropic

nature of the band structure. Further, we use the above eigensolutions and Eq. 1.7 to obtain the expression for Berry connection, which is given by,

$$\mathcal{A} = -\frac{v_y^2}{2}\frac{1}{E_\pm}\left(-2q_x q_y\,\hat{x} + q_x^2\,\hat{y}\right) \tag{1.77}$$

Now Berry phase can be calculated using Eq. 1.6 which yields $\Phi_B = 0$. The Berry curvature is also found to be zero which can be predicted from Eq. 1.15, since $h_z = 0$.

1.8.1 Cyclotron effective mass

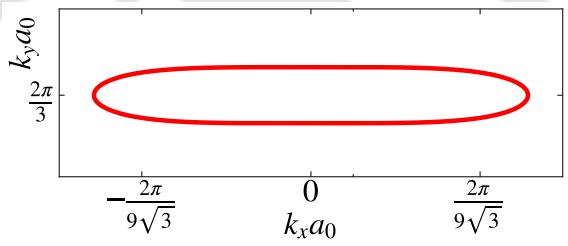

FIG. 1.15: An isoenergy contour of the semi-Dirac dispersion around the M point is depicted.

To calculate the cyclotron effective mass, we use Eq. 1.54. Before that we need to calculate the area $S(E)$ of the isoenergy contours. However, the trajectory of the electrons are not circular, since it is quadratic in k_x and linear in k_y as shown in Fig. 1.15. Therefore, we calculate the area of the first quadrant by integration and the total area would be four times of it which is given by,

$$S(E) = \int q_y\,\mathrm{d}q_x = 4\int_{q_x=0}^{\sqrt{E/\alpha}} \frac{1}{v_y}\sqrt{E^2 - \alpha_x^2 q_x^4}\,\mathrm{d}q_x$$

$$= \frac{E^{3/2}}{v_y\sqrt{\alpha_x}}\int_{\xi=0}^{1}(1-\xi)^{1/2}\,\xi^{-3/4}\,\mathrm{d}\xi$$

where $\xi = \frac{\alpha_x^2}{E^2}q_x^4$. This yields,

$$S(E) = \frac{2\sqrt{\pi}}{3}\frac{\Gamma(\frac{1}{4})}{\Gamma(\frac{3}{4})}\frac{E^{3/2}}{v_y\sqrt{\alpha}} \tag{1.78}$$

Hence the cyclotron mass becomes proportional to $\sqrt{E}$, namely,

$$m^* = \frac{\hbar^2 E^{1/2}}{\sqrt{\alpha_x} v_y} \frac{\Gamma(\frac{1}{4})}{2\sqrt{\pi}\Gamma(\frac{3}{4})}. \tag{1.79}$$

This result is completely different from graphene (the Dirac case) as evident from the band structure which is anisotropic in this type of semi-Dirac system.

Chapter 2

Band-Engineered Haldane Model

In order to answer a question whether a crystal lattice with Bloch bands can possess a non-zero Chern number in the absence of an external magnetic field, Haldane in a seminal paper [16] had proposed a complex next nearest neighbour hopping in a honeycomb lattice which explicitly breaks the time reversal symmetry (albeit no net flux) and should yields a quantized anomalous Hall conductance, σ_{xy}. The quantization of σ_{xy} is an artefact of the quantized (integral) values of the Chern number which is obtained from the integral of the Berry curvature over the BZ. A non-vanishing Chern number and hence a finite Hall response are expected for any arbitrary value of the phase, ϕ of the complex next nearest neighbour hopping, where the closing (opening) of the energy gap occurs at either of the Dirac points ($\mathbf{K}$ and $\mathbf{K}'$) depending on the value of the Semenoff mass, Δ. A rescaled variant of it, namely, $\tilde{\Delta}$ ($= \Delta/3\sqrt{3}\sin\phi$) as a function of ϕ shows a phase diagram that encodes opening and closing of the spectral gaps alternately at the $\mathbf{K}$ and the $\mathbf{K}'$ points as $\tilde{\Delta}$ is tuned between $+1$ and -1.

A striking distinction of the linear dispersion (Dirac like) along both the longitudinal directions in k-space, is a case presented by an anisotropic dispersion where the bands are found to be linearly disperse along one direction and quadratically in the other [40, 41]. Such a dispersion is referred to as the semi-Dirac dispersion and has been realized in a variety of experimental scenarios. We have already presented an account of such experiments and the relevant theoretical work in the previous chapter (see the introduction of Chapter 1).

However, the fate of the anisotropic Dirac physics has never been discussed in conjunction with a topologically non-trivial energy gap in the spectrum. This motivates us to explore the evolution of the topological properties of an anisotropic dispersion in the presence of a Haldane flux as one interpolates between the Dirac and the semi-Dirac cases and it comprises of the content in this chapter. As detailed earlier, such a possibility can be realized by choosing the hopping amplitude corresponding to one of the neighbours (say t_1) to be different than the other two (say t), where the former can be tuned starting from a value equal to the latter, that is, $t_1 = t$ to larger values, for example, $t_1 \geq 2t$. We shall show below that in the regime $t < t_1 < 2t$, we get a non-trivial insulating phase with a plateau at a value of e^2/h for the (anomalous) Hall conductivity whose width shrinks as a function of $\delta(= t_1/t)$ since it denotes the energy gap in the spectrum. At the semi-Dirac limit ($t_1 = 2t$), upto second order in momenta, the dispersion displays a linear behaviour in one direction and quadratic in the other. The M point is located at $(0, \frac{2\pi}{3a_0})$, a_0 being the lattice constant. Under this condition, the physics becomes similar to that of a single anisotropic Dirac cone in the low energy limit, although the inversion symmetry is still preserved. This, along with a Berry phase of π yields a finite Berry curvature at certain k-points in the BZ, despite not having any gap in the spectrum. The Chern number vanishes as soon as t_1 becomes greater than $2t$ where a trivial insulating phase emerges, thereby indicating a transition from a topological phase to a trivial one through a gap closing point. Appearance of two counter propagating modes at the edges is responsible for the emergence of a trivial insulating phase beyond the gap closing point.

To summarize, in this chapter, we present a detailed study of the evolution of the band structure, density of states (DOS), edge modes in a nanoribbon, Berry curvature, Chern number phase diagram and finally the anomalous Hall conductivity to study the evolution of the topological properties. Importantly, we address the existence of a phase transition from a topological to a trivial phase embedded therein.

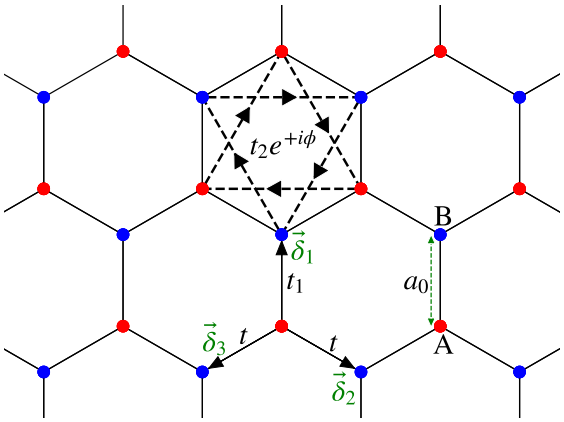

FIG. 2.1: (Color online) A honeycomb lattice is shown where the red and the blue circles represent two different sublattices A and B respectively. In the $\boldsymbol{\delta}_2$ and $\boldsymbol{\delta}_3$ direction, the nearest neighbour hopping strengths are same, namely, t, whereas in the $\boldsymbol{\delta}_1$ direction, it is t_1. At the top, the sign of the complex phase, ϕ corresponding to NNN hopping is depicted. The arrows indicate the direction of the electrons hopping between the sites of the same sublattice (A to A or B to B). For the hopping to be in the clockwise direction, ϕ is positive and for the hopping in the anti-clockwise direction ϕ is negative.

2.1 Model Hamiltonian

The tight-binding Hamiltonian for Haldane model can be written as,

$$H = \sum_{\langle i,j\rangle} t_{ij} c_i^\dagger c_j + t_2 \sum_{\langle\langle i,j\rangle\rangle} e^{i\phi_{ij}} c_i^\dagger c_j + \sum_i \Delta_i c_i^\dagger c_i + \text{h.c.}, \tag{2.1}$$

Various symbols have already been used in Chapter 1. We still include here for completeness. The first term denotes the nearest-neighbour hopping with the strength t_{ij}. $t_{ij} = t$ in the two nearest neighbours directions ($\boldsymbol{\delta}_2$ and $\boldsymbol{\delta}_3$), whereas in the third direction, that is, along $\boldsymbol{\delta}_1$, the strength is t_1. The NN vectors are given by, $\boldsymbol{\delta}_1 = a_0(0,1)$, $\boldsymbol{\delta}_2 = a_0(\sqrt{3}/2, -1/2)$ and $\boldsymbol{\delta}_3 = a_0(-\sqrt{3}/2, -1/2)$. The second term denotes the direction dependent next nearest neighbour (NNN) hopping with an amplitude t_2 and a complex phase ϕ having identical values along all the NNN directions, where ϕ assumes positive (negative) values if the electron hops in the clockwise (anti-clockwise) direction. The three NNN vectors are denoted by $\boldsymbol{\nu}_1 = \boldsymbol{\delta}_2 - \boldsymbol{\delta}_3$, $\boldsymbol{\nu}_2 = \boldsymbol{\delta}_3 - \boldsymbol{\delta}_1$ and $\boldsymbol{\nu}_3 = \boldsymbol{\delta}_2 - \boldsymbol{\delta}_1$. The third term in Eq. (2.1) denotes the on-site energy term, where Δ_i is $+\Delta$ ($-\Delta$) depending on the A (B) sublattice

sites. A Fourier transform of the Hamiltonian in Eq. (2.1) yields,

$$\begin{aligned} H &= \left[t_1 \cos(\mathbf{k}\cdot\boldsymbol{\delta}_1) + \sum_{i=2}^{3} t\ \cos(\mathbf{k}\cdot\boldsymbol{\delta}_i) \right] \sigma_x + \left[t_1 \sin(\mathbf{k}\cdot\boldsymbol{\delta}_1) + \sum_{i=2}^{3} t\ \sin(\mathbf{k}\cdot\boldsymbol{\delta}_i) \right] \sigma_y \\ &+ \left[\Delta - 2\, t_2\ \sin\,\phi \sum_{i=1}^{3} \sin(\mathbf{k}\cdot\boldsymbol{\nu}_i) \right] \sigma_z + \left[2t_2\ \cos\,\phi \sum_{i=1}^{3} \cos(\mathbf{k}\cdot\boldsymbol{\nu}_i) \right] I \\ &= h_x\sigma_x + h_y\sigma_y + h_z\sigma_z + h_0 I, \end{aligned} \tag{2.2}$$

where σ_i are the 2×2 spin-$1/2$ Pauli matrices which denote the sublattice degrees of freedom and I is the 2×2 identity matrix. h_i as shown in square brackets in Eq. (2.2) are the coefficients of σ_i. The energy dispersion can be obtained as, $E(k) = h_0 \pm [h_x^2 + h_y^2 + h_z^2]^{1/2}$, where the $\pm$ signs correspond to the conduction and the valence band dispersions respectively. To make the notations on different

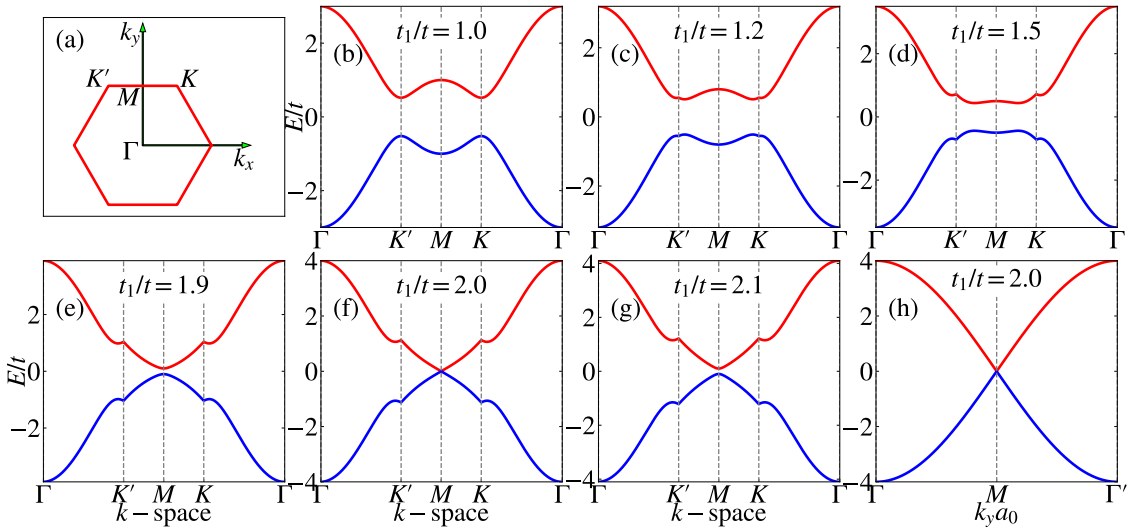

FIG. 2.2: In (a), the BZ of a honeycomb lattice is shown. The electronic band dispersions in the k-space along the $\Gamma \to K \to M \to K' \to \Gamma$ direction are depicted for (b) $t_1 = t$, (c) $t_1 = 1.2t$, (d) $t_1 = 1.5t$, (e) $t_1 = 1.9t$, (f) $t_1 = 2t$ and (g) $t_1 = 2.1t$ are shown. In (h), the dispersion along the $\Gamma \to M \to \Gamma'$ direction is shown specifically for $t_1 = 2t$. In all figures, t_2, Δ, and ϕ are kept fixed at $0.1t$, 0 and $\pi/2$ respectively.

symmetry points clear, the BZ of the honeycomb lattice and the electronic band structures corresponding to different values of t_1 are shown in Fig. 2.2. The NNN hopping amplitude and the complex phase are fixed at $t_2 = 0.1t$ and $\phi = \pi/2$ respectively. Inclusion of this complex NNN hopping opens up a gap, thereby

making it an insulating state. It may be noted that even with $\Delta = 0$ and $t_2 = 0$, gaps still open up at the $\mathbf{K}$ and $\mathbf{K}'$ points, however they are trivial gaps and hence do not contribute to the topological properties of the system. For $t_1 = t$, $t_2 \neq 0$ and $\phi = \pi/2$, the system is the famous Haldane model [16], where a gap opens at the two non-equivalent Dirac points, that is, at the $\mathbf{K}'$ $(2\pi/3\sqrt{3}a_0, 2\pi/3a_0)$ and at the $\mathbf{K}$ $(-2\pi/3\sqrt{3}a_0, 2\pi/3a_0)$ points (see Fig. 2.2(b)). As t_1 deviates from t, these points come closer to each other, accompanied by a diminishing band gap occurring in the spectrum (see Figs. 2.2(c)-2.2(e)). As t_1 becomes equal to $2t$, that is the semi-Dirac limit, even in the presence of t_2, the two bands touch at the $\mathbf{M}$ $(0, 2\pi/3a_0)$ point (see Fig. 2.2(f)). This is obvious from the expression of h_z, which is zero only at the $\mathbf{M}$ point, becomes non-zero as one moves away from the $\mathbf{M}$ point and eventually at the $\mathbf{K}$ or the $\mathbf{K}'$ points it reaches its maximum value, namely, $|3\sqrt{3}t_2|$. Moreover, the band structure along the k_y-direction for $t_1 = 2t$ is depicted in Fig. 2.2(h). Upon closer inspection, it can be seen that the dispersion is linear along both the k_x- and k_y-directions (see Figs. 2.2(f) and 2.2(h)) at the low energies, however the velocities of the electrons are unequal. Such dispersions are known as the anisotropic linear dispersion which is different from the Dirac case ($t_1 = t$) where the spectrum is isotropically linear. Later we shall demonstrate how the band dispersion affects the Berry phase. Furthermore, when t_1 exceeds the semi-Dirac value ($= 2t$), namely, $t_1 = 2.1t$, a spectral gap reopens. This occurs owing to h_x and h_y now becoming non-zero at the $\mathbf{M}$ point as evident from Fig. 2.2(g). Moreover, the bandwidth increases from $6t$ in the Dirac case to $2(2t + t_1)$ for the semi-Dirac one.

Further, to support the anisotropic linear behaviour for the $t_1 = 2t$ case, we obtain the expressions for cyclotron effective mass only for the $t_1 = 2t$ case in presence of a non-zero t_2 using Eq. 1.54.

$$m^* = \frac{\hbar^2 E}{v_x v_y} \tag{2.3}$$

To calculate it, the area of isoenergy contours is used, which is $S(E) = \pi E^2/(v_x v_y)$. Here, $E = [v_x^2 q_x^2 + v_y^2 q_y^2]$ is the energy of the system obtained from the low energy Hamiltonian in Eq. 2.10 (only the terms linear in q_x and q_y are kept) with

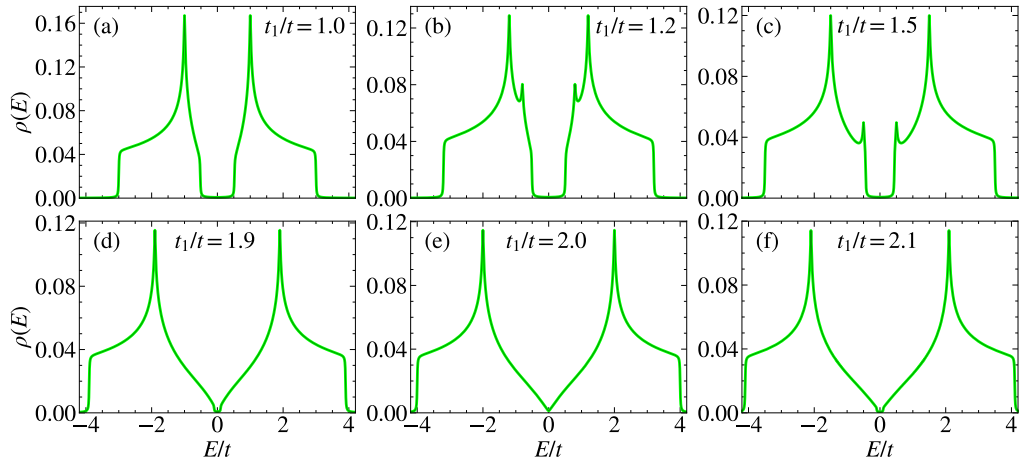

FIG. 2.3: The density of states (DOS) (in units of $1/t$) is plotted as a function of E/t for (a) $t_1 = t$, (b) $t_1 = 1.2t$, (c) $t_1 = 1.5t$, (d) $t_1 = 1.9t$, (e) $t_1 = 2t$ and (f) $t_1 = 2.1t$. Through out the calculations t_2, Δ and ϕ are kept fixed at $0.1t$, 0 and $\pi/2$ respectively.

$v_x = -4\sqrt{3}t_2a_0$ and $v_y = 3ta_0$. Thus we recover the cyclotron mass being linearly dependent on energy similar to the Dirac case (see Eq. 1.55). This confirms an anisotropic Dirac behaviour in presence of the Haldane flux and is a distinct feature compared to the absence of the Haldane flux.

Next we compute the density of states (DOS) that counts the number of electronic states in the vicinity of a particular value of energy E. It can be obtained from the following relation,

$$\rho(E) = \frac{1}{(2\pi)^2}\int_{BZ}\delta(E - E(\mathbf{k}))\mathrm{d}\mathbf{k}. \tag{2.4}$$

To show the detailed evolution, we have numerically computed the DOS for several different values of t_1 as shown in Fig. 2.3. Two extra peaks (other than the dominant ones whose origin is well understood) in the DOS spectrum appear for $t_1 = 1.2t$ and $t_1 = 1.5t$ (see Fig. 2.3(b) and 2.3(c)) because of the presence of saddle points in the band structure (see Fig. 2.2(c) and 2.2(d)) occurring at the M $(0, 2\pi/3a_0)$ point in the BZ. The saddle points are absent for further large values of t_1, namely, $t_1 \geq 1.9t$ which results in the vanishing of the additional peaks in the DOS. These peaks would occur even in absence of Haldane flux [63]. For $t < t_1 < 2t$, the DOS becomes non-vanishing in the vicinity of the zero energy

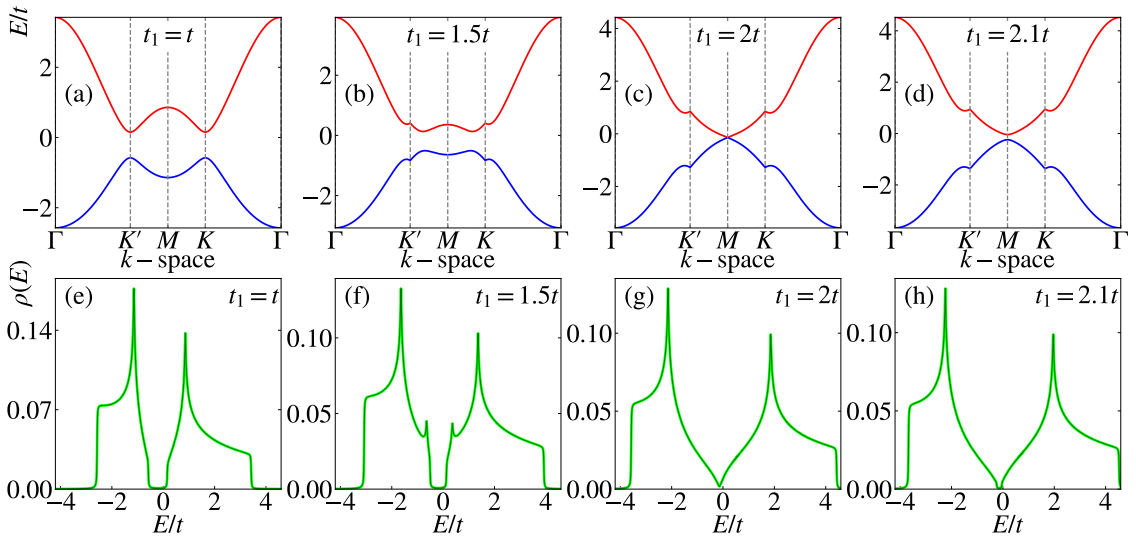

FIG. 2.4: The band structures are shown for $t_1 = t, 1.5t, 2t$, and $2.1t$ in (a), (b), (c), and (d) respectively. While, the density of states are shown for $t_1 = t, 1.5t, 2t$, and $2.1t$ in (e), (f), (g), and (h) respectively. These plots are obtained under the condition where the particle-hole symmetry is broken in the system ($\phi = \pi/4$).

which is also evident from the band structure shown in Fig. 2.2. As soon as t_1 becomes equal to $2t$, the DOS vanishes quadratically near $E = 0$ energy is denoted in unit of the hopping t (Fig. 2.3(e)). Beyond that (at $t_1 = 2.1t$), the DOS again becomes zero at $E \simeq 0$ and thus implies of a gap opening up in the spectrum.

Now, we show the dispersion spectrum and DOS for another value of ϕ, namely, $\phi = \pi/4$ in Fig. 2.4. At this value of ϕ, the NNN becomes complex and breaks the particle-hole symmetry. However, the main discussion of this chapter is relevant for $\phi = \pi/2$. From the band structures (see Figs. 2.4(a)-2.4(d)), it is evident that the conduction and valence bands are not symmetric about the Fermi level $(E_F = 0)$. However, the variations of band gap with the anisotropic hopping t_1 for $\phi = \pi/4$ remain the same as those corresponding to $\phi = \pi/2$. Further, the DOS (see Figs. 2.4(e)-2.4(h)) shows the asymmetry about $E = 0$, which is evident from the corresponding band structure plots. We also see the existence of peaks in DOS similar to the case for $\phi = \pi/2$.

2.2 Edge States

So far we have studied infinite systems which is periodic in both the x and the y-directions. However to achieve edge states and their properties, a system of finite size suits the best. It is therefore interesting to consider a semi-infinite ribbon with a finite number of sites in the y-direction and an infinite number of sites in the x direction. We label the sublattices as A_1, B_1, A_2, B_2, ... A_N, B_N etc. along the y-direction. The periodicity and hence the translational symmetry of the ribbon in the y-direction are broken because of the edges being present, while along the x-direction the system is periodic. This allows us to Fourier transform the operators only in the x-direction, via $c^{\dagger}_{x,y} = \sum_k e^{ikx} c^{\dagger}_{k,y}$. Incorporating such transformation in the tight binding Hamiltonian (Eq. (2.1)), we arrive at the following set eigenvalue equations,

$$\begin{aligned} E_k a_{k,n} = &- \left[t\left\{1 + e^{(-1)^n ik}\right\} b_{k,n} + t_1 b_{k,n-1}\right] \\ &- 2t_2 \left[\cos(k+\phi) a_{k,n} + e^{(-1)^n \frac{ik}{2}} \cos\left(\frac{k}{2} - \phi\right) \{a_{k,n-1} + a_{k,n+1}\}\right] \end{aligned} \tag{2.5}$$

$$\begin{aligned} E_k b_{k,n} = &- \left[t\left\{1 + e^{(-1)^{n+1} ik}\right\} a_{k,n} + t_1 a_{k,n+1}\right] \\ &- 2t_2 \left[\cos(k-\phi) b_{k,n} + e^{(-1)^{n+1} \frac{ik}{2}} \cos\left(\frac{k}{2} + \phi\right) \{a_{k,n-1} + a_{k,n+1}\}\right] \end{aligned} \tag{2.6}$$

where n stands for the n-th sublattice which is an integer in the range $[1 : N]$. N is related to the width of the ribbon (see below) and k is the (dimensionless) momentum in the x-direction defined by $k = \sqrt{3} a_0 k_x$. The width of the ribbon can be calculated from the relation $W(N) = a_0\left(\frac{3N}{2} - 1\right)$. In our work, we have used $N = 128$ and hence the ribbon has a width of $191 a_0$ in the y-direction. In Eqs. (2.5) and (2.6), $a_{k,n}$ and $b_{k,n}$ are the coefficients of the wavefunctions corresponding to the sublattices A and B respectively. By solving these equations, we have obtained the band structure of the ribbon for different values of t_1 in the range $[t : 2t]$ and also for $t_1 > 2t$ as shown in Fig. 2.5 for a given value of N. As can be seen, one of the modes from the lower band crosses over to the upper band with increasing values of k_x and another one crosses in the opposite direction. The amplitudes of the wavefunctions corresponding to these modes decay exponentially into the

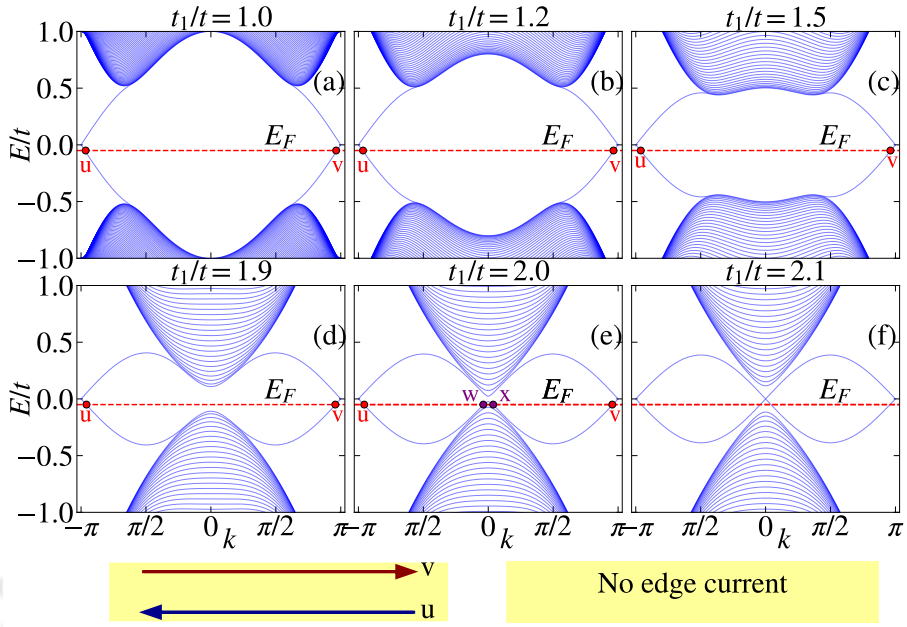

FIG. 2.5: The energy spectra as a function k (here k denotes $\sqrt{3}a_0k_x$) are shown for (a) $t_1 = t$, (b) $t_1 = 1.2t$, (c) $t_1 = 1.5t$, (d) $t_1 = 1.9t$, (e) $t_1 = 2t$ and (f) $t_1 = 2.1t$. In each figure, the edge state are shown by red dots at the Fermi energy E_F (red dashed line), while in (e) the purple dots are the bulk states. A schematic diagram of a part of the ribbon with edge current are shown in yellow panels, where the edge currents along the edges are depicted by arrows. For $t_1 = 2.1t$, the edge modes are detached from the bulk. This results in no edge current as shown in the yellow panel a the bottom of (f). Through out the calculations N, t_2, Δ and ϕ are kept fixed at 128, $0.1t$, 0 and $\pi/2$ respectively.

bulk from a maximum value at the edge of the ribbon [184–186]. It should be noted that the velocities have opposite signs (since v is proportional to $\partial E/\partial k$) along these states, implying that the electrons move in opposite directions along the edges. This makes the edge states chiral in nature. Owing to the presence of the edge states there will be a plateau in the Hall response of value e^2/h. The edge states are shown for various values of t_1 in Fig. 2.5.

In Fig. 2.5(e), we have shown the band structure for $t_1 = 2t$, where the intersection of the edge states with the Fermi energy, E_F (shown via a dashed line at $E/t = 0$) are represented by the dots u and v, whereas the purple dots w and x belong to the bulk states. Below the figure, the edge currents corresponding to the points u and v along the edges of the ribbon are depicted in a yellow panel. Although there is a small gap discernible at $k = 0$ for $t_1 = 2t$, if we gradually increase the value of N, or equivalently, the width of the ribbon, we shall observe

vanishing of the gap. Consequently in an infinite system there will be no gap in the band structure as inferred from Fig. 2.2(f). The edge states for $t_1 = 2.1t$ is depicted in Fig. 2.5(f), where the edge modes are detached from the bulk bands. As a result, there is no edge current in the ribbon, as shown in the yellow panel at the bottom of Fig. 2.5(f).

2.3 Berry phase and Berry curvature

In this section, we present the Berry curvature and Berry phase of the system. First, we compute the Berry curvature, Ω numerically using Eq. 1.15 for various values of t_1 and the results are shown in Fig. 2.6. The $t_1 = t$ case (Fig. 2.6(a)) represents a familiar scenario where the non-zero (and negative) values are highly concentrated around the Dirac points which persists as t_1 starts deviating from t till moderate values of t_1. At larger values of t_1 (close to yet less than $2t$) the Berry curvature (Fig. 2.6(b)-2.6(f)) becomes non-zero only in the vicinity of the M point. For $t_1 = 2t$, Ω diverges since the two bands touch each other at the M point. When $t_1 > 2t$, Ω reverses its sign as shown in Fig. 2.6(f). The implication of the sign change in Ω for $t_1 > 2t$ becomes clear, as we examine the Chern number, which drops from a value $1 \rightarrow 0$, as we shall see in Sec. 2.4.

Further, to visualize the divergence nature of Ω corresponding to the $t_1 = 2t$ case, we evaluate the expression for Ω using Eq. 1.15 which is given as,

$$\Omega_{\pm}(q_x, q_y) = \mp \frac{v_x v_y \alpha_x q_x^2}{2\left[\alpha_x^2 q_x^4 + v_y^2 q_y^2 + v_x^2 q_x^2\right]^{\frac{3}{2}}} \tag{2.7}$$

where $\alpha_x = \frac{3ta_0^2}{4}$, $v_y = 3ta_0$, and $v_x = -4\sqrt{3}t_2 a_0$. $\mathbf{q}$ is the small momenta about the M point, that is, $\mathbf{q} = \mathbf{k} - \mathbf{M}$. The low energy Hamiltonian discussed in Sec. 2.5 has been used for the calculation of above Ω. The expressions for d_x, d_y and d_z are $\alpha_x q_x^2$, $v_y q_y$ and $v_x q_x$ respectively. The other terms of d_is, shown in table 2.1 for $t_1 = 2t$ have been ignored. It can be seen that Ω diverges at the M point (put $q_x = q_y = 0$).

Now we discuss the evolution of the Berry phase, Φ_B. To calculate it, Eq. 1.6 has been used. The variation of Φ_B with respect to the NN hopping t_1 in presence

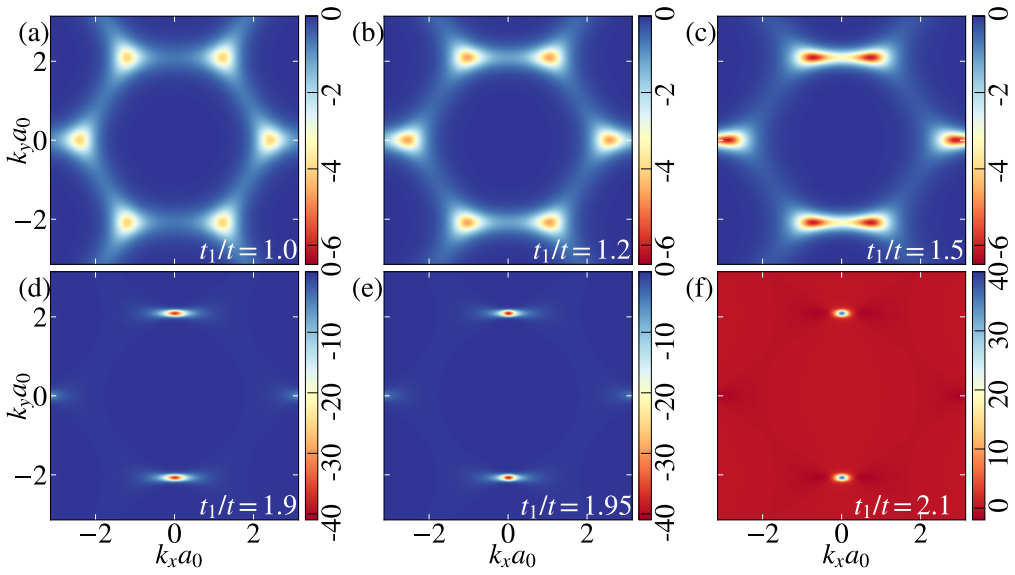

FIG. 2.6: Berry curvatures are shown in the k_x-k_y plane for (a) $t_1 = t$, (b) $t_1 = 1.2t$, (c) $t_1 = 1.5t$, (d) $t_1 = 1.9t$, (e) $t_1 = 1.95t$ and (f) $t_1 = 2.1t$. Here t_2, ϕ and Δ are fixed at $0.1t$, $\pi/2$ and 0 respectively. The colorbar denotes the magnitude of the Berry curvature.

of a NNN hopping ($t_2 = 0.1t$) is shown in Fig. 2.7 by the blue curve. As can be seen, $\Phi_B \approx 2\pi$ as long as there is a gap in the spectrum, that is, for $t_1 < 2t$. This is a key result as it implies that a non-zero Haldane flux renders a non-relativistic character to an otherwise relativistic Dirac fermion. As soon as t_1 becomes $2t$, the gap disappears and becomes anisotropic linear (about the M point, see Figs. 2.2(f) and 2.2(h)), Φ_B drops to a value very nearly equal to π. When t_1 exceeds $2t$ (say, $t_a = 2.1t$), again a gap opens up in the spectrum, however Φ_B drops to zero.

We have also shown Φ_B as a function of t_1 in absence of t_2 ($t_2 = 0$) in Fig. 2.7 by the red curve. When $t_1 = t$, that is, in the Dirac case, Φ_B is found to have a value π. It persists at a value π as long as t_1 remains less than $2t$, since the Dirac cones exist (see Figs. 1.14(a)-1.14(c) in chapter 1). When those Dirac cones merge at $t_1 = 2t$ and the dispersion becomes semi-Dirac type about the M point, Φ_B vanishes. As t_1 exceeds $2t$, Φ_B remains at zero in the gapped dispersion spectrum.

Therefore, in the gap closing scenarios, when we have linear dispersions in both k_x- and k_y-directions, whether it is isotropic or anisotropic, we always observe a Berry phase π [the cases with $(t \leq t_1 < 2t, t_2 = 0)$ and $(t_1 = 2t, t_2 = 0.1t)$]. Once the gap opens or the dispersion becomes quadratic, Φ_B either becomes 2π or

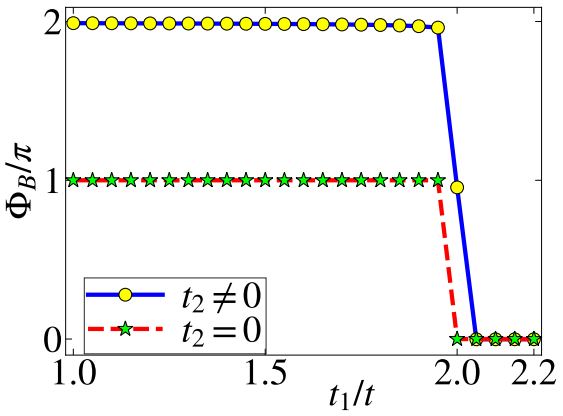

FIG. 2.7: The Berry phase is shown as a function of t_1 both in the presence ($t_2 = 0.1t$) and in the absence ($t_2 = 0$) of NNN hopping.

drops to zero.

2.4 Chern Number

To obtain a phase diagram that encodes vanishing of the quantum anomalous Hall phase, we now turn on the inversion-symmetry breaking on-site energies $+\Delta$ and $-\Delta$ at the sublattices A and B respectively [188]. Only inclusion of Δ (that is, keeping $t_2 = 0$) allows us to open an energy gap in the spectrum at the Dirac points. However, the gap is trivial in nature.

Now in order to get information about the non-trivial phase in such a scenario, we compute the Chern number. We follow the method discussed in Sec. 1.1.3 to calculate the Chern number corresponding to the lower band as a function of Δ and ϕ, keeping t_2 constant as shown in the phase diagrams of Fig. 2.8. As can be seen, there are three regions in each phase diagram. The red ($C = +1$) and the blue ($C = -1$) regions are the topologically non-trivial insulating phase, while the green region ($C = 0$) denotes a trivial insulator. When $t_1 = t$ we get the well known phase diagram of the Haldane model [187] (see Fig. 2.8(a)), where the phase transition occurs at $\Delta = |3\sqrt{3}t_2|$ for $\phi = \pi/2$. Whereas if we look at the other phase diagrams (Fig. 2.8(b) - 2.8(f)) for $t_1 > t$, the features are similar to that of the Haldane model, except for the size of Chern insulating region gradually shrinks. These results are consistent with the band structure plots (see Fig. 2.2).

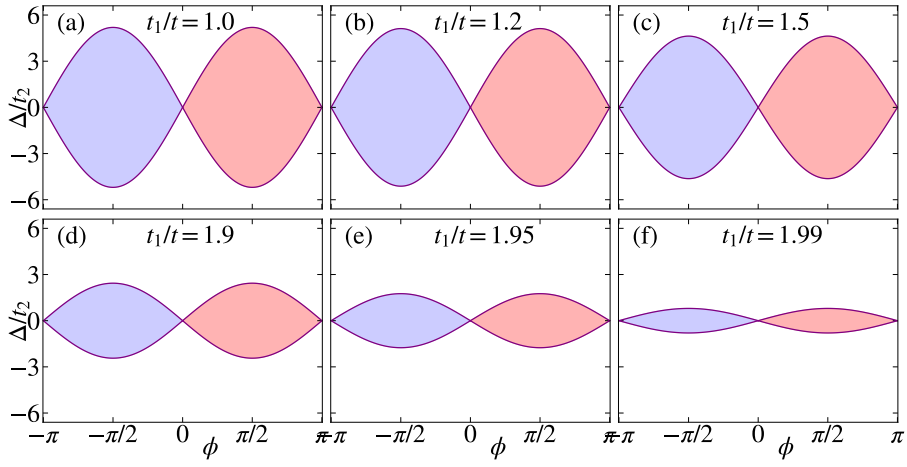

FIG. 2.8: Phase diagram for (a) $t_1 = t$, (b) $t_1 = 1.2t$, (c) $t_1 = 1.5t$, (d) $t_1 = 1.9t$, (e) $t_1 = 1.95t$ and (f) $t_1 = 1.99t$. Each of the red and the blue regions represent Chern insulating phase with Chern number $+1$ and -1 respectively, whereas the green region in each figure is the normal insulating phase with zero Chern number.

As the band gap decreases with the increasing strength of t_1, phase transitions between the topological and the trivial phases occur for lesser values of Δ. In the semi-Dirac limit, the energy spectrum consists of gapless anisotropic Dirac cones in the low energy limit. Here $t_1 = 2t$ denotes a critical point (gap closing point) which demarcates the topological phase ($t < t_1 < 2t$) from a normal insulating phase ($t_1 > 2t$). As the value of t_1 becomes larger than $2t$, that is, $t_1 = 2.1t$, the system becomes a band insulator.

The shrinking of the width of the Chern lobes in shown in Fig. 2.9. As can be

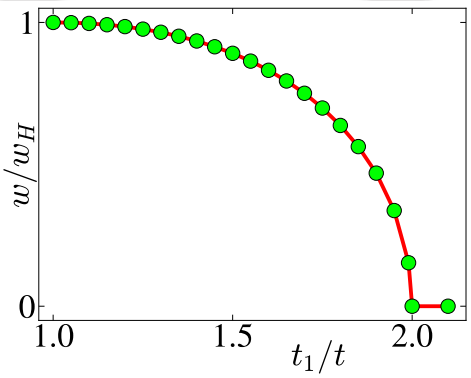

FIG. 2.9: The width of the Chern insulating phase as a function of t_1/t corresponding to $\phi = \pi/2$ is shown. Here $w_H = 6\sqrt{3}t_2$ is the width for $t_1 = t$, that is, the width of the lobe in the Haldane model.

seen from Fig. 2.8, the width is maximum at $t_1 = t$ and has a value $6\sqrt{3}t_2$ (let us denote it by w_H). There is a slower fall off initially as t_1 starts deviating from t, however there is a near vertical decrease in the width as t_1 approaches $2t$, which eventually vanishes at the critical (semi-Dirac) point, namely, $t_1 = 2t$.

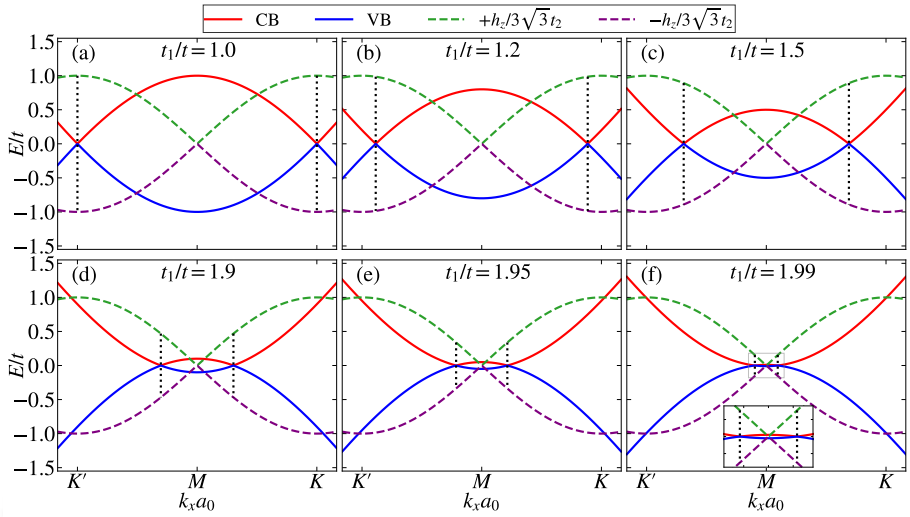

FIG. 2.10: The band dispersion in the absence of the NNN hopping $(t_2 = 0)$ along $K \to M \to K'$ direction, that is, the k_x direction for (a) $t_1 = t$, (b) $t_1 = 1.2t$, (c) $t_1 = 1.5t$, (d) $t_1 = 1.9t$, (e) $t_1 = 1.95t$ and (f) $t_1 = 1.99t$. In the inset of (f), a closer view in the vicinity of **M** point is shown. In each of the figures, the red and the blue curves represent the conduction band (CB) and the valence band (VB) respectively, while the green and the purple dashed curves are positive and negative values of h_z scaled by $3\sqrt{3}t_2$. The vertical dotted lines are plotted at k_x points where the CB and VB touch each other. Here we have set ϕ and Δ as $\pi/2$ and 0 respectively.

In order to visualize the dependence of the width w on the band structure, we have depicted the conduction and the valence bands along the k_x-axis for a particular value of k_y, namely, $k_y = 2\pi/3$ for different values of t_1 in Fig. 2.10, where the NNN hopping is absent, that is, for $t_2 = 0$. The conduction and the valence bands are shown by the red and the blue curves, while the values $\pm h_z/3\sqrt{3}t_2$ (see definition of h_z in Eq. (2.2) where the complex NNN hopping, t_2 enters through h_z with $3\sqrt{3}t_2$ being the value of h_z at the **K** and **K**′ points in the Haldane model) are shown by the green and the purple curves. The dotted vertical lines are drawn at the band touching points which depend on the NN hopping strength (t_1) and the height of these lines between the positive and the negative values of h_z is $2w/w_H$, where w is width of the Chern insulating phase for $t_1 \neq t$. So the width depends on the magnitude of h_z at the band touching point and this magnitude

decreases as one approaches the **M** point starting from the **K** and the **K**′ points. Mathematically, it can be represented as,

$$\frac{w}{w_H} = \frac{h_z(k_x, k_y)}{3\sqrt{3}t_2} \tag{2.8}$$

where k_x and k_y denote the magnitude of the momenta for which the energy gap vanishes. It should be noted that between **K** and **K**′, the band touching points for different t_1 can be evaluated by setting either h_x or h_y to zero and k_y to $2\pi/3$ which results in the following equation,

$$k_x = \pm\frac{2}{\sqrt{3}}\cos^{-1}\left(\frac{t_1}{2t}\right), \quad 1 \leq t_1 \leq 2 \tag{2.9}$$

These boundary points are shown in Fig. 2.10.

2.5 Anomalous Hall conductivity

In this section we present numerical calculations of the Hall conductivity for our band deformed system. A non-zero local Berry curvature gives rise to the anomalous Hall conductivity. In order to calculate it we first obtain the low energy form for the tight binding Hamiltonian in Eq. (2.1) for different choices of t_1. Such a low energy expansion (that is, the Taylor series expansion around the band minima points) of the Hamiltonian will be valid and helpful for our purpose. It can be written in a compact notation as,

$$H = d_x(t_1/t, k_x, k_y)t\sigma_x + d_y(t_1/t, k_x, k_y)t\sigma_y + d_z(t_1/t, k_x, k_y)t_2\sigma_z \tag{2.10}$$

where the coefficients d_x, d_y and d_z are functions of k_x, k_y and t_1/t. These coefficients are presented up to terms quadratic in k_x and k_y corresponding to a few values of t_1/t in table 2.1. For simplicity we have absorbed the lattice constant in the definition of the momentum, **k** so that it is rendered dimensionless. It is to be kept in mind that the low energy expansions are done at different k_x, k_y points for different values of t_1 since the bands come closest at different points in the

TABLE. 2.1: The coefficients d_x, d_y and d_z for a few different values of t_1/t are shown in the table. The coefficients are presented up to terms quadratic in k_x and k_y. Here we have set ϕ and Δ as $\pi/2$ and 0 respectively.

t_1/t	d_x	d_y	d_z
1	$\frac{3}{2}k_x - \frac{3}{8}k_x^2 + \frac{1}{4}k_y^2$	$\frac{3}{2}k_y - \frac{3}{8}k_yk_x$	$-3\sqrt{3}$
1.9	$\frac{3}{4}k_x^2 - \frac{7}{10}k_y^2 + \frac{29}{20}\sqrt{3}k_y - \frac{1}{20}$	$\frac{9\sqrt{3}}{40}k_y^2 + \frac{29}{20}k_y + \frac{3\sqrt{3}}{4}k_x^2 + \frac{\sqrt{3}}{20}$	$-4\sqrt{3}k_x$
2	$\frac{3}{4}k_x^2 - \frac{3}{4}k_y^2$	$3k_y + \frac{3\sqrt{3}}{4}k_x^2 - \frac{3}{4}k_y^2$	$-4\sqrt{3}k_x$
2.1	$\frac{3}{4}k_x^2 - \frac{8}{5}k_y^2 + \frac{31}{20}\sqrt{3}k_y + \frac{1}{20}$	$\frac{11\sqrt{3}}{40}k_y^2 + \frac{31}{20}k_y + \frac{3\sqrt{3}}{4}k_x^2 - \frac{\sqrt{3}}{20}$	$-4\sqrt{3}k_x$

BZ. As an example, for $t_1 = t$, the approximation is done around the point with coordinates $(2\pi/3\sqrt{3}, 2\pi/3)$ (the Dirac points), whereas for $t_1 \leq 2t$, the expansion is done around the point $(0, 2\pi/3)$ (the M point).

The Hamiltonian with these coefficients in table 2.1 represents the generic Hamiltonian for a two-level system and is of the form, $H = \mathbf{d} \cdot \boldsymbol{\sigma}$, where the components of $\mathbf{d}$-vector are the coefficients of σ_is in Eq. (2.10). One may distinguish the d_is from the h_is in Eq. (2.2) where the latter, namely, h_x, h_y and h_z denote the coefficients corresponding to the full tight binding Hamiltonian. For $t_1 = t$, the coefficients of σ_x and σ_y, namely, d_x and d_y depend on terms that are linear in k_x and k_y respectively.

For larger t_1, particularly for $t_1 = 2t$, d_x is quadratic in both k_x and k_y, while d_y has terms linear in k_y and quadratic in both k_x and k_y. This renders non-uniformity in the band dispersion, and thus results in unequal velocities in different directions in the k-space. Further, the coefficient of σ_z, which arises because of the Haldane term (complex NNN hopping) is a constant for $t_1 = t$, while for larger values of t_1, it varies linearly in k_x. However for small k values (near the M point), the linear terms are dominant which gives anisotropic linear band dispersion at low energies.

The simple form of the Hamiltonian facilitates computation of the anomalous

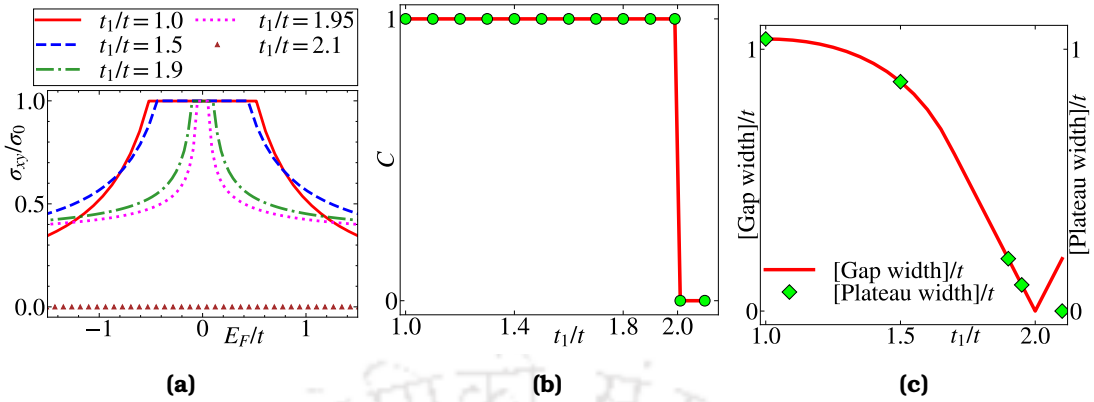

FIG. 2.11: (a) The variation of the Hall conductivity, σ_{xy} is shown as a function of Fermi energy, E_F for several values of t_1. Here $\sigma_0 = e^2/h$ is the unit of Hall conductance. In the calculation we have set $t_2 = 0.1t$ and $\phi = \pi/2$. It is evident from the figure that the plateau width decreases with increase in t_1 values. (b) The Chern number is plotted as a function of t_1/t. The Chern number stays at 1 for all values of $t_1 < 2t$ and vanishes for $t_1 > 2t$. (c) The gap width and the plateau width in Hall conductivity are shown as a function of t_1/t. They are labelled by the red curve and the green diamond points respectively. The plateau width is same as the gap width till $t_1 < 2t$. At $t_1 = 2.1t$ the width of the Hall plateau is zero but gap is non-zero.

Hall conductivity using (we repeat here for completeness),

$$\sigma_{xy} = \frac{e^2}{\hbar} \int \frac{\mathrm{d}\mathbf{k}}{(2\pi)^2} f\left(E_{\mathbf{k}}\right) \Omega(\mathbf{k}) \tag{2.11}$$

where $\Omega(\mathbf{k})$ denotes the z-component of Berry curvature which can be obtained from the derivatives of the $\mathbf{d}$ vector with respect to the momenta, k_x and k_y using (repeated here for convenience),

$$\Omega(\mathbf{k}) = \frac{\mathbf{d}}{2|\mathbf{d}|^3} \cdot \left(\frac{\partial \mathbf{d}}{\partial k_x} \times \frac{\partial \mathbf{d}}{\partial k_y} \right). \tag{2.12}$$

and $f(\epsilon) = [e^{\beta(\epsilon - E_F)} + 1]^{-1}$ is the Fermi-Dirac distribution function with β being the inverse temperature ($\beta = 1/k_B T$). The total Hall conductivity is the sum of σ_{xy} from all the bands. Using Eqs. (2.12) and (2.11) the Hall conductivity is calculated numerically and plotted as a function of the Fermi energy, E_F for $T = 0$ in Fig. 2.11(a). We can see that as long as the Fermi energy lies in the gap the Hall conductivity has a plateau and hence quantized in unit of e^2/h. The integral in Eq. (2.11) is performed over the states which are partially occupied at a given value of the Fermi energy. Consequently, the Hall conductivity decreases

rapidly as the Fermi energy moves away from the gapped region. In Fig. 2.11(a) the quantized plateau stays at e^2/h, except that the plateau width decreases with increase in the value of t_1. This occurs because the width of the energy gap in the spectrum decreases with the increasing strength of t_1, although the Hall plateau survives as long as the Fermi energy lies in the gap.

The above inference is supported by Fig. 2.11(b) where we plot the Chern number, C as a function of t_1/t. C stays at 1 as long as $t_1/t < 2$, implying continued existence of the topological phase, while as soon as t_1/t becomes slightly larger than 2, C drops to zero. Thus we get a normal insulator beyond the semi-Dirac limit.

We further derive support of the above scenario via Fig. 2.11(c), where we have shown the variation in the width of the Hall plateau and the width of the energy gap as a function of t_1/t. Here the band gap decreases with the increase in t_1 and the plateau width is found to be proportional to the energy gap. So the width of the Hall plateau follows the energy gap till $t_1 = 2t$. Again as t_1 becomes larger than $2t$, the plateau width vanishes, but the gap in the dispersion continues to exist.

2.6 Summary

We have investigated the evolution of the electronic spectrum and the topological properties in a Chern insulating model with deformable band properties. The tunable dispersion achieved by creating an anisotropy in hopping among a particular pair of nearest neighbours (t_1) as compared to the other two (t) is otherwise a well-studied problem, except that the presence of a non-zero Haldane flux yields significantly rich physics embedded therein. The model shows a topological phase transition from a Chern insulating regime to a trivial insulating phase as the above anisotropy is progressively made larger. Computation of the electronic dispersion shows the Dirac points move towards each other and finally merge at the M point where the conduction and the valence bands touch each other as the hopping amplitudes satisfy $t_1 = 2t$. Eventually, for larger values of t_1, the electronic spectrum gets gapped out again, where it shows properties of a trivial insulator.

These conclusions are supported by computing the band dispersion, DOS, edge modes, Berry curvature, the Chern number phase diagram and the anomalous Hall conductivity.

Chapter 3

Semi-Dirac Limit of (Real) Third Neighbour Hopping on a Honeycomb Lattice: Higher Chern Numbers

In the previous chapter, we have seen that the semi-Dirac system does not exhibit any non-trivial phases even in absence of the TRS which is in contrary to its Dirac counter part. Here we wish to explore the possibilities of achieving non-trivial phases in the semi-Dirac system via a suitable modification. A crucial point is that, unlike the Dirac case, addition of the complex second neighbour hopping in the semi-Dirac system does not open a gap in the electronic spectrum, instead the system still remains a semi-metal with the conduction and the valence bands touching each other at the M point in the BZ. A little introspection reveals that, in such a scenario we can add a real third neighbour hopping to shift the band extrema point in the energy spectrum, and hence look for the existence of the topological phases. It is known that the (real) second neighbour hopping in graphene is approximately 10% of that of the nearest-neighbour hopping [184]. Thus, a further neighbour would be even smaller. However, we will demonstrate that incorporating the third neighbor as a parameter in the tight-binding description yields intriguing phenomena. However, we shall see in the following that if the third neighbour is used as a parameter to the tight binding description, it yields interesting phenomenon.

The Dirac system with the third neighbour hopping has been discussed in literature [70]. However to the best of our knowledge, the semi-Dirac system in presence of the Haldane term and a real third neighbour hopping have never been discussed, and hence is new to the scientific community. An important dividend of such an exercise will be accessing regions in the phase diagram with large values of the Chern number [190], which also facilitates studying the topological phase transitions between phases with different Chern numbers. On both theoretical and experimental fronts, a variety of systems have been found that shows higher Chern numbers which we have already discussed in the Chapter 1 and are skipped them for brevity.

Motivated by the above scenario, here we discuss the topological properties of the semi-Dirac system in presence of a third neighbour (hence between different sublattices) hopping. We shall show that inclusion of the third neighbour hopping shifts the band minima from the boundary towards the interior of the BZ and makes the system a Chern insulator, with Chern numbers ± 2 for certain values of the hopping amplitude. Addition of the Semenoff mass to the problem changes Chern numbers from ± 2 to ∓ 1 for a specific range of values for the Semenoff mass and the third neighnour hopping amplitude. Consequently, we obtain the plateaus of the Hall conductivity that are quantized as Ce^2/h, with C being its Chern number and acquires values ± 1 and ± 2.

This chapter is organized as follows, in section 3.1 we show the semi-Dirac Hamiltonian in presence of a Haldane term and a real third neighbour hopping on a honeycomb lattice. In section 3.2, we investigate the topological properties by computing the Chern number for various values of the amplitude of the third neighbour hopping, and obtain the phase diagrams that demonstrate the existence (or absence) of the non-trivial topological phases. In section 3.3, we study the structure of the edge modes in a nanoribbon for various relevant values of the second and the third neighbour hopping amplitudes. Hence, we compute the anomalous Hall conductivities in section 3.4 that exhibit plateaus quantized in units of e^2/h and finally conclude with a brief summary of our results in section 3.5.

3.1 Model Hamiltonian

We consider a tight binding Hamiltonian on a honeycomb lattice with hopping between the various neighbours that can be written as,

$$H = \left[\sum_{\langle i,j\rangle} t_{ij} c_i^\dagger c_j + t_2 \sum_{\langle\langle i,k\rangle\rangle} e^{i\phi_{ik}} c_i^\dagger c_k + t_3 \sum_{\langle\langle\langle i,l\rangle\rangle\rangle} c_i^\dagger c_l + \text{h.c.}\right] + \sum_i \Delta_i c_i^\dagger c_i \qquad \boxed{3.1}$$

The first term is the nearest neighbour (N1) hopping. Here, for the sake of distinction with other hopping amplitudes, we shall refer to it as N1 hopping. The N1 hopping strengths (denoted by t_{ij}) along the $\boldsymbol{\delta}_2$ and the $\boldsymbol{\delta}_3$ directions are t, while along the $\boldsymbol{\delta}_1$ direction, the strength is t_1, as shown in Fig. 3.1. We have assumed two different values of t_1, such as, $t_1 = t$ and $t_1 = 2t$ (other intermediate values are not discussed here) which represent the isotropic Dirac and the semi-Dirac cases respectively. As the Dirac case has already been studied, the semi-Dirac case is the main focus for this chapter. The second term is the Haldane term comprising of a complex second neighbour (N2) hopping with an amplitude, t_2 and a complex phase denoted by ϕ_{ik} whose values have already been described in the previous chapter. The third term represents the third neighbour (N3) hopping between different sublattices and the fourth term represents the onsite energy (Semenoff mass), that assumes values $+\Delta$ and $-\Delta$ for sublattices A and B respectively. We have skipped mentioning the N1 and N2 vectors in this chapter for brevity. It may be noted that the anisotropic hopping amplitudes enter through the N1 hopping amplitudes, while N2 and N3 hoppings are left unaltered. Thus, the key symmetries, such as, chiral (with $\Delta = 0$) and particles-hole (subject to N2 hopping being purely imaginary) symmetries are not disturbed, while TRS remains broken all the while.

Performing a Fourier transform of Eq. 3.1, the Hamiltonian in the momentum space can be written as,

$$H(\mathbf{k}) = h_x(\mathbf{k})\sigma_x + h_y(\mathbf{k})\sigma_y + h_z(\mathbf{k})\sigma_z + h_0(\mathbf{k})I = \mathbf{h}(\mathbf{k}) \cdot \boldsymbol{\sigma} + h_0(\mathbf{k})I \qquad \boxed{3.2}$$

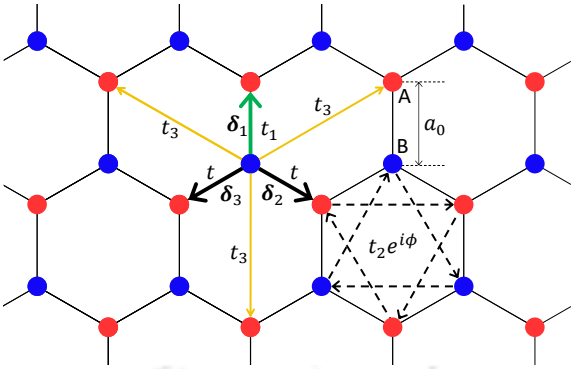

FIG. 3.1: A honeycomb lattice is shown where the red and the blue circles represent the sublattices A and B respectively. In the $\boldsymbol{\delta}_2$ and $\boldsymbol{\delta}_3$ directions the N2 hopping strengths are same (t), while in the $\boldsymbol{\delta}_1$ direction it is t_1. The N3 hopping is shown by the yellow arrow.

where,

$$h_x(\mathbf{k}) = \left\{ t_1 \cos k_y + 2t \cos\frac{k_y}{2} \cos\frac{\sqrt{3}k_x}{2} \right\} + t_3 \left\{ \cos 2k_y + 2\cos k_y \cos\sqrt{3}k_x \right\}, \quad 3.3$$

$$h_y(\mathbf{k}) = \left\{ -t_1 \sin k_y + 2t \sin\frac{k_y}{2} \cos\frac{\sqrt{3}k_x}{2} \right\} + t_3 \left\{ \sin 2k_y - 2\sin k_y \cos\sqrt{3}k_x \right\}, \quad 3.4$$

$$h_z(\mathbf{k}) = \Delta - 2t_2 \sin\phi \left\{ 2\sin\frac{\sqrt{3}k_x}{2} \cos\frac{3k_y}{2} - \sin\sqrt{3}k_x \right\} \quad 3.5$$

and,

$$h_0(\mathbf{k}) = 2t_2 \cos\phi \left\{ 2\cos\frac{\sqrt{3}k_x}{2} \cos\frac{3k_y}{2} + \cos\sqrt{3}k_x \right\} \quad 3.6$$

where σ_i ($i \in x, y, z$) denote the 2×2 spin-1/2 Pauli matrices which represent the sublattice degrees of freedom, and I is the 2×2 identity matrix. The energy dispersion can be obtained as,

$$E(\mathbf{k}) = h_0(\mathbf{k}) \pm \sqrt{h_x(\mathbf{k})^2 + h_y(\mathbf{k})^2 + h_z(\mathbf{k})^2}, \quad 3.7$$

where the $\pm$ signs refer to the upper (conduction) band and the lower (valence) band respectively. In the absence of t_2 and t_3, the band dispersion is linear along one direction and quadratic along its perpendicular direction [63] about the band touching M point in the BZ. We refer to this as the zero mode in our subsequent discussion.

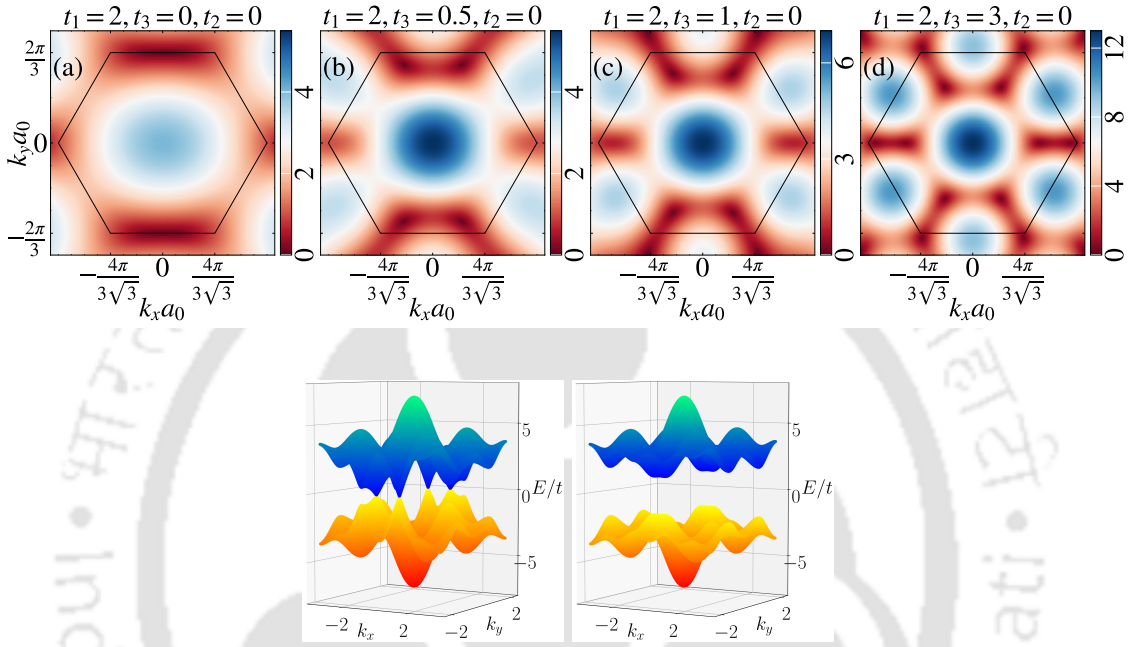

FIG. 3.2: The top view of the bandstructure for the semi-Dirac ($t_1 = 2t$) system is depicted for (a) $t_3/t = 0$, (b) $t_3/t = 0.5$, (c) $t_3/t = 1$ and (d) $t_3/t = 3$. The hexagons in each figure represent the first Brillouin zone. In the calculations, we have fixed $t_2 = 0$, $\Delta = 0$. In (e) and (f) a three dimensional depiction of the bandstructure for the semi-Dirac system are shown for $t_2 = 0$ and $t_2 = 0.5t$ respectively, where we have used $\Delta = 0$ and $\phi = \pi/2$.

Now, if we add a small N3 hopping, namely, t_3, then the zero modes shift from the M point towards the interior of the BZ as shown in Figs. 3.2(b)-3.2(d). There are four zero modes inside the first BZ for a non-zero value of t_3. Let us call these points where the zero modes occur as the $\mathbf{\Lambda}$ points. For example, one of the zero modes for a particular value of t_3, namely, $t_3 = t$ occurs approximately at a point, which we call as $\mathbf{\Lambda}_1 = \left(\frac{1.1560\pi}{3\sqrt{3}a_0}, \frac{1.5487\pi}{3a_0}\right)$. while the same for a different value of t_3, namely $t_3 = 3t$ approximately occurs at another, $\mathbf{\Lambda}_2 = \left(\frac{1.0805\pi}{3\sqrt{3}a_0}, \frac{1.2403\pi}{3a_0}\right)$. For other values of t_3, namely, say $t_3 > 3t$, the zero modes remain fixed at the same locations as that for $t_3 = 3t$. We wish to remind ourselves that t_3 is merely a

parameter in our model, and hence a large value such as this is only to access different topological phases and hence of academic interest.

Now, if we turn on the N2 hopping, t_2 then the spectral gaps open up at these Λ points in the BZ where the zero modes occur, and hence the system behaves as an insulator. However, in the absence of t_3 (with t_2 being non-zero), there is no gap at the M point, and the dispersion is anisotropic linear (linear along both the directions, but with different velocities along the x- and the y-directions) about the M point, which makes the system a semi-metal as discussed in Ref. [193]. In Figs. 3.2(e) and 3.2(f), we have shown the bandstructures for the semi-Dirac system in the absence, and in the presence of t_2 respectively for non-zero values of t_3. In our calculations, we have fixed the values of the Haldane flux, ϕ, N1 hopping, t_1 and the Semenoff mass, Δ to be $\pi/2$, $2t$ and zero respectively. The corresponding bandstructures for the Dirac system have been discussed in Ref. [191, 192], and we skip them here to make our discussion concise.

3.2 Phase diagram

In this section, we obtain the phase diagram by numerically calculating the Chern number of the system. Since in this model, the complex N2 hopping term breaks the TRS, non-zero values and hence non-trivial phases with finite Chern number are expected. The inversion symmetry breaking onsite energies, $\pm\Delta$ on different sublattices open or close energy gaps in the energy spectrum at the Λ points. We compute the Chern number using Eq. 1.21 (see Sec. 1.1.3) as a function of Δ and t_3, and plotted it in the phase diagram in Fig. 3.3.

It is to be noted that in the absence of an N3 hopping, the Chern number is always zero for any arbitrary value of Δ and ϕ for the semi-Dirac case ($t_1 = 2t$), even though the time reversal symmetry remains broken. However in presence of the non-zero N3 hopping, we may obtain non-zero values for the Chern number. In Fig. 3.3(a) we have depicted the Chern number corresponding to the lower band as a function of Δ and t_3 for Haldane flux, $\phi = \pi/2$. As can be seen, there are two regions denoted by the red and the green colours. The region in red indicates the value of the Chern number, $C = 1$, while the green region indicates

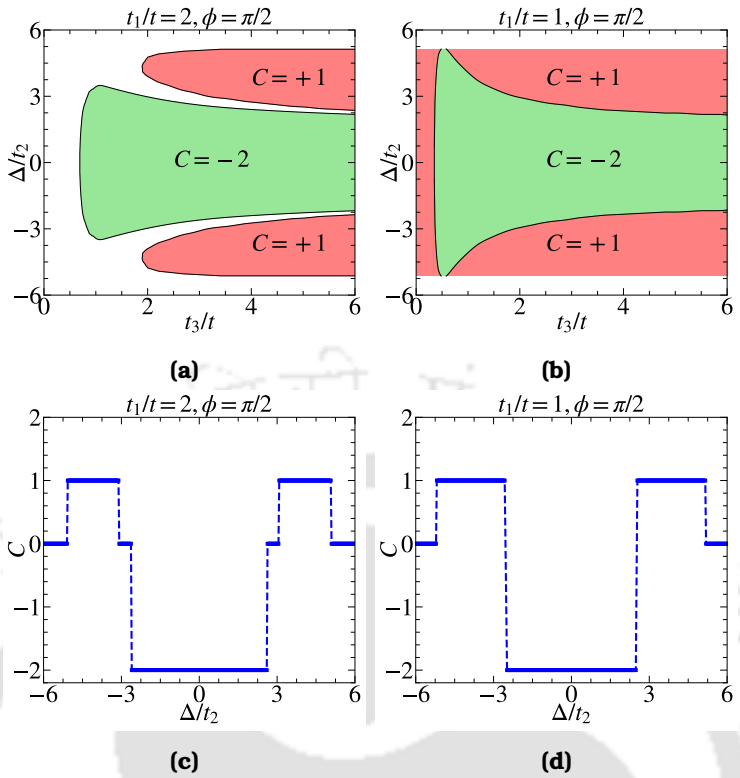

FIG. 3.3: The Chern number of the lower band is depicted as a function of Δ and t_3 for (a) $t_1/t = 2$ and (b) $t_1/t = 1$. The coloured regions signify the Chern insulating regions with non-zero Chern numbers ($C = +1$ for the red region and $C = -2$ for the green one), while the white region denotes the trivial insulating phase with $C = 0$. We have shown the variation of C as a function of Δ for a particular value of t_3, say $t_3 = 3t$, in (c) and (d) for $t_1/t = 2$ and $t_1/t = 1$ respectively. In this calculation, the Haldane flux ϕ is kept fixed at $\pi/2$. The topological phase transitions are implied via C discontinuously changing values between $1 \to 0 \to -2$.

$C = -2$. In addition, there is also a finite region denoted by the white colour, which corresponds to a trivial region with $C = 0$. In absence of t_3 or at small values of t_3, namely $t_3 < 0.68t$, for all values of Δ, the trivial region prevails. We observe the topological phase with the Chern number $C = -2$ beyond a certain value of the N3 hopping, t_3, namely $t_3 \gtrsim 0.68t$, for a zero Semenoff mass ($\Delta = 0$). If we increase the value of Δ, then we observe the $C = -2$ phase for a range of values of t_3, such as, $0.68t \lesssim t_3 \lesssim 1.9t$. However, for $t_3 \gtrsim 1.9t$, there are two topological phases with Chern numbers $C = 1$ and $C = -2$, which depend on the value of Δ. For example, for $t_3 = 3t$, there is phase transition occurring from a $C = 0$ to a $C = 1$ phase at $\Delta \simeq -5.04t_2$. C again drops to zero for $\Delta \simeq -3.11t_2$. Beyond $\Delta \simeq -2.56t_2$, the Chern number becomes -2 and stays at -2 until a specific value

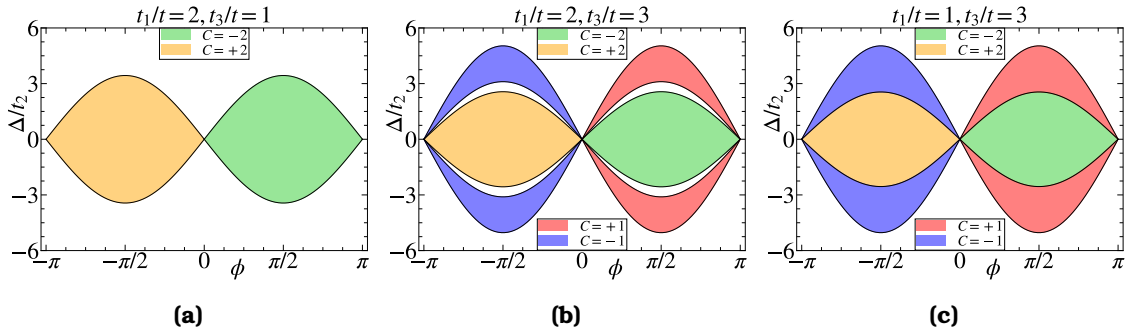

FIG. 3.4: The Chern numbers of the lower band is shown as a function of Δ and ϕ for (a) $t_1/t = 2$ and $t_3/t = 1$, (b) $t_1/t = 2$ and $t_3/t = 3$ and (c) $t_1/t = 1$ and $t_3/t = 3$. In each figure, the green and the orange regions denote the Chern insulating phase with the Chern numbers -2 and +2 respectively, while the red and the blue regions imply the Chern numbers +1 and -1 respectively. Further, the white region denotes trivial topological regime with zero Chern number.

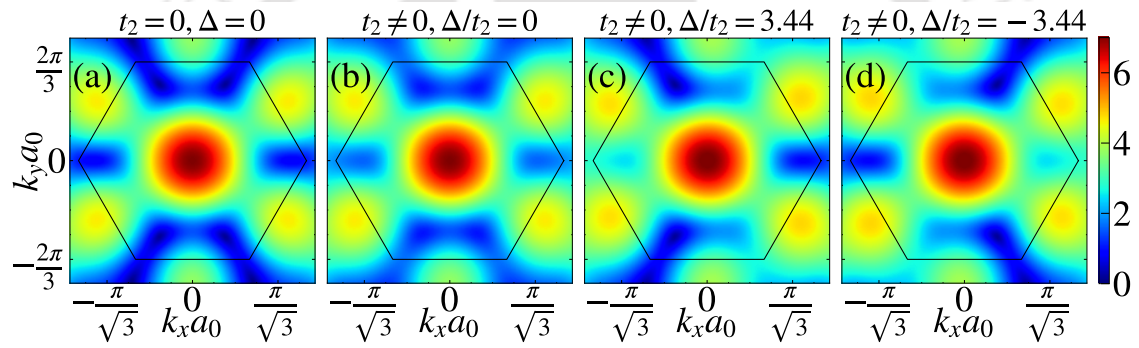

FIG. 3.5: The conduction band of the semi-Dirac system ($t_1 = 2t$) is shown in (a) in absence of t_2 and the Semenoff mass Δ, while the same in presence of a non-zero t_2 are presented in (b), (c) and (d) for $\Delta = 0$, $\Delta/t_2 = 3.44$ and $\Delta/t_2 = -3.44$ respectively. The values of t_3 and ϕ are taken as t and $\pi/2$ respectively.

of Δ, namely, $\Delta \simeq 2.56t_2$, when the Chern number vanishes again. The Chern number becomes 1 at $\Delta \simeq 3.11t_2$, and finally vanishes again for $\Delta \gtrsim 5.04t_2$. Thus there are a series of phase transitions occurring at $t_3 = 3t$. There is always a trivial region (with $C = 0$) in between the two Chern insulating regions having two different Chern numbers (the white region between the red and the green regions). Further, as one increases the value of t_3, the regions with zero Chern numbers ($C = 0$) are obtained for lesser values of Δ. As a result, the width of the Chern insulating region with $C = -2$ (the green region) shrinks with the increase of t_3, or equivalently, we can say, the width of the $C = 1$ region increases with the

increase in N3 hopping t_3. The trivial region (shown in white in Fig. 3.3(a)) gets narrower as one increases the value of t_3.

This phenomenon is somewhat different in the Dirac case (see Fig. 3.3(b)), where we can see a non-zero Chern number (namely, $C = 1$) even in absence of the N3 hopping, that is, the well-known Haldane model. The phase persists for very small values of t_3. However in the presence of N3 hopping, we obtain a phase with Chern number $C = -2$ or $C = 1$ depending on the value of Δ. Further, unlike the semi-Dirac case, there is no trivial regime in between the two different Chern insulating regimes, that is, the red and the green regions. If we fix the value of t_3, say, $t_3 = 3t$, and calculate the Chern numbers for increasing values of Δ, then we observe the Chern number to jump from $C = -2$ to $C = 1$ at $\Delta \simeq 2.55t_2$. Finally, the Chern number drops to zero from a value $C = 1$ at $\Delta = 3\sqrt{3}t_2$. The values of Δ, at which the Chern number changes from a value $C = -2$ to $C = 1$, depend on the value of the N3 hopping t_3 (see the shoulder like region in Fig. 3.3(b)). However, the values of Δ at which the Chern number vanishes from a value $C = 1$ does not depend upon t_3. It should be noted that the calculations are done for a Haldane flux, $\phi = \pi/2$. If we alter the value of ϕ to $-\pi/2$ then the phase diagram will remain unchanged, except that the Chern numbers will undergo a sign change.

In Figs. 3.3(c) and 3.3(d), we have shown the variation of Chern numbers as a function of Δ for the semi-Dirac ($t_1 = 2t$) and the Dirac systems ($t_1 = t$) respectively for a particular value of t_3, say, $t_3 = 3t$. As can be seen for the semi-Dirac case (see fig. 3.3(c)), there are phase transitions occurring from $C = 0$ to $C = 1$ and then again to $C = 0$ as one increases Δ. With further increase of Δ, C drops to -2. To quote some numerical values, the plateau at $C = -2$ exists for a range of Δ, that is, $-2.56t_2 \lesssim \Delta \lesssim 2.56t_2$. With further increase in the value of Δ, C drops to zero and then again rises to 1 and finally vanishes. The plateaus at $C = 1$ persist for some values of Δ, such that, $-5.04t_2 \lesssim \Delta \lesssim -3.11t_2$ and $3.11t_2 \lesssim \Delta \lesssim 5.04t_2$. A similar phase transitions are observed for the Dirac case (see Fig. 3.3(d)), except that there is direct phase transitions from $C = 1$ to $C = -2$ or vice versa. The $C = -2$ plateau occurs for $-2.55t_2 < \Delta < 2.55t_2$, while the plateaus at $C = 1$ occur for $-3\sqrt{3}t_2 \leq \Delta \lesssim -2.55t_2$ and $2.55t_2 \lesssim \Delta \leq 3\sqrt{3}t_2$.

TABLE. 3.1: The value of Chern numbers for various values of Δ and t_3 are presented. The upper table corresponds to the semi-Dirac case, while the lower one corresponds to the Dirac case.

$t_1 = 2t$

	The range/value of Δ	The range/value of t_3
$C = 0$	$\Delta = 0$	$0 \leq t_3 < 0.68t$
$C = -2$		$t_3 \gtrsim 0.68t$
$C = +1$	$5.04t_2 \lesssim \lvert\Delta\rvert \lesssim 3.11t_2$	$t_3 = 3t$
$C = -2$	$\lvert\Delta\rvert \lesssim 2.56t_2$	
$C = +1$	$\lvert\Delta\rvert = 4.38t_2$	$t_3 \gtrsim 1.9t$

$t_1 = t$

	The range/value of Δ	The range/value of t_3
$C = +1$	$\Delta = 0$	$0 \leq t_3 < 0.4t$
$C = -2$		$t_3 \gtrsim 0.4t$
$C = +1$	$3\sqrt{3}t_2 \lesssim \lvert\Delta\rvert \lesssim 2.55t_2$	$t_3 = 3t$
$C = -2$	$\lvert\Delta\rvert \lesssim 2.55t_2$	
$C = +1$	$\lvert\Delta\rvert \approx 3\sqrt{3}t_2$	$t_3 \gtrsim 0.51t$

We summarize the preceding discussion in Table 3.1.

Fig. 3.4 shows the phase diagram in the Δ-ϕ plane corresponding to the lower band for both the semi-Dirac and the Dirac cases. For both of them, the values of the Chern number depend on the value of N3 hopping amplitude (see Fig. 3.3). In Fig. 3.4(a), we have shown the phase diagram for the semi-Dirac case for $t_3 = t$. As can be seen, there are two Chern insulating regions with Chern numbers $C = -2$ (green region) and $C = +2$ (yellow region). The phase diagram is similar to that of the Haldane model, except that the values for the Chern number are different in this case. Further, the widths of the Chern insulating lobes are smaller than those in the Haldane model. Now, if we increase the value of t_3 (say, $t_3 = 3t$), we shall see additional Chern insulating regions emerge, with the Chern numbers given by $C = +1$ (red region) and $C = -1$ (blue region) as depicted in Fig. 3.4(b). There exists a trivial insulating phase with $C = 0$ in between the two Chern insulating regions, that is, between the green and the red regions, or between the yellow and the blue regions. These types of phase diagrams are in

complete contrast with the Dirac case, where in the latter, the trivial insulating phase is absent as shown in Fig. 3.4(c). The width of the Chern insulating region with $C = -2$ is greater in the Dirac case compared to that of the semi-Dirac case (see Fig. 3.4(c)), as is evident from the Δ-t_3 phase diagram (Fig. 3.3(b)). For vanishingly small values of t_3, which are physically relevant, the phase diagram becomes similar to that of the Haldane model.

The reason of having a value of the Chern number $|C| = 2$ is that we have multiple zero modes in presence of t_3 (and in absence of t_2) inside the first BZ for the semi-Dirac system. For example, when $t_3 = t$, the zero modes occur at four Λ points as depicted in Fig. 3.5(a), which are perceptible from the dark blue colours. Gaps open up at those Λ points, as we turn on the N2 hopping t_2 (see Fig. 3.5(b)). The Chern number of the system becomes -2. Now, if we keep increasing the value of the Semenoff mass, Δ, the gaps at two out of four Λ points decrease, and finally vanish at $\Delta \approx 3.4372$ (see Fig. 3.5(c)), where a topological phase transition takes place. For $\Delta \gtrsim 3.4372$, the gaps open up again, however the Chern number vanishes. A similar gap closing scenario occurs at the remaining two Λ points for $\Delta \approx -3.4372$ (see Fig. 3.5(d)).

The phase diagrams presented in Figs. 3.3 and 3.4 aid us in identifying specific values of t_3 and Δ to explore the nature of the topological phases. We achieve that via the numerical computation of the edge states and the anomalous Hall conductivity as discussed below. These quantities are investigated for $t_3 = 0.5t$, t and $3t$, where we have considered $\Delta = 0$ corresponding to $t_3 = 0.5t$ and t, while the $t_3 = 3t$ case has been studied for $\Delta = 0$ and $\Delta = 4t_2$, which, correspond to $C = -2$ and $C = 1$ respectively.

3.3 Edge states

In order to understand whether the nature of the band gaps are topological or trivial, we look for the existence (or absence) of the edge states. To achieve this, we have considered the system to have semi-infinite ribbon geometry with zigzag edges along the periodic x-direction. We Fourier transform the operators along the x-direction (because of the translational symmetry) which yields two sets of

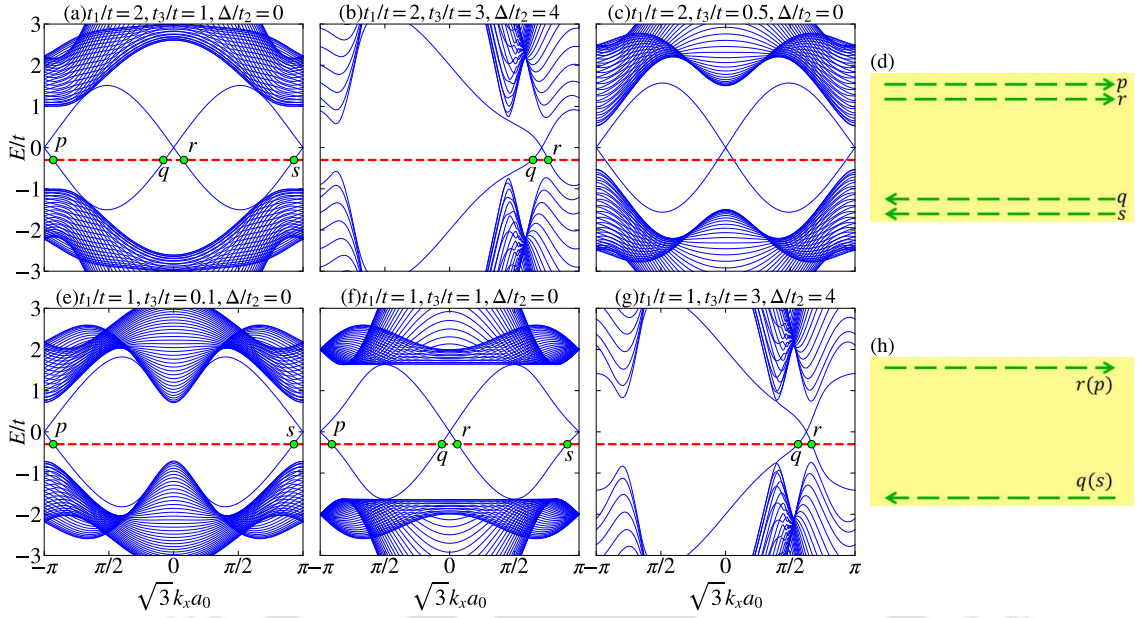

FIG. 3.6: The energy spectra of the ribbon as a function of the dimensionless momentum k (here k denotes $\sqrt{3}a_0k_x$) for the semi-Dirac system ($t_1/t = 2$) are shown in (a) $t_3/t = 1$, $\Delta/t_2 = 0$ (b) $t_3/t = 3$, $\Delta/t_2 = 4$ and (c) $t_3/t = 0.5$, $\Delta/t_2 = 0$, while for the Dirac system ($t_1/t = 1$) it is shown in (e) $t_3/t = 0.1$, $\Delta = 0$, (f) $t_3/t = 1$, $\Delta = 0$ and (g) $t_3/t = 3$, $\Delta/t_2 = 4$. The green dots in each figure signify the intersection of the edge states with the Fermi energy E_F (shown via the red dashed line). (d) and (h) are Schematic diagrams of a part of the ribbon. The arrows in (d) represent the edge currents corresponding to the points of figure (a) and (f), while in (h) the edge currents are shown corresponding to the points of figure (b), (e) and (g).

coupled eigenvalue equations for the wave functions as follows,

$$E_k a_{k,n} = -\left[t\left\{1+e^{(-1)^n ik}\right\}b_{k,n} + t_1 b_{k,n-1}\right] + t_3\left[b_{k,n+3} + 2b_{k,n-1}\cos k\right] + \Delta a_{k,n} - 2t_2\left[\cos(k+\phi)a_{k,n} + e^{(-1)^n \frac{ik}{2}}\cos\left(\frac{k}{2}-\phi\right)\left\{a_{k,n-1}+a_{k,n+1}\right\}\right] \quad 3.8$$

$$E_k b_{k,n} = -\left[t\left\{1+e^{(-1)^{n+1} ik}\right\}a_{k,n} + t_1 a_{k,n+1}\right] + t_3\left[a_{k,n-3} + 2a_{k,n+1}\cos k\right] - \Delta b_{k,n} - 2t_2\left[\cos(k-\phi)b_{k,n} + e^{(-1)^{n+1} \frac{ik}{2}}\cos\left(\frac{k}{2}+\phi\right)\left\{a_{k,n-1}+a_{k,n+1}\right\}\right] \quad 3.9$$

where n denotes the site index. n assumes integer values in the range $[1 : N]$ with N being the total number of unit cells along the y-direction. In Eqs. 3.8 and 3.9, $a_{k,n}$ and $b_{k,n}$ are the coefficients of the wave functions corresponding to the

n-th A and B sublattices respectively. Here k is the momentum along the periodic x-direction, which is rendered dimensionless by defining, $k = \sqrt{3}a_0 k_x$. The width D of the ribbon along the y-direction is related to N via $D(N) = a_0\left(\frac{3N}{2} - 1\right)$. As earlier, we have used $N = 128$ and hence the ribbon has a width of $191a_0$. By solving Eqs. 3.8 and 3.9 one can get the bandstructure of the nanoribbon as shown in Fig. 3.6 for a fixed value of the Haldane flux, namely $\phi = \pi/2$. As can be seen, one of the edge modes from the lower band crosses over to the upper band as a function of k_x, and another one traverses in the opposite direction. These edge modes are responsible for a finite value of the Hall conductivity, provided the Fermi energy lies in the bulk spectral gap. In Fig. 3.6(a), we show the edge states for the semi-Dirac ($t_1 = 2t$) system corresponding to a particular value of the N3 hopping, for example, $t_3 = t$. The red dashed line represents the Fermi energy, E_F and the points where the edge modes intersect the Fermi energy are shown by green dots. The edge currents corresponding to the points 'p' and 'r' flow along one of the zigzag edges of the ribbon and the edge currents corresponding to the points 'p' and 's' travel along the other edge (see Fig. 3.6(g)). However they flow in the opposite directions, since the velocity of the electron is proportional to the slope of electron dispersion, that is, $\partial E/\partial k$, which alters sign at (q, s) compared to those at (p, r).

Owing to the presence of a pair of edge states, there will be finite Hall conductivity with a plateau occurring at a value $n_e e^2/h$, where '$n_e = 2$' denotes the number of edge modes [189]. This result is consistent with the Chern number phase diagram (see Fig. 3.3(a)), where the Chern number is found to have a value -2 for $t_3 = t$ and $\Delta = 0$. In contrast, we get a single edge mode, along either edge of the ribbon for $t_3 = 3t$ and $\Delta = 4t_2$ as shown in Fig. 3.6(f). In this case, we show the edge currents corresponding to the points 'q' and 'r' in Fig. 3.6(h). This result is also consistent with the phase diagram (Fig. 3.3(b)), where we find $C = 1$. For $t_2 = 0.5$ and $\Delta = 0$, the edge modes are shown in Fig. 3.6(c). It is clearly visible that the edge modes are split from the bulk. Thus, one can say that the edge modes do not contribute to the edge current and hence the system possesses zero Hall conductivity.

The edge states for the Dirac system ($t_1 = t$) are shown for comparison in

Figs. 3.6(d), 3.6(e) and 3.6(f). The plots show the presence of single edge mode at the points 'p' and 's' for $t_3 = 0.1t$ and $\Delta = 0$ (Fig. 3.6(d)), which propagates at two opposite edges of the ribbon corresponding to the points 'p' and 's'. Such a situation yields a plateau in the Hall conductivity at e^2/h. This result is similar to that of the Haldane model. Now, if we further increase the value of the N3 hopping, for example, consider $t_3 = t$ (Fig. 3.6(e)), a pair of edge modes appear, and they propagate along two different edges of the ribbon, however these two pairs are counter propagating at the opposite edges (see Fig. 3.6(h)). In this case, the Hall plateau is quantized in unit of $2e^2/h$. The pair of the edge currents will exist as long as the Semenoff mass, Δ remains at a zero value. However, as we introduce a finite value of Δ, there is possibility that there will be single edge mode at each edge as depicted in Fig. 3.6(f). Here we see that the edge modes are along either edge of the ribbon corresponding to the points 'q' and 'r' as shown in Fig. 3.6(h). The number of edge currents along either edge of the ribbon is consistent with their values for the Chern numbers, namely, $C = 1$ and $C = -2$ (see Fig. 3.3(b)).

3.4 Anomalous Hall conductivity

In this section, we describe the Hall conductivity of the system which is calculated numerically at zero temperature ($T = 0$) as a function of E_F using Eq. 1.39. The spectrum is shown in Fig. 3.7(a) corresponding to the semi-Dirac system ($t_1 = 2t$). We see that as long the Fermi energy lies in the gapped region, the Hall conductivity shows a plateau quantized in unit of $2e^2/h$ for $t_3 = t$ and $\Delta = 0$. Since the integral is performed over the occupied states for a given value of E_F, the Hall conductivity decreases as E_F moves away from the gapped region, that is, towards the bulk. If we consider the Semenoff mass, Δ to be zero, we see that the plateaus occur at $2e^2/h$ as shown by the green and the red curves in Fig. 3.7(a). However, in presence of a finite value of Δ, there is a possibility of getting a plateau at e^2/h occurring in σ_{xy} as shown by the blue curve in Fig. 3.7(b). These results are supported by the respective values for the Chern numbers. Thus, corresponding to $C = -2$, we get the Hall plateau quantized at a value $2e^2/h$, and

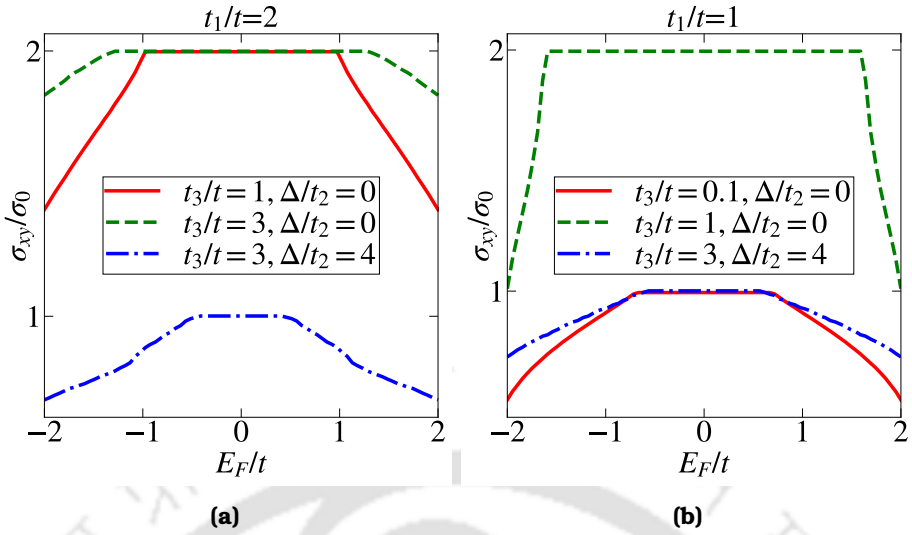

FIG. 3.7: The variation of anomalous Hall conductivity, σ_{xy} is shown as a function of the Fermi energy E_F for (a) $t_1/t = 2$ and (b) $t_1/t = 1$. Here $\sigma_0 = e^2/h$ is the unit of the Hall conductivity. In this calculation we have fixed the N2 hopping t_2 at $0.5t$ and the Haldane flux ϕ at $\pi/2$.

for $C = 1$, we get it is quantized at e^2/h.

To compare with the Dirac case, that is, for $t_1 = t$, we have shown the anomalous Hall conductivity in Fig. 3.7(b). As can be seen, with a small N3 hopping (say, $t_3 = 0.1t$), the Hall plateau is quantized in unit of e^2/h (the red curve in Fig. 3.7(b)). If we increase the value of the N3 hopping, the quantized Hall conductivity is seen at $2e^2/h$. Now, if we add the Semenoff mass term, the quantized Hall conductivity acquires a plateau at e^2/h. The value of Δ till which the e^2/h plateau is retained depends on the value of t_3. In Fig. 3.7(b), we show the Hall conductivity for a non-zero Δ by the blue curve corresponding to $t_3 = 3t$. The existence of the e^2/h Hall plateau is noted for a certain range of Δ, that is, $2.5t_2 \lesssim \Delta \lesssim 3\sqrt{3}t_2$ corresponding to a fixed value of N3 hopping, namely, $t_3 = 3t$. Similar to the case of the semi-Dirac system, the quantized Hall conductivity of the Dirac system is fully consistent with the corresponding Chern number phase diagrams (see Fig. 3.3(b)).

3.5 Summary

We have shown that in the semi-Dirac system, adding a third neighbour hopping causes the zero modes to move inward into the BZ from its boundary. Addition of the Haldane term creates spectral gaps at those points. We have obtained two different phase diagrams, namely, in the parameter spaces defined by Δ-ϕ and Δ-t_3 by computing the Chern numbers for the respective cases. The Δ-t_3 phase diagram is an addition to the existing literature. Further, the Δ-t_3 phase diagram for the semi-Dirac case encodes different scenario than the Dirac case in the following sense. There is always a trivial regime in between the two Chern insulating regimes ($C = -2$ and $C = 1$), which is absent for the Dirac case. The Δ-ϕ phase diagram for the semi-Dirac case shows that one may have Chern insulating regions either with $|C| = 2$ and $|C| = 1$, or only $|C| = 2$, depending on the value of the N3 hopping, t_3. The computation of the edge states show additional crossing of the edge modes corresponding to $|C| = 2$. Finally, the anomalous Hall conductivities, for several values of t_3, demonstrate the existence of Hall plateaus quantized either at $2e^2/h$ or at e^2/h depending on the number of edge modes crossing the Fermi energy.

Chapter 4

Topological Properties of a Bernal Stacked Bilayer Graphene

All of our previous work deals with monolayer systems in which the topological features were controlled by the properties of their bands. In this chapter, we will explore a bilayer topological model that is even more intriguing because it offers another way to achieve higher Chern numbers. This is due to the presence of a larger number of bands in its band structure, specifically two conduction bands and two valence bands. A higher value of the Chern number implies higher value of the anomalous Hall conductivity, together with larger number of chiral edge modes present in the system. It is instructive to investigate how band engineering affects the topological properties of such bilayer systems. Similar to the earlier case, band deformation can also be introduced via anisotropic hopping along a specific direction. The topological properties of such band-engineered bilayer systems are fascinating since they exhibit a richer phase diagram, and the existence of chiral edge modes and quantized Hall conductivity has not been studied in the literature before.

Therefore, in this chapter, we focus on a bilayer graphene with broken TRS, that is, a coupled bilayer Haldane model. The stacking of the two layers is assumed in such a way that the B sublattice of the upper layer lies exactly above the A sublattice of the lower layer. Such stacking is known as the AB stacking or the Bernal stacking. We shall see that the Chern numbers associated with

various bands reveal interesting properties. For example, some of the bands possess both Chern numbers ± 2 and ± 1, while the rests are associated with Chern numbers ± 1. Such a scenario needs to be assessed for a band engineered system. Specifically, we wish to address the ramifications of the band deformation caused via asymmetric hopping amplitudes on the topological properties and ascertain whether such deformation induces a topological phase transition. In our bilayer model, band engineering is incorporated via asymmetric NN hopping amplitudes in each of the layers, while the tunneling amplitude across the layers is left unaltered. It should be noted that the AA stacking of graphene also demonstrates non-trivial phases [194]. However, it needs elaborate investigation and is not considered in this thesis.

Our subsequent discussions are arranged as follows. Sec. 4.1 introduces the tight binding Hamiltonian of a bilayer graphene. Sec. 4.2 discusses the band structure of the system with the interlayer coupling ($t_\perp$) and the anisotropic NN hopping amplitudes (t_1) as parameters. Sec. 4.3 deals with the phase diagram that are obtained by computing the Chern numbers associated with the bands. In Sec. 4.4, the presence (or absence) of the chiral edge modes in a ribbon geometry are presented. Next, the numerical computations of the anomalous Hall conductivity are shown in Sec. 4.5. Finally, a brief summary of the results are included in the concluding section (Sec. 4.6).

4.1 The Hamiltonian

A tight-binding Hamiltonian of a bilayer honeycomb lattice can be written as follows,

$$H = \sum_{p\in l,u}\left[\sum_{\langle ij\rangle} t_{ij} c_i^{p\dagger} c_j^p + t_2 \sum_{\langle\langle im\rangle\rangle} e^{i\phi_p^{im}} c_i^{p\dagger} c_m^p + \text{h.c.}\right] + \left[t_\perp \sum_{\langle q,r\rangle_\perp} c_q^{l\dagger} c_r^u + \text{h.c.}\right] \quad \text{4.1}$$

where $c_i^{p\dagger}(c_i^p)$ is the creation (annihilation) operator corresponding to site i which belongs to the layer p. Here $p = l, u$ represent the lower and the upper layers respectively. The first term in the right hand side denotes the nearest neighbour (NN) hopping with the amplitude t_{ij} being either t_1 when i and j sites lie along

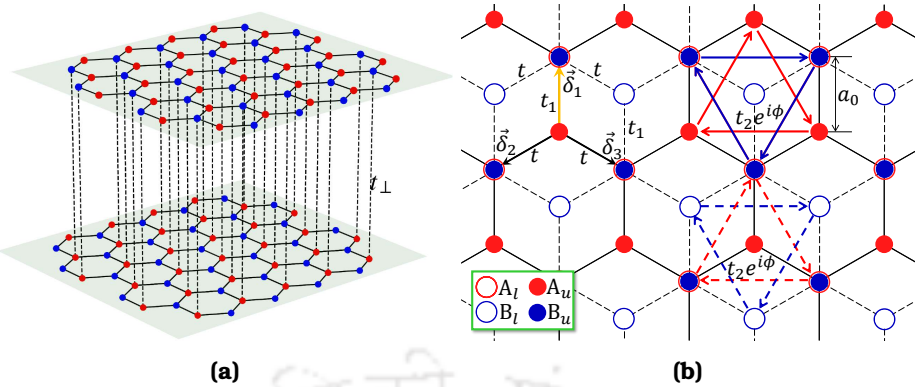

FIG. 4.1: A bilayer graphene is shown in (a) with the interlayer coupling $t_\perp$ between the B sublattice of upper layer and the A sublattice of lower layer. In both layers, the A and B sublattices are denoted by the red and blue filled circles. In (b), the other planar hoppings are shown. To properly see each sublattices in each layer, we have denoted the A and B sublattices in lower layer with the circles in red and blue respectively. The subscripts l and u in $\mathrm{A}_{l,u}$ and $\mathrm{B}_{l,u}$ refers to lower and upper layer respectively. All the bondings and NNN hoppings in the lower layers are shown by the dashed lines and dashed arrows respectively. The NN hopping strength along the $\boldsymbol{\delta}_1$ direction (shown via the yellow arrow) is t_1, while it is t along the $\boldsymbol{\delta}_{2,3}$ directions ($\boldsymbol{\delta}_i$ are defined in text). The NNN hopping is $t_2e^{i\phi}$ ($t_2e^{-i\phi}$) for the clockwise (anti-clockwise) direction.

the $\boldsymbol{\delta}_1$ direction, or t when they lie along the $\boldsymbol{\delta}_{2,3}$ directions as shown in Fig. 4.1. The second term represents the complex next nearest neighbour (NNN) hopping with the amplitude t_2 and a phase $\phi^{im}_{l,p}$. We have labelled the Haldane flux corresponding to the lower and upper layers as ϕ^{im}_l and ϕ^{im}_u respectively. Both acquire a positive or negative sign when an electron hops in the counter-clockwise or clockwise direction. The third term is the hopping between the two layers with the coupling strength $t_\perp$. t is important to note that the interlayer hopping occurs between the B sublattice on layer u ($r \in \mathrm{B}_u$) and the A sublattice on layer l ($q \in \mathrm{A}_l$) (AB or Bernal stacking). In our calculations, we have varied t_1 in both the layers from a value t to $2t$ (semi-Dirac limit) and also considered the case $t_1 > 2t$.

Now, we Fourier transform the Hamiltonian and write them in the four sub-

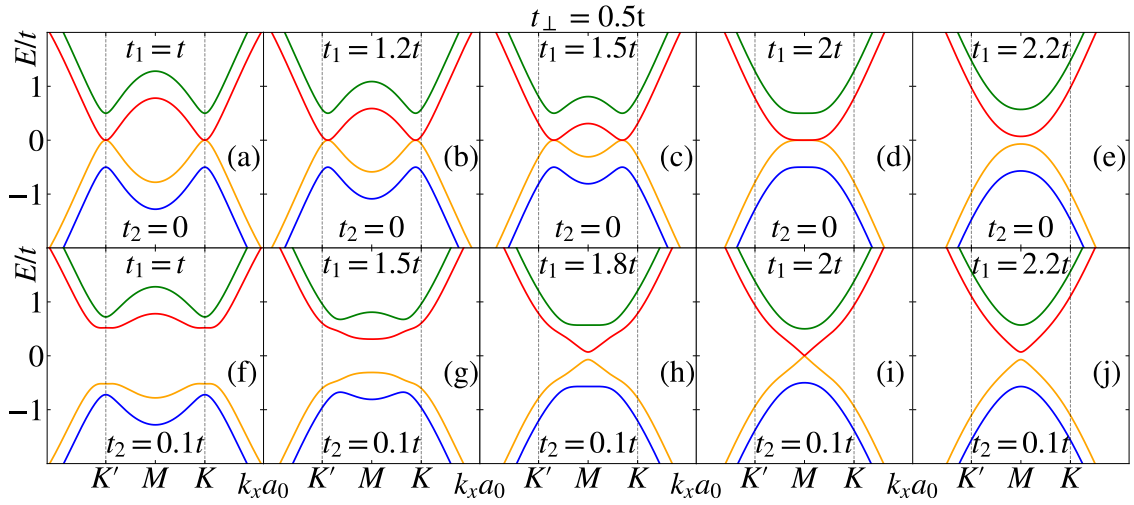

FIG. 4.2: The band structure in absence of t_2 ($t_2 = 0$) is shown along the k_x-axis (at $k_y a_0 = 2\pi/3$) for (a) $t_1 = t$, (b) $t_1 = 1.2t$, (c) $t_1 = 1.5t$, (d) $t_1 = 2t$, and (e) $t_1 = 2.2t$. Similarly, the dispersions in presence of t_2 ($t_2 = 0.1t$) are depicted for (f) $t_1 = t$, (g) $t_1 = 1.5t$, (h) $t_1 = 1.8t$, (i) $t_1 = 2t$, and (j) $t_1 = 2.2t$. The values of the other parameters are $t_\perp = 0.5t$ and $\phi_l = \phi_u = \pi/2$.

lattice basis, namely, $\{\mathrm{A}_l, \mathrm{B}_l, \mathrm{A}_u, \mathrm{B}_u\}$ in the following way,

$$H(\mathbf{k}) = \begin{pmatrix} h_z^+(\mathbf{k},\phi_l) & h_{xy}(\mathbf{k},t_1) & 0 & t_\perp \\ h_{xy}^*(\mathbf{k},t_1) & h_z^-(\mathbf{k},\phi_l) & 0 & 0 \\ 0 & 0 & h_z^+(\mathbf{k},\phi_u) & h_{xy}(\mathbf{k},t_1) \\ t_\perp & 0 & h_{xy}^*(\mathbf{k},t_1) & h_z^-(\mathbf{k},\phi_u) \end{pmatrix} \quad \text{4.2}$$

where $h_z^\pm$ are defined as, $h_z^+(\mathbf{k},\phi_p) = h_0(\mathbf{k},\phi_p) \pm h_z(\mathbf{k},\phi_p)$. The element $h_{xy}(\mathbf{k},t_1)$ has the following form, $h_{xy}(\mathbf{k},t_1) = h_x(\mathbf{k},t_1) - ih_y(\mathbf{k},t_1)$. The expressions for the h_is can be written as,

$$h_0(\mathbf{k},\phi_p) = 2t_2\cos\phi_p\left\{2\cos\frac{\sqrt{3}k_x}{2}\cos\frac{3k_y}{2} + \cos\sqrt{3}k_x\right\} \quad \text{4.3}$$

$$h_z(\mathbf{k},\phi_p) = -2t_2\sin\phi_p\left\{2\sin\frac{\sqrt{3}k_x}{2}\cos\frac{3k_y}{2} - \sin\sqrt{3}k_x\right\}, \quad \text{4.4}$$

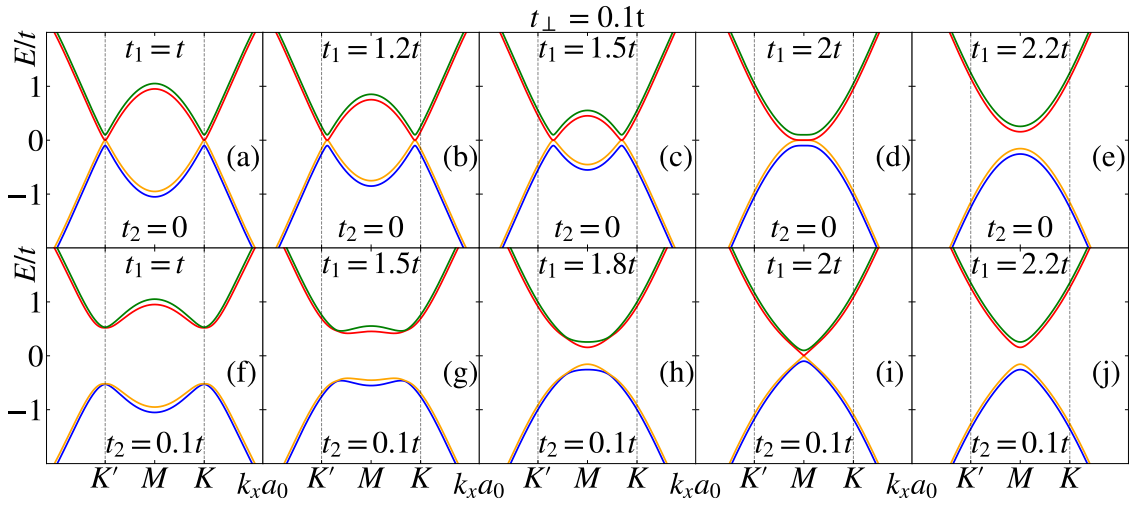

FIG. 4.3: The band structure for $t_2 = 0$ is shown along the k_x-axis (at $k_y a_0 = 2\pi/3$) for (a) $t_1 = t$, (b) $t_1 = 1.2t$, (c) $t_1 = 1.5t$, (d) $t_1 = 2t$, and (e) $t_1 = 2.2t$. While, the spectra for a non-zero t_2 ($t_2 = 0.1t$) are depicted for (f) $t_1 = t$, (g) $t_1 = 1.5t$, (h) $t_1 = 1.8t$, (i) $t_1 = 2t$, and (j) $t_1 = 2.2t$. The values of $t_\perp$, ϕ_l and ϕ_u are fixed at $0.1t$, $\pi/2$ and $\pi/2$ respectively.

$$h_x(\mathbf{k}, t_1) = \left\{ t_1 \cos k_y + 2t \cos\frac{k_y}{2} \cos\frac{\sqrt{3}k_x}{2} \right\}, \tag{4.5}$$

and

$$h_y(\mathbf{k}, t_1) = \left\{ -t_1 \sin k_y + 2t \sin\frac{k_y}{2} \cos\frac{\sqrt{3}k_x}{2} \right\}, \tag{4.6}$$

Throughout our work, the amplitude of the NNN hopping t_2 is kept fixed at $0.1t$, and two different values of the interlayer hopping strength are chosen, namely, $t_\perp = 0.5t$ and $t_\perp = 0.1t$. The values of ϕ_l and ϕ_u are taken such that $\phi_l = \phi_u = \pi/2$. However, only for obtaining the Chern number phase diagrams, ϕ_l and ϕ_u are varied in the range $[-\pi : +\pi]$ (see Sec. 4.3). Now, for $\phi_u = \phi_l$, we obtain the following dispersion relation,

$$E^c_\pm = \left[h_0 + \sqrt{\frac{t_\perp^2}{2} + |h_{xy}|^2 + h_z^2 \pm \frac{t_\perp}{2}\sqrt{t_\perp^2 + 4h_{xy}^2}} \right] \tag{4.7}$$

$$E^v_\pm = \left[h_0 - \sqrt{\frac{t_\perp^2}{2} + |h_{xy}|^2 + h_z^2 \pm \frac{t_\perp}{2}\sqrt{t_\perp^2 + 4h_{xy}^2}} \right] \tag{4.8}$$

where $E^c_\pm$ denote the two conduction bands and $E^v_\pm$ are the two valence bands for a bilayer. We discuss the results on the band structure in detail in the subsequent section.

4.2 Spectral properties

In this section, we discuss how the spectral properties evolve as we interpolate between the Dirac and the semi-Dirac limits. We show the band structure for two different values of $t_\perp$. The first one is for $t_\perp = 0.5t$ as shown in Fig. 4.2. As can be seen, there are four bands which we have labeled as follows. The upper conduction band is labeled as band-c1, while the lower conduction band is band-c2. Similarly, the lower and the upper valence bands are labeled as band-v1 and band-v2 respectively. When $t_2 = 0$ (no Haldane flux), band-c2 and band-v2 touch each other at the Fermi level at the $\mathbf{K}$ and $\mathbf{K}'$ points (see Figs. 4.2(a)-4.2(d)). These points are referred to as the Dirac points. Further, with the increase in the value of t_1, we deviate from the Dirac limit, and the band touching points move close to each other which finally merge at $t_1 = 2t$. Beyond this value, that is, for $t_1 > 2t$, a gap opens up at the $\mathbf{M}$ point. Now, if we switch on t_2 (see Figs. 4.2(e)-4.2(i)), the spectral gap remains open for $t \leq t_1 < 2t$ and $t_1 > 2t$, while the gap vanishes exactly at the semi-Dirac limit, namely, $t_1 = 2t$. The gap closing scenario of the bilayer graphene is thus similar to the case of single layer graphene, where the energy gap between the conduction and valence band vanishes at the semi-Dirac limit, that is, at $t_1 = 2t$ [193].

Further, we have presented band structure in Fig. 4.3 for a smaller value of $t_\perp$, namely, $t_\perp = 0.1t$. It is obvious from Eqs. 4.7 and 4.8 that the separation among the conduction bands (band-c1 and band-c2) and that among the valence bands (band-v1 and band-v2) decreases with decrease in $t_\perp$. Moreover, the low energy dispersions of band-c2 and band-v2 about the band touching points have a linear behaviour which was quadratic for $t_\perp = 0.5t$. Thus, the massive electrons become progressively massless as we lower the value of $t_\perp$. Further, with the decrease in $t_\perp$, the spectral gap between band-c2 and band-v2 increases. For example, when $t_\perp = 0.1t$ the band gap is $\Delta E_g \simeq 1.0390t$ and $0.3124t$ for $t_1 = t$ and $1.8t$

respectively. While for $t_\perp = 0.5t$, $\Delta E_g \simeq 1.0335t$ and $0.1406t$ for $t_1 = t$ and $1.8t$ respectively. Thus the difference in energy is more noticeable as we move towards the semi-Dirac limit, that is, at large values of t_1.

4.3 Chern number and phase diagram

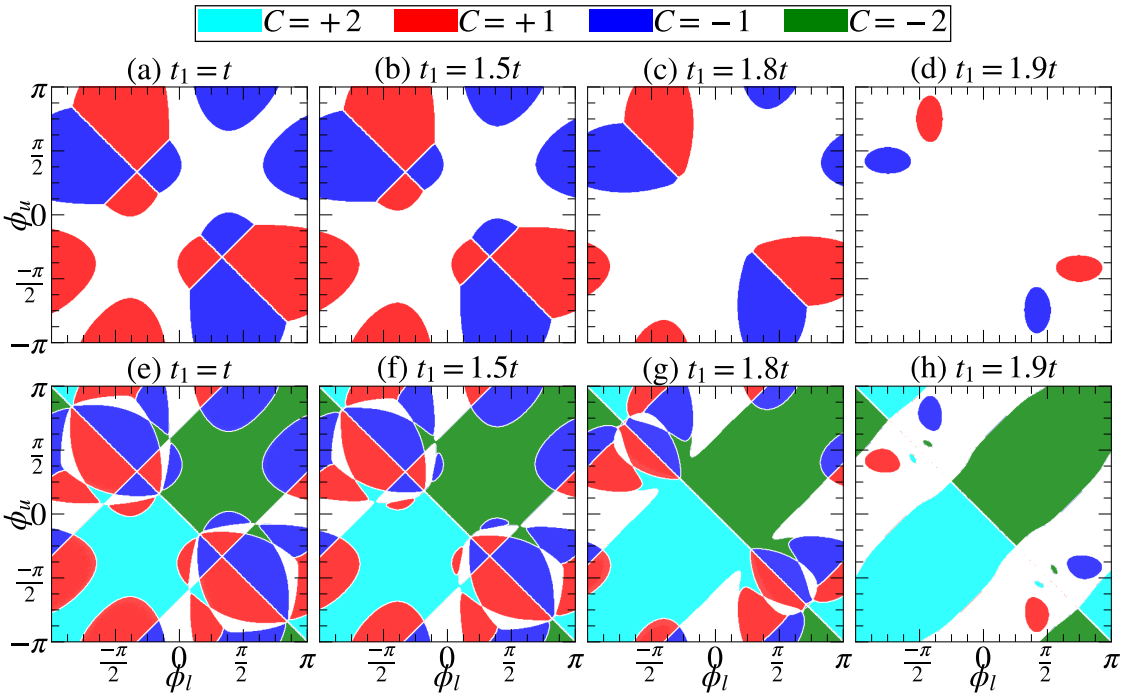

FIG. 4.4: The phase diagrams corresponding to the lowest occupied band, that is, band-v1 are presented in (a)-(d), while those for band-v2 are shown in (e)-(h). The white regions denote the trivial phase with Chern number as zero, while the colored regions indicate the non-trivial phase with the non-zero Chern numbers. The values of the Chern numbers corresponding to the colors are indicated at the top of the figure. The value of $t_\perp$ is kept fixed at $0.5t$.

In this section, we calculate the Chern number as a function of the fluxes ϕ_l and ϕ_u using Eq. 1.21 and shown in the phase diagrams in Fig. 4.4. Here the value of $t_\perp$ is chosen to be $0.5t$. The phase diagrams corresponding to band-v1 are shown in Figs. 4.4(a)-4.4(d), while Figs. 4.4(e)-4.4(h) corresponds to the phase diagrams of band-v2. We have denoted the Chern insulating regions by two different colors. The regions in red denote $C = +1$ phase, while the blue ones

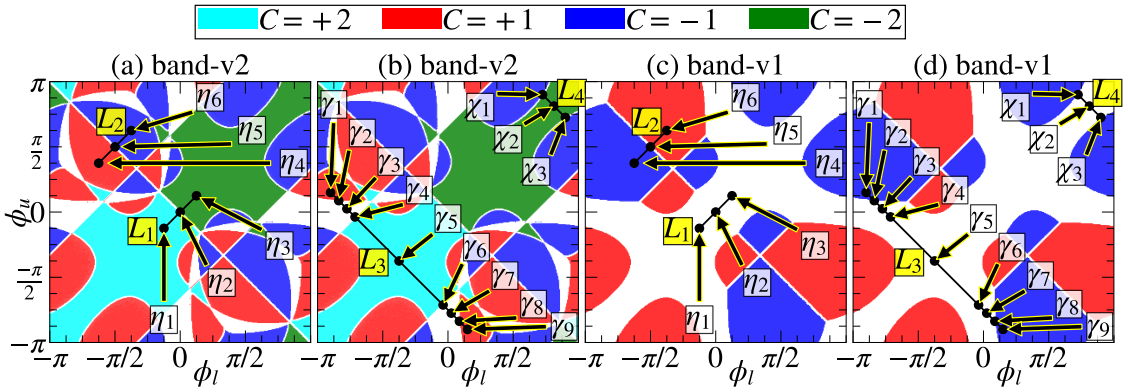

FIG. 4.5: The phase diagrams corresponding to band-v2 are shown in (a) and (b), and those for band-v1 are presented in (c) and (d). In (a) and (c), the η points are used and shown along the L_1 and L_2 lines, whereas the γ and χ points are marked along the L_3 and L_4 lines in both (b) and (d). Along those lines multiple phase transitions occur. For example, along L_3, the Chern number corresponding to band-v2 has values $+1$, 0, $+2$, 0, $+1$ at the points γ_1, γ_3, γ_5, γ_7 and γ_9 respectively. The phase transitions take place at γ_2, γ_4, γ_6 and γ_8, where band-v2 touches either band-v1 or band-c2. The values of $t_\perp$ and t_1 are taken as $0.5t$ and t_1 respectively.

denote $C = -1$ phases. The trivial phases with $C = 0$ are shown by the white regions. It is evident from Fig. 4.4(a) that the areas of the Chern insulating regions are maximum for $t_1 = t$ (Dirac case). An engineering of the band structure, that is, with the increase in the value of t_1, the area of the topological regions (called as the Chern lobes) gradually shrink. We have shown the phase diagram till a certain value, namely, $t_1 = 1.9t$ (see Fig. 4.4(d)), beyond which the topological regions can hardly be seen. When t_1 becomes equal to $2t$, the Chern number (C) vanishes completely for all values of ϕ_l and ϕ_u owing to a gapless scenario that exists between band-c2 and band-v2. Although band-v1 remains separated from the band-v2, the Chern number still vanishes. For $t_1 > 2t$, a gap opens up, however, the Chern numbers continue to be zero, and thus the gap is trivial.

Further, the phase diagrams corresponding to band-v2 (see Figs. 4.4(e)-4.4(h)) demonstrates additional phases with higher Chern numbers ($C = \pm 2$). Such non-trivial phases are denoted by different colors, namely, the cyan and green colors for the $C = +2$ and $C = -2$ phases respectively. The red and blue colors continue to denote $C = +1$ and $C = -1$ phases respectively. Thus, both $C = \pm 2$ and $C = \pm 1$ phases occur at different parameter values in the same phase diagram. Further,

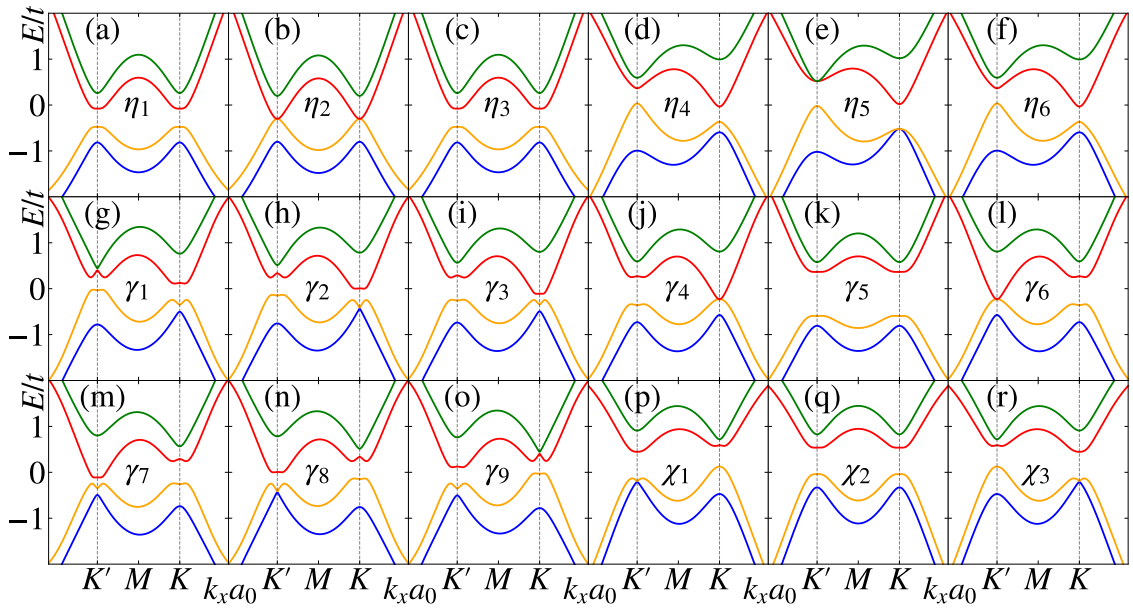

FIG. 4.6: The band structures corresponding to the points η_1-η_6 [shown in Figs. 4.5(a) and 4.5(c)] are depicted in (a)-(f). The spectra for the points γ_1-γ_9 [shown in Figs. 4.5(c) and 4.5(d)] are shown in (g)-(o), and for the points χ_1-χ_3 are presented in (p)-(r). The values of t_1 and $t_\perp$ for all the band structures are kept fixed at t and $0.5t$ respectively.

the topological regions shrink with the increase in t_1, and finally vanish at $t_1 = 2t$, where the gap between the band-v2 and band-c2 vanishes. For $t_1 > 2t$, the gap reopens, but the Chern number remains zero for all values of ϕ_l and ϕ_u. The phase diagrams for band-c1 and band-c2 are identical in shape to those of band-v1 and band-v2 respectively, except the Chern numbers have opposite signs.

In order to visualize the gap closing scenario corresponding to different phase transitions occurring in the phase diagrams, the band structures are presented in Fig. 4.6 for a particular value of t_1 and $t_\perp$, namely, $t_1 = t$ and $t_\perp = 0.5t$. The values of ϕ_l and ϕ_u are such that they lie along the four lines, namely, L_1, L_2, L_3 and L_4 in the phase diagrams depicted in Fig. 4.5, and are denoted by $\eta_i\,(i = 1, \ldots, 6)$, $\gamma_j\,(j = 1, \ldots, 9)$, and $\chi_s\,(s = 1, 2, 3)$. Along L_1, a topological phase transition occur between $C = +2$ and $C = -2$ corresponding to band-v2, while the transition between $C = +1$ and $C = -1$ occur along L_2 for both band-v2 and band-v1. These results have to be understood in conjunction with the corresponding band structures as shown in Figs. 4.6(a)-4.6(c) and 4.6(d)-4.6(f) respectively. The band structures corresponding to η_1 and η_3 points are identical

and the Chern numbers corresponding to band-v2 are $+2$ and -2 respectively [Fig. 4.5(a)]. At η_2, band-v2 and band-c2 touch each other at both the Dirac points [Fig. 4.6(b)], and hence there is a phase transition at η_2. However, band-v1 remains isolated from band-v2 at these η points, and the Chern numbers are zero along L_1 as evident from its phase diagram [Fig. 4.5(c)]. Further, the band structures corresponding to η_4 and η_6 have similar features, however in this case, C has values $+1$ and -1 respectively corresponding to band-v2, while for band-v1, C has the same magnitude, but are of opposite signs. At the phase transition occurring at η_5, band-v2 and band-v1 touch each other at the **K** point in the BZ [Fig. 4.6(e)], and hence for both the bands, a topological phase transition takes place at this point.

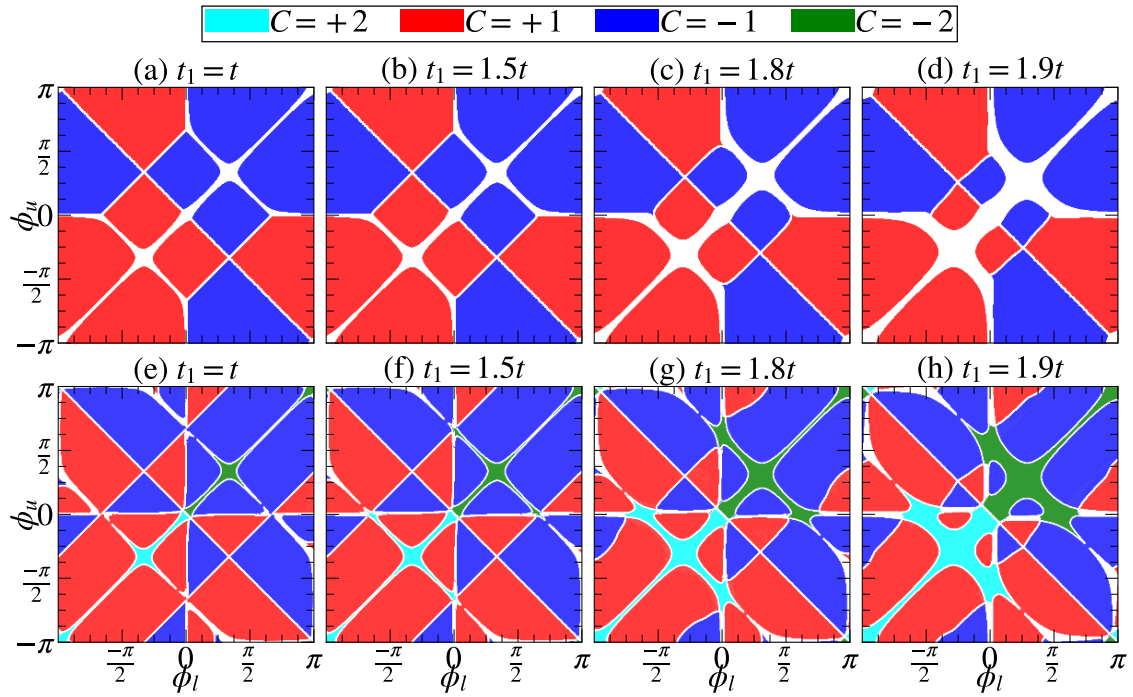

FIG. 4.7: The phase diagrams corresponding to band-v1 are shown in (a)-(d), while those for band-v2 are shown in (e)-(h). The value of $t_\perp$ is kept fixed at $0.1t$. The values of t_1 are such that $t_1 = t$ in (a) and (e), $t_1 = 1.5t$ in (b) and (f), $t_1 = 1.8t$ in (c) and (g), and $t_1 = 1.9t$ in (d) and (h). The white regions denote trivial phases with zero Chern numbers, while the colored regions indicate the non-trivial phases with the non-zero Chern numbers. The values are indicated at the top of the figure.

Further, along L_3, again multiple phase transitions occur [see Figs. 4.5(b) and

4.5(d)], and the corresponding dispersions are shown in Figs. 4.6(g)-4.6(o). At γ_1, band-v2 and band-v1 show $C = +1$ and $C = -1$ respectively which drops to zero at γ_2 and hence the gap between those bands close at the $\mathbf{K}$ point as shown in Fig. 4.6(h). At γ_3, the gap reopens, but the Chern numbers corresponding to these bands remain zero. The gap between band-v2 and band-c2 vanishes at γ_4 where again a phase transition takes place, since along the line connecting γ_4 and γ_6, the Chern number has a value $+2$. The band structure at an intermediate point, namely, γ_5 has been shown in Fig. 4.6(k). Similarly, phase transitions take place at γ_6 and γ_8, where the gaps vanish at the $\mathbf{K}'$ point. At γ_7 and γ_9, C assumes values zero and $+1$ respectively corresponding to band-v2. It should be noted that band-v1 shows vanishing of the Chern number between γ_2 and γ_8 segments [see Fig. 4.5(d)] and hence it never touches band-v2 which results in absence of any phase transition.

We now show the phase transitions between $C = -2$ and $C = -1$ phase along L_4. The corresponding band structures are shown in Figs. 4.6(p)-4.6(r). At χ_2, band-v2 and band-v1 remain isolated from each other, however, they possess Chern numbers $C = -2$ and $C = 0$ respectively. At χ_1 and χ_3, these two bands touch each other at the $\mathbf{K}'$ and $\mathbf{K}$ points in the BZ respectively, where topological phase transitions take place. Beyond χ_1 and χ_3, the gap reopens and both bands possess non-trivial phases with $C = -1$.

Further, along the $\phi_u = -\phi_l$ line, a semi-metallic phase exists for all the bands. In the vicinity of $\phi_u = \phi_l$, only the phase diagrams of band-v1 show trivial regions with $C = 0$, however, those for band-v2 demonstrate non-trivial phases either with $C = +2$ or $C = -2$.

Moreover, in order to see the effects of the interlayer hopping, $t_\perp$ on the topological phases, we have shown the phase diagrams corresponding to band-v1 [Figs. 4.7(a)-4.7(d)] and band-v2 [Figs. 4.7(e)-4.7(h)] for a different value of $t_\perp$ (in addition to $t_\perp = 0.5t$). It is evident that the areas of Chern insulating regions are enhanced corresponding to a lower values of $t_\perp = 0.1t$. Also, the shapes of the topological regions are different from those for the $t_\perp = 0.5t$ case. Further, the areas of $C = \pm 2$ regions in the phase diagram corresponding to band-v2 are mostly spanned by $C = \pm 1$ regions. However, the feature that remains unaltered is the

trivial phase along $\phi_u = \pm\phi_l$ lines for band-v1 and $\phi_u = \phi_l$ line for band-v2. For both $t_\perp = 0.5t$ and $t_\perp = 0.1t$, the Chern insulating regions gradually shrink with the increase in the value of t_1 and finally vanish at the semi-Dirac limit, namely, $t_1 = 2t$. For $t_1 > 2t$, the system remains a trivial insulator.

4.4 Edge states

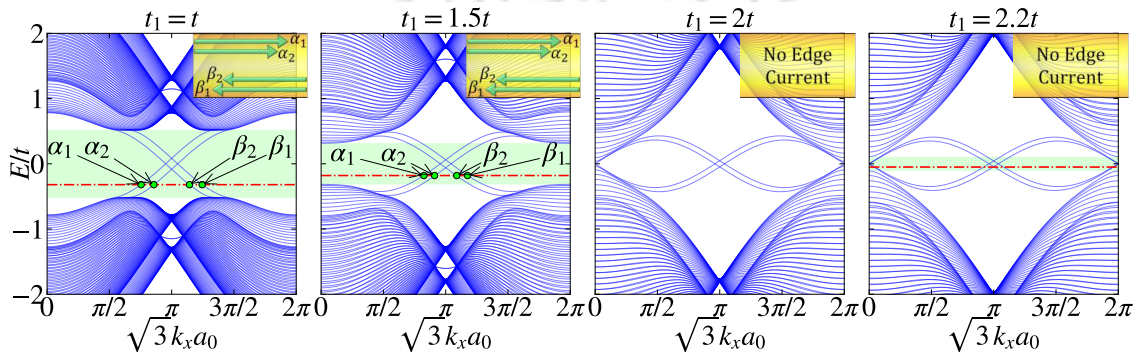

FIG. 4.8: The edge state spectra are shown for (a) $t_1 = t$, (b) $t_1 = 1.5t$, (c) $t_1 = 2t$, and (d) $t_1 = 2.2t$. The green shaded regions represent the bulk gap in (a), (b) and (d) [no bulk gap in (c)]. The Fermi levels (E_F) are denoted by the red dashed lines, which are shown to be present in the bulk gap. E_F intersects the edge modes at the points denoted by the green dots as shown in (a) and (b). For these, the edge currents are shown by the green arrows in the yellow panels located at the top right corner, which represent parts of the semi-infinite ribbon.

To show the existence (and their vanishing) of the edge modes, in this section, we show the band structure of the system for semi-infinite nanoribbon. The ribbon has a finite width along the y-direction, while it is infinite along the x-direction [70, 185]. Further, we label the sites along the y-direction as A_1^l, B_1^l, A_2^l, B_2^l, ... A_N^l, B_N^l, A_1^u, B_1^u, A_2^u, B_2^u, ... A_N^u, B_N^u. Since, the periodicity along the x-direction remains preserved, we can Fourier transform the operators along that direction. This results in a set of four coupled equations as shown below.

$$\begin{aligned} E_k a^u_{k,n} = &\left[t\left\{1 + e^{(-1)^n ik}\right\} b^u_{k,n} + t_1 b^u_{k,n-1}\right] \\ &- 2t_2\left[\cos(k+\phi) a^u_{k,n} + e^{(-1)^n \frac{ik}{2}} \cos\left(\frac{k}{2} - \phi\right)\left\{a^u_{k,n-1} + a^u_{k,n+1}\right\}\right] \end{aligned} \quad \text{4.9}$$

$$E_k b^u_{k,n} = \left[t\left\{1+e^{(-1)^{n+1}ik}\right\}a^u_{k,n} + t_1 a^u_{k,n+1}\right] - 2t_2\left[e^{(-1)^{n+1}\frac{ik}{2}}\cos\left(\frac{k}{2}+\phi\right)\right. \tag{4.10}$$
$$\left.\times\{a^u_{k,n-1}+a^u_{k,n+1}\}+\cos(k-\phi)b^u_{k,n}\right] + t_\perp\left[\xi_1 e^{-ik}+\xi_2\right]a^l_n$$

$$E_k a^l_{k,n} = \left[t\left\{1+e^{(-1)^{n}ik}\right\}b^l_{k,n} + t_1 b^l_{k,n-1}\right] - 2t_2\left[e^{(-1)^{n}\frac{ik}{2}}\cos\left(\frac{k}{2}-\phi\right)\right. \tag{4.11}$$
$$\left.\times\{a^l_{k,n-1}+a^l_{k,n+1}\}\cos(k+\phi)a^l_{k,n}+\right] + t_\perp\left[\xi_1 e^{ik}+\xi_2\right]b^u_n$$

$$E_k b^l_{k,n} = \left[t\left\{1+e^{(-1)^{n+1}ik}\right\}a^l_{k,n} + t_1 a^l_{k,n+1}\right] \tag{4.12}$$
$$-2t_2\left[\cos(k-\phi)b^l_{k,n} + e^{(-1)^{n+1}\frac{ik}{2}}\cos\left(\frac{k}{2}+\phi\right)\{a^l_{k,n-1}+a^l_{k,n+1}\}\right]$$

where $a^{l,u}_{k,n}$ and $b^{l,u}_{k,n}$ are the amplitudes of the wave functions corresponding to the sublattices A and B respectively. To remind ourselves, the superscripts l and u refer to lower and upper layers respectively. Here $k = \sqrt{3}k_x a_0$ is the dimensionless momentum and n denotes the site index which assumes integer values in the range $[1 : N]$ with N being the total number of unit cells along the y-direction. We have chosen $N = 128$, resulting in a width of $79\sqrt{3}a_0$. In Eqs. 4.10 and 4.11, ξ_1 and ξ_2 denote quantities that depend on the site index n and are defined as,

$$\xi_1 = [1-(-1)^n]/2 \;\text{ and }\; \xi_2 = [1+(-1)^n]/2$$

respectively.

By solving Eqs. 4.9, 4.10, 4.11, and 4.12, we obtain the band structure of the nanoribbon for various values of t_1 as presented in Fig. 4.8. It can be noticed that a pair of edge modes from the valence bands (band-v2) traverse the Fermi level, E_F (shown via the red dashed line) and merge with the conduction bands (band-c2), and another pair crosses the Fermi level in the opposite direction. Such crossing of the edge modes leads to a quantized Hall conductivity should the Fermi level lie in the bulk gap. E_F intersects the edge modes [see Figs. 4.8(a) and 4.8(b)] at four points (marked by the green dots), whose corresponding edge currents are shown by the green arrows in the yellow panels located at the top right corner of the plots. The yellow panels represent a part of the semi-infinite ribbon. Since the velocity of electrons is proportional to the slope of the band structure, that is, $\partial E/\partial k$, there exists a pair of edge currents at each edge that moves in the same

direction. However, such pairs of currents propagate in opposite directions at the two edges of the ribbon. Hence, these modes are called chiral edge modes.

It should be noted that because of a pair of chiral edge modes, we should obtain the Hall conductivity quantized with a plateau at $2e^2/h$, with the factor '2' arising due to doubling of the number of chiral edge modes [189]. Such chiral edge modes exist as long as the value of t_1 remains less than $2t$. Since the bulk gap vanishes at $t_1 = 2t$ [see Fig. 4.8(c)], the edge current vanishes. For $t_1 > 2t$, the edge modes get detached from the bulk bands as shown in Fig. 4.8(d) for $t_1 = 2.2t$, thereby resulting in a zero edge current. These results are consistent with the corresponding Chern numbers obtained in the phase diagram. For example, we observe the non-zero edge currents for $t_1 < 2t$ and the corresponding Chern number is found to be $C = |2|$. For $t_1 > 2t$, the Chern numbers vanish, and so do the edge currents. The figures presented here are for $t_\perp = 0.5t$. For $t_\perp = 0.1t$, we observe similar features in the spectrum, except that the bulk gaps are reduced. We have skipped the discussion of the latter for brevity.

4.5 Hall conductivity

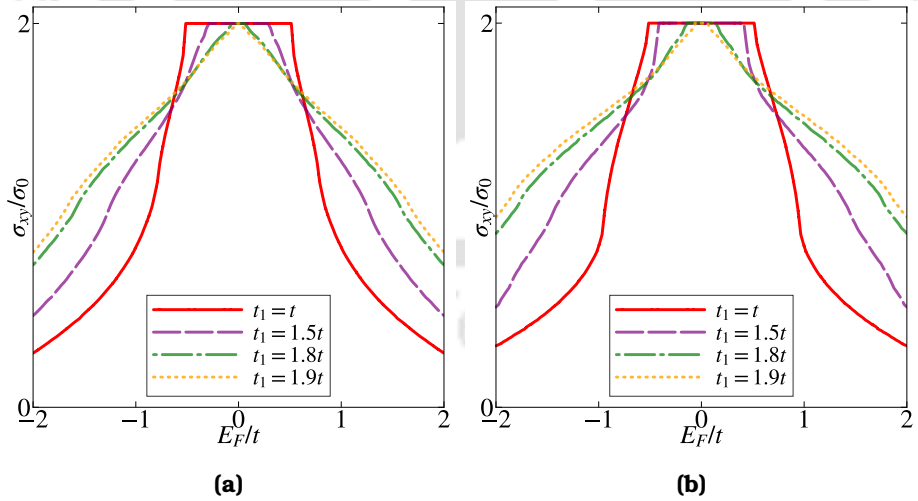

FIG. 4.9: The anomalous Hall conductivities are shown as a function of E_F for various values of t_1 in (a) and (b) for $t_\perp = 0.5t$ and $t_\perp = 0.1t$ respectively. The plateau width decreases as t_1 deviates from t.

Here, we calculate the anomalous Hall conductivity as a function of the Fermi

energy E_F using Eq. 1.39 at zero temperature. The spectrum for various values of t_1 is shown in Fig. 4.9.

As can be seen from Fig. 4.9(a), that when the Fermi energy, E_F lies in the bulk gap, σ_{xy} becomes quantized at a value $2\sigma_0$. The width of the plateau is equal to the width of the bulk gap in the dispersion spectrum of Fig. 4.2. As soon as E_F intersects the bands (either both the conduction or both the valence bands), σ_{xy} starts to decrease since the integral is performed over the occupied states. This also results in diminishing of the plateau width with increase in the value of t_1. This happens because the energy gap between the band-c2 and band-v2 shrinks. The plateau and the Hall conductivity vanish completely at $t_1 = 2t$, where the spectrum becomes gapless. For the hopping asymmetry engineered beyond the semi-Dirac limit, that is, $t_1 > 2t$, the bands become gapped again, however, the Hall conductivity remains zero. These results are consistent with their corresponding information coming from the Chern numbers. The Hall plateaus are observed as long as the system remains a Chern insulator, that is, for $t_1 < 2t$. Further, the factor '2' in $2\sigma_0$ denotes the value of Chern number (and also the edge modes) which vanishes for $t_1 > 2t$.

We have also presented the Hall conductivity for a smaller value of $t_\perp$, namely, $t_\perp = 0.1t$ in Fig. 4.9(b). In this case, the plateau widths corresponding to different values of t_1 are larger as compared to that for the $t_\perp = 0.5t$ case, since the corresponding band gaps are enhanced as shown in Fig. 4.3. However, similar to the previous case, the plateau width decreases with the increase of t_1, which finally vanishes at $t_1 = 2t$ and beyond. Thus, a topological phase transition takes place across the gap closing point at the semi-Dirac limit, namely, $t_1 = 2t$.

4.6 Summary

We have investigated the topological properties for a band engineered bilayer Haldane. By tuning one of the three NN hopping amplitudes, the band extrema, which were located at the $\mathbf{K}$ and $\mathbf{K}'$ points for the Dirac case, migrate towards each other and finally merge at an intermediate $\mathbf{M}$ point in the BZ in the semi-Dirac limit, that is, at $t_1 = 2t$. We have calculated the Chern numbers for various

values of t_1 and plotted them in the ϕ_u-ϕ_l plane which demonstrates that the higher Chern numbers ($C = \pm 2$) are associated only with band-v2. However, the Chern numbers corresponding to both bands vanish, that is, there are topological phase transitions, where the Chern numbers discontinuously change from $C = \pm 2$ to $C = 0$ and $C = \pm 1$ to $C = 0$, across the semi-Dirac point $t_1 = 2t$. Also, there are multiple phase transitions in the phase diagram, such as, $+2 \rightarrow -2$, $+1 \rightarrow -1$, $\pm 2 \rightarrow \pm 1$ and $\pm 2 \rightarrow 0 \rightarrow 1$. These phase transitions are confirmed by the opening and closing of the energy gaps (semi-metallic phase) in the dispersion spectrum. Further, we have also computed the band structure of a nanoribbon, where we observe a pair of chiral edge modes along the edges of the ribbon exist as long as t_1 remains lesser than $2t$. Also for the anomalous Hall conductivity, the width of the quantized plateau at $2\sigma_0$ gradually decreases with increase in t_1, which finally vanishes at $t_1 = 2t$. Thus, a bilayer Haldane model, similar to its monolayer analogue, exhibits a topological phase transition at the semi-Dirac point. However, here we have larger Chern number values and doubling of the edge modes at the edges of the bilayer nanoribbon. Further, the phase transitions are supported by the vanishing Chern number, chiral edge modes, and the anomalous Hall conductivity.

Chapter 5

Band-Deformed Dice Lattice: Role of Flat Bands and Topological Phase Transitions

The previous chapters include description of topological phases for two-band systems, where the Chern number assumes values ± 1. In this chapter wish to extend the exploration of such non-trivial phases in multi-band system. The system we have considered here is the dice lattice which has the structure of a honeycomb lattice with an additional lattice point at the centre of the hexagon. This point is connected to either A or B sublattice and thus belongs to a third sublattice, namely, a C sublattice [93]. Thus, the unit cell contains three sublattices, namely, A, B and C. The band structure consists of a zero energy flat band that resides between the conduction (upper) and the valence (lower) bands, and they have degeneracies at the Dirac points ($\mathbf{K}$ and $\mathbf{K}'$) in the sense that all the bands touch each other at these points in the BZ.

Further, to induce non-trivial phases in the system, the TRS breaking complex NNN hopping is included in the dice lattice whose topological and the transport properties may be predictable from the band structure perspective (similarity with that of the honeycomb lattice). However, owing to an additional flat band at the Fermi level, the topological properties would be more interesting and are characterized by larger values of Chern number, namely, $C = \pm 2$. Interestingly, the electrons in the flat band are immobile, and hence their contribution to the transport phenomena may not yield interesting results. However our studies will have

larger impact if somehow the flat band is rendered dispersive, which will enable it to contribute to the transport phenomenon and may have important consequences on the topological properties. We simulate the evolution of the topological properties of a band-engineered dice lattice induced by an anisotropic hopping energy between selected nearest neighbour bonds.

As a first case (we shall call this as case-I later), the hopping anisotropy is introduced via tuning the nearest nighbour (NN) hopping amplitudes between the A-B (say, t_1) and B-C (say, t') sublattices identically along a given direction, while those along the rest of the NN directions (t) are kept unaltered (see Fig. 5.1). Such an anisotropic hopping causes the band extrema from the Dirac points to move closer to each other, and they eventually merge at an intermediate M point, in a scenario quite similar to us. The spectral gaps and the topological properties vanish at a special value of the hopping t_1, namely, $t_1 = t' = 2t$. In the absence of the NNN hopping, the band dispersion for this particular value of t_1 and t' is quadratic along the k_x direction and linear along the k_y direction, resulting in the so-called semi-Dirac dispersion. However, the presence of NNN hopping makes the spectrum anisotropic linear, that is, linear along both the directions, but the electrons have unequal velocities. This phenomenon is similar to the case for graphene, where a topological phase transition takes place at the gap closing semi-Dirac limit [193, 202], except that in the dice lattice we have an additional zero energy flat band. Thus, disappearance of a band gap is more involved here as we shall see below.

An second option to induce hopping anisotropy is via '*selectively*' tuning the hopping t_1 between the A and B sublattices, while keeping t' between the B and C sublattices unaltered. To distinguish it from the case above, we call it case-II. Such a selective hopping anisotropy leads to distinct effects compared to the above case, where the band extrema do not migrate, however the flat band gets dispersive, which eventually alters the gap between the conduction (or valence) and the flat band. Moreover, the deformation of the flat band, which no longer remains flat, should enable it to contribute to the transport properties. Finally, the spectral gap vanishes at certain value of the anisotropy, intermediate to the Dirac and the semi-Dirac limits, namely, $t_1 = 1.67t$ which is different from case-

I (that is, $t_1 = t' = 2t$) and depends on the value of NNN hopping amplitude t_2. The latter is also a discernible feature of this system, since the value of t_2 did not play a role earlier and any non-zero t_2 induces topological properties. Such vanishing of the band gap again leads to the vanishing of the topological properties similar to the case above. However, the Chern insulating regions in the phase diagram and the anomalous Hall conductivities have differences in these two cases. Expectedly, we see that the effects of the flat band being dispersive lead to observable consequences in the behaviour of the anomalous Hall conductivity.

Possible experimental scenarios in inducing hopping anisotropy, at least for case-I can be provided as follows. The hopping energies t_1 and t' can be altered simultaneously by applying an uniaxial strain to the system which changes the bond length along the direction of application of the strain. Thus, the hopping energies among the A-B and B-C sublattices will be modified simultaneously. Such applications of uniaxial strain in the honeycomb lattice structure, such as, Si_2O yields a semi-Dirac band structure [52]. For the sake of completeness, we have applied both types of anisotropy and compare between the corresponding properties for a dice lattice. Case-II involves selective control of the hopping amplitudes (see Fig. 5.1) and is included for comparison owing to the interesting consequences detailed above (and also later in section 5.3).

This chapter is organized in the following way. In Sec. 5.1, we present the Hamiltonian of the system for the two cases (case-I and case-II) and the energy dispersions are plotted for a few different values of the anisotropy parameters in Sec. 5.2. Sec. 5.3 deals with the topological properties among which Sec. 5.3.1 shows the phase diagrams corresponding to different strengths of the anisotropic hopping. Further, the presence (or absence) of a pair of edge modes of a nanoribbon for various parameters are shown in Sec. 5.3.2. Finally, we present numerical computation of the anomalous Hall conductivity in Sec. 5.3.3 corresponding to both the case-I and case-II. We finally conclude with a brief summary of the results obtained in Sec. 5.4.

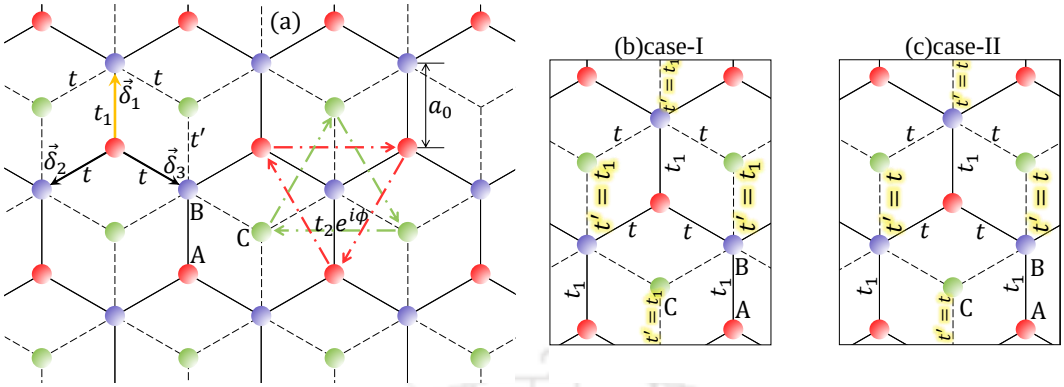

FIG. 5.1: A dice lattice is shown in (a) where the red, blue and the green circles represent the sublattices A, B and C respectively. The NN hopping strength between A and B sublattices along the $\boldsymbol{\delta}_1$ direction (shown via the yellow arrow) is t_1, while it is t' between B and C sublattices along the same direction. The NNN hopping is $t_2 e^{i\phi}$ ($t_2 e^{-i\phi}$) for the clockwise (anti-clockwise) direction. $\boldsymbol{\delta}_i$ and a_0 represent the NN vectors and lattice constant respectively. In (b) and (c), the values of the NN hopping amplitude, namely, t' are shown corresponding to case-I and case-II respectively.

5.1 The Hamiltonian

A tight-binding Hamiltonian on a dice lattice can be written as follows,

$$H = \left[\sum_{\langle ij\rangle} t_{ij} c_i^\dagger c_j + \sum_{\langle\langle ik\rangle\rangle} e^{i\phi_{ik}} c_i^\dagger c_k + \text{h.c.}\right] + \sum_i \Delta_i c_i^\dagger c_i \qquad 5.1$$

The first term is the nearest neighbour (NN) hopping, where the hopping $t_{ij} = t_1$ when i connects the site j along the $\boldsymbol{\delta}_1 = a_0(0,1)$ direction, while it is t along the $\boldsymbol{\delta}_2 = a_0(\sqrt{3}/2, -1/2)$ and $\boldsymbol{\delta}_3 = a_0(\sqrt{3}/2, -1/2)$ directions shown in Fig. 5.1. Such values of t_{ij} are restricted among the A and B sublattices. Further, the NN hoppings between the B and C sublattices along the $\boldsymbol{\delta}_1$ direction is t', and is t in the $\boldsymbol{\delta}_{2,3}$ directions. As elaborated earlier, we have considered two cases. In case-I we vary both t_1 and t' in the range $[t : 2t]$, while is the second case, t' is kept fixed at t, and t_1 is varied in the range $[t : 1.8t]$. This rather unfamiliar value, namely, $1.8t$ originates from the vanishing of spectral gap occurring at $t_1 = 1.67t$. The second term in Eq. 5.1 represents the complex next nearest neighbour hopping (NNN) with an amplitude t_2 and a phase ϕ_{ik}, where ϕ_{ik} is positive (negative) when an electron hops in the clockwise (anti-clockwise) direction. The third term denotes the onsite energy term, that assumes values $\pm\Delta$ at the sites that belong to A and

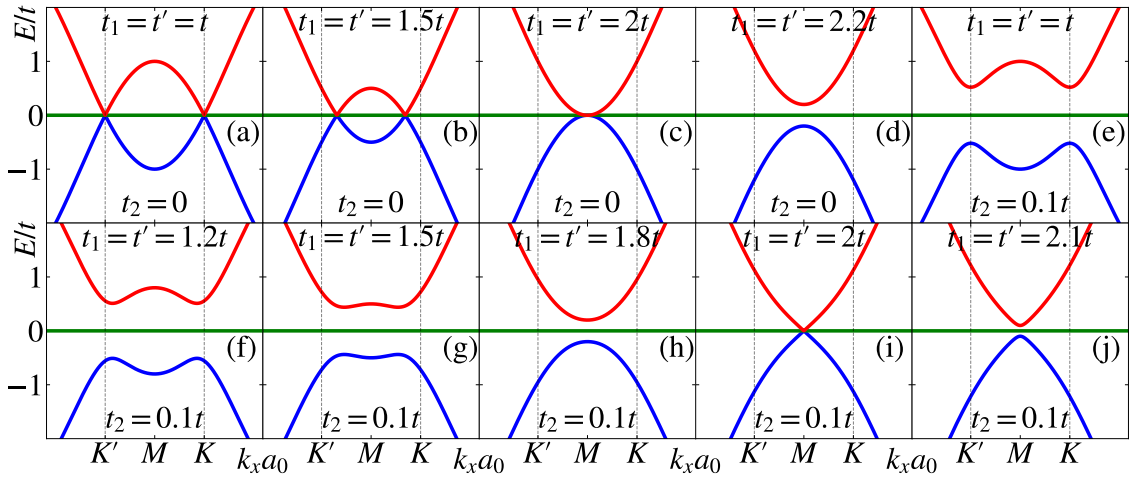

FIG. 5.2: The band structure of the system in absence of t_2 ($t_2 = 0$) is shown along the k_x-axis (at $k_y a_0 = 2\pi/3$) for (a) $t_1 = t' = t$, (b) $t_1 = t' = 1.5t$, (c) $t_1 = t' = 2t$, and (d) $t_1 = t' = 2.2t$. Similarly, the dispersion in presence of t_2 ($t_2 = 0.1t$) is depicted for (e) $t_1 = t' = t$, (f) $t_1 = t' = 1.2t$, (g) $t_1 = t' = 1.5t$, (h) $t_1 = t' = 1.8t$, (i) $t_1 = t' = 2t$, and (j) $t_1 = t' = 2.1t$. In the figures, k_x is rendered dimensionless by multiplying with lattice constant a_0.

C sublattices respectively.

The Fourier transformed Hamiltonian can be written as,

$$H(\mathbf{k}) = \begin{pmatrix} h_z^+(\mathbf{k}) & h(\mathbf{k}, t_1) & 0 \\ h^*(\mathbf{k}, t_1) & 0 & h(\mathbf{k}, t') \\ 0 & h^*(\mathbf{k}, t') & h_z^-(\mathbf{k}) \end{pmatrix} \tag{5.2}$$

where $h(\mathbf{k}, \tilde{t}) = h_x(\mathbf{k}, \tilde{t}) - i h_y(\mathbf{k}, \tilde{t})$, where $\tilde{t}$ is either t_1 or t'. The elements $h_z^{\pm}$ are defined as, $h_z^+(\mathbf{k}) = h_0(\mathbf{k}) \pm h_z(\mathbf{k})$. The expressions for the h_is can be written as,

$$h_x(\mathbf{k}, \tilde{t}) = \left\{ \tilde{t} \cos k_y + 2t \cos \frac{k_y}{2} \cos \frac{\sqrt{3} k_x}{2} \right\}, \tag{5.3}$$

$$h_y(\mathbf{k}, \tilde{t}) = \left\{ -\tilde{t} \sin k_y + 2t \sin \frac{k_y}{2} \cos \frac{\sqrt{3} k_x}{2} \right\}, \tag{5.4}$$

$$h_z(\mathbf{k}) = \Delta - 2t_2 \sin\phi \left\{ 2\sin\frac{\sqrt{3}k_x}{2}\cos\frac{3k_y}{2} - \sin\sqrt{3}k_x \right\} \quad \text{5.5}$$

and,

$$h_0(\mathbf{k}) = 2t_2 \cos\phi \left\{ 2\cos\frac{\sqrt{3}k_x}{2}\cos\frac{3k_y}{2} + \cos\sqrt{3}k_x \right\} \quad \text{5.6}$$

To make discussion self-contained, we have included the calculation of the electronic dispersion in Appendix A.1. The Haldane flux is kept constant at $\pi/2$ to ensure that the NNN hopping amplitudes are purely imaginary. Furthermore, we have considered $\Delta = 0$, except for the computation of the phase diagram in Sec. 5.3.1.

5.2 Spectral properties

The electronic energy spectra of the system, via varying both t_1 and t', have been obtained via numerical diagonalization of Eq. 5.2 and are shown in Fig. 5.2. Three bands appear in the spectrum, which we term as the conduction band (shown in red), flat band (in green) and valence band (in blue). In absence of the NNN hopping, there is no spectral gap (Figs. 5.2(a)-5.2(d)) in the BZ except for $t_1 > 2t$. As we turn on the NNN hopping, spectral gaps (of the same magnitude) open up at the Dirac points, that is, at $\mathbf{K}\,(2\pi/3\sqrt{3}a_0, 2\pi/3a_0)$ and $\mathbf{K}'\,(-2\pi/3\sqrt{3}a_0, 2\pi/3a_0)$ points (Fig. 5.2(e)). Now if we increase t_1 and t', the band extrema at the $\mathbf{K}$ and the $\mathbf{K}'$ points migrate towards each other which results in diminishing of the band gap. At a special value of the hopping amplitude, namely, $t_1 = t' = 2t$, the band gap vanishes at $\mathbf{M}\,(2\pi/3a_0, 0)$ point even in the presence of the Haldane term, t_2 (that is, TRS remains broken) (Fig. 5.2(i)). As both t_1 and t' are increased beyond value $2t$ (t denotes NN hopping), a spectral gap opens up again at the $\mathbf{M}$ point and the band structure henceforth remains gapped for all values of $t_1 > 2t$ and $t' > 2t$. It should be noted that without the Haldane's NNN hopping, the band structure of the dice lattice (Figs. 5.2(a)-5.2(d)) demonstrates very similar properties with that of graphene, except that there is no flat band for the latter [40, 41]. At $t_1 = t' = 2t$, the spectrum resembles a semi-Dirac dispersion, that is, linear along

k_y, and quadratic along the k_x direction. The presence of t_2 makes the dispersion anisotropic linear, that is linear along both the directions, however the electrons move with different velocities (see Fig. 5.2(i)). Further, the spectra for other values of t_1 (for $t_2 \neq 0$) demonstrate similar features as that obtained for graphene [193].

Now we discuss the spectral features corresponding to case-II where t' is fixed at t, while t_1 is varied. The corresponding plots are depicted in Fig. 5.3 for both $t_2 = 0$ (5.3(a) - 5.3(d)) and $t_2 \neq 0$ (5.3(e) - 5.3(j)). For $t_2 = 0$, one can observe a spectral gap, which scales with t_1, however the flat band continues to remain flat. As t_2 is turned on, the flat band becomes dispersive for $t_1 \neq t$, and the spectral gap decreases. Hence, we can no longer call it flat band and we refer to it from now on as the middle band. It should be noted that the conduction band minimum remains fixed at the $\mathbf{K}$ point, while the same near the $\mathbf{K}'$ point is displaced along the positive k_x-direction. A similar scenario occurs in the case of the valence band. In fact the reverse occurs, that is, the valence band maximum at $\mathbf{K}'$ point remains constant, while that at $\mathbf{K}$ shifts. Finally the gap vanishes completely at a specific value of t_1, namely $t_1 \simeq 1.67t$. Beyond this value, the gap reopens. Thus the gap closing or the so called '*semi-Dirac*' limit occurs at a much lower value compared to standard $t_1 = 2t$.

Another important aspect of keeping t' unchanged ($t' = t$) is that the closing of the energy gap depends on the value of t_2. The spectrum shown in Figs. 5.3(e) - 5.3(j) is for $t_2 = 0.1t$ for which the gap closes at $t_1 = 1.67t$. However, if t_2 is increases (decreases) the gap closes at higher (lower) values of t_1. Further, as opposed to all the three bands (three fold degeneracy) touching together at the $\mathbf{M}$ point in case-I, here we observe the two bands (conduction and middle bands) to be touching each other above the Fermi level, while the other two (valence and middle bands) touch below the Fermi level (see Fig. 5.3(i)).

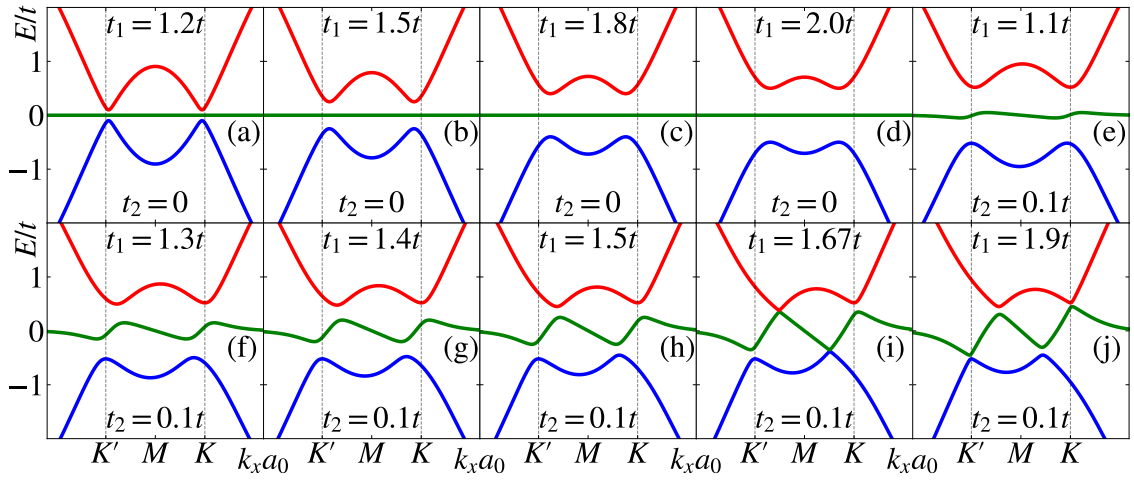

FIG. 5.3: The band structures corresponding to case-II are shown along the dimensionless k_x-axis (at $k_y a_0 = 2\pi/3$) for (a) $t_1 = 1.2t$, (b) $t_1 = 1.5t$, (c) $t_1 = 1.8t$, and (d) $t_1 = 2t$, without a Haldane term ($t_2 = 0$). The same for $t_2 \neq 0$ are shown in (e)-(j) for $t_1 = 1.1t$, $t_1 = 1.3t$, $t_1 = 1.4t$, $t_1 = 1.5t$, $t_1 = 1.67t$, and $t_1 = 1.9t$ respectively. The values of t', ϕ and Δ are taken as t, $\pi/2$ and zero respectively.

5.3 Topological properties

5.3.1 Chern number

In this section, we obtain the phase diagram of the system by calculating the Chern number numerically. Since the NNN hopping term breaks the TRS, we should get non-zero values of Chern number. Moreover, non-vanishing onsite energies, (Δ) can open or close energy gaps at the Dirac points and play an essential role in inducing a topological phase transition. The Chern number (C) of the system have been calculated using the relation in Eq. 1.21 as a function of Δ and ϕ. In Fig. 5.4, we show the Chern number phase diagram corresponding to case-I. As can be noticed, the green and the blue regions in each figure represent the topological phases of the system with Chern numbers $C = +2$ and -2 respectively, while the white region denotes trivial phase with zero Chern number ($C = 0$). Also, we have shown the boundaries separating the topological and the trivial phases corresponding to the original Haldane model for graphene by the black sinusoidal curve. Corresponding to $t_1 = t' = t$, that is, for the familiar dice lattice we get a maximum area of Chern insulating lobes (Fig. 5.4(a)). However,

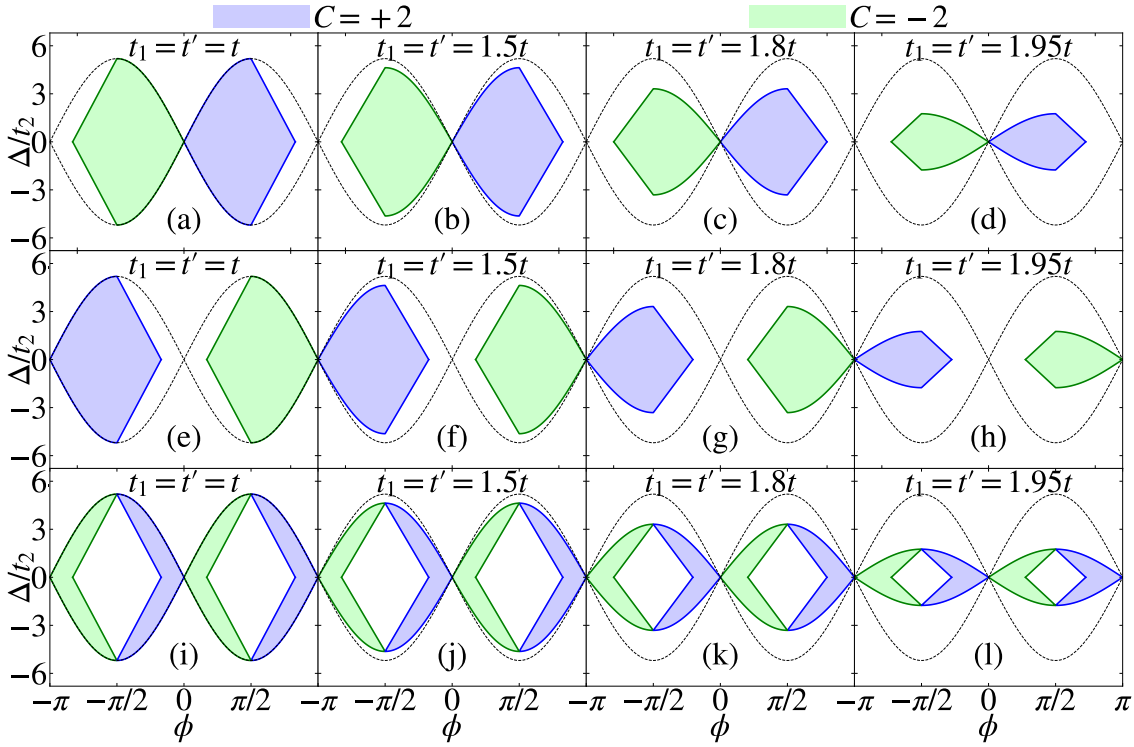

FIG. 5.4: The phase diagrams are shown for $t_1 = t' = t$ in (a), (e) and (i), $t_1 = t' = 1.5t$ in (b), (f) and (j), $t_1 = t' = 1.8t$ in (c), (g) and (k), $t_1 = t' = 1.95t$ in (d), (h) and (l). These phase diagrams are presented corresponding to the valence, conduction and flat bands in (a)-(d), (e)-(h) and (i)-(l) respectively. The non-zero Chern numbers corresponding to blue and green regions have values $+2$ and -2 respectively (indicated above the figures), while the white regions represent vanishing Chern number.

the Chern insulating (topological) regions are smaller than those for the original Haldane model. The phase boundary is sinusoidal for $0 \leq |\phi| \leq \pi/2$ and linear for $|\phi| > \pi/2$. Further, with the increase in the value of t_1 and t' (Figs. 5.4(b)-5.4(d)), the area of the Chern insulating region gradually decreases, but the phase boundary follows the pattern corresponding to that of $t_1 = t' = t$. Finally, the Chern number vanishes completely at the semi-Dirac limit, that is, $t_1 = t' = 2t$. In this limit, for any non-zero value of Δ, there is always a gap in the band structure, however $|C|$ remains zero. If the values of t_1 and t' increases beyond $2t$, the spectral gap remains trivial ($C = 0$) for all values of Δ.

The phase diagrams corresponding to the conduction bands are presented in Figs. 5.4(e)-5.4(h). It is evident that they are similar to that of the valence band except that the Chern insulating regions move away symmetrically from $\phi = 0$

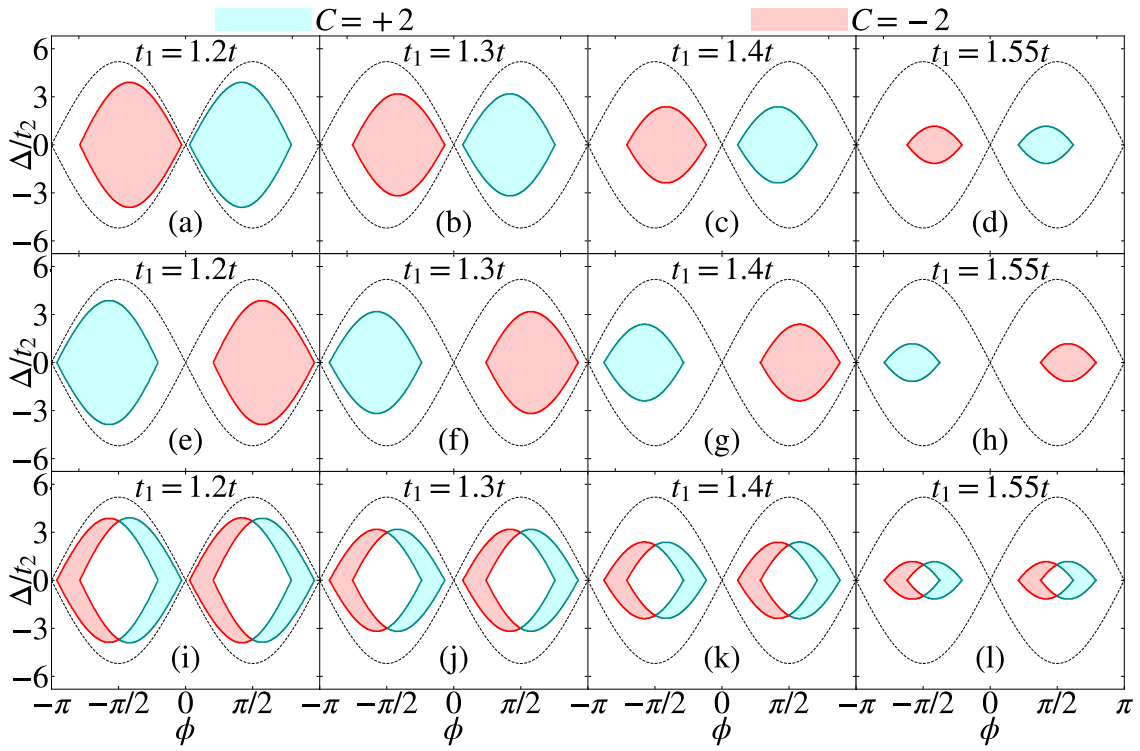

FIG. 5.5: The phase diagrams are shown for $t_1 = 1.2t$ in (a), (e) and (i), $t_1 = 1.3t$ in (b), (f) and (j), $t_1 = 1.4t$ in (c), (g) and (k), $t_1 = 1.55t$ in (d), (h) and (l). These phase diagrams are presented corresponding to the valence, conduction and the middle bands in (a)-(d), (e)-(h) and (i)-(l) respectively. The value of t' and t_2 are taken as t and $0.1t$ respectively. The non-zero Chern numbers corresponding to cyan and red regions have values $+2$ and -2 respectively (indicated above the figures), while the white regions represent vanishing Chern number.

with these having opposite signs for the Chern number, C. In Figs. 5.4(i)-5.4(l), the phase diagrams corresponding to the flat band are depicted. It is obvious that the topological regions are away from $\phi = \pi/2$ and both $C = +2$ and $C = -2$ are observed in the $\pi > |\phi| > 0$ regime. Further the combined phase diagrams for the conduction, middle and the valence bands totally fill up the region under the sinusoidal curves that correspond to the band deformed two-band Haldane model [193]. Hence the total Chern number summed over all bands vanishes. Also we get higher Chern numbers, namely, $|C| = 2$ instead of $|C| = 1$, along with each of the Chern lobes no longer being symmetric (and sinusoidal).

The scenario changes for case-II, when we retain $t' = t$ and selectively vary t_1 as shown in Fig. 5.5. In this case the Chern insulating phases are denoted

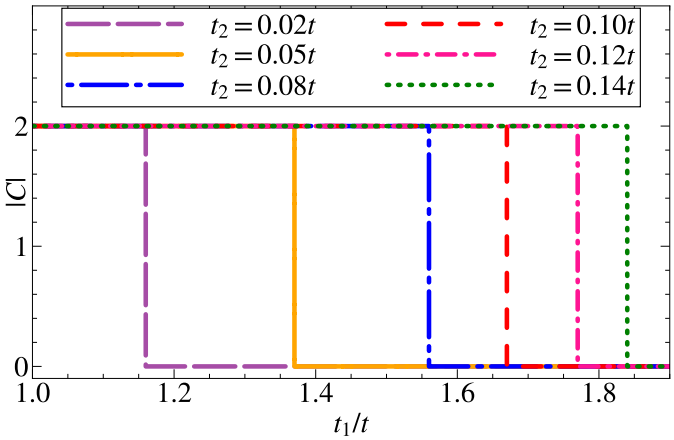

FIG. 5.6: The variation of Chern number as a function of the NN hopping amplitude t_1/t is shown for various values of t_2, which are indicated in panel above the curves.

by different colours, namely, cyan for $C = 2$ and red for $C = -2$ phases. It can be noticed that the Chern insulating regions are shifted away from $\phi = 0$ corresponding to the valence band (Figs. 5.5(a)-5.5(d)), while it gets shifted away from $|\phi| = \pi$ corresponding to the conduction band (Figs. 5.5(e)-5.5(h)). It should be noted that when $t_1 \neq t$, the Chern number corresponding to the valence band becomes zero for $|\phi| \neq 0$ along the $\Delta = 0$ line, since the valence band touches the dispersive flat band at these values of ϕ. As a result, the topological lobes for $\phi > 0$ and $\phi < 0$ regions are separated by a trivial region in the vicinity of $\phi = 0$. Also the separation increases with increase in the value of t_1. A similar scenario occurs for the conduction band, but the Chern lobes are separated by a trivial region in the vicinity of $\phi = \pm\pi$.

Further, the Chern lobes are sinusoidal in shape and thus are distinct from those in case-I. However as earlier, the Chern insulating regions gradually shrink with increase in t_1 and it eventually vanishes completely at the gap closing point $t_1 = 1.67t$. For any non-zero value of Δ, the spectral gap is always trivial for $t_1 = 1.67t$. For $t_1 > 1.67t$, the gap reopens for $\Delta = 0$, however the Chern number vanishes. Thus we observe a topological phase transition at the gap closing point $t_1 = 1.67t$. This is analogous to the semi-Dirac limit for case-II, which now occurs for lower values of t_1. Further, the non-trivial regions corresponding to the middle band have values both $+2$ and -2 for $\pi > |\phi| > 0$ (Figs. 5.5(i)-5.5(l)). The combined phase diagrams corresponding to the conduction, middle and the

valence bands again account for the total Chern number to be vanishing and is similar to the previous case.

There is a subtle issue regarding the non-trivial phases of the system which needs to be mentioned in some details (we have made a brief mention of it in Sec. 5.2). For the well known Haldane model, the topological phase of the system does not depend upon the value of the NNN hopping amplitude t_2, that is, it only requires an infinitesimal t_2 to break the time-reversal invariance, which yields a non-zero Chern number. However, in case of a band deformed dice lattice the non-trivial topology depends on the value of t_2. For example, let us fix t_1, say at $t_1 = 1.4t$ and vary t_2. At $t_2 = 0.05t$, we observe vanishing of the Chern number regardless of the values of ϕ and Δ. However, when $t_2 = 0.1t$ we obtain the $C = |2|$ phase for certain range of values for ϕ and Δ. This implies that at a particular value of t_1, the Chern insulating regions in the Δ-ϕ phase diagram gradually increases with increase in the value of t_2. However, such variation with t_2 occurs for all values of t_1, such that $t_1 > t$ (except for $t_1 = t$). In Fig. 5.6 we have plotted the Chern number as a function of the hopping strength t_1 for various representative values of t_2 indicated in the figure. As can be seen, with increase in the value of t_2, the Chern number vanishes at higher values of t_1. For example, when $t_2 = 0.02t$, the phase transition occurs at $t_1 \simeq 1.16t$. Whereas, for $t_2 = 0.1t$, the transition occurs at $t_1 \simeq 1.67t$. We quote a few other pair of values of t_1 and t_2 for which the Chern number vanishes, such as, $(t_1, t_2) \simeq (1.37t, 0.05t)$, $(1.56t, 0.08t)$, $(1.77t, 0.12t)$ and $(1.84t, 0.14t)$ and so on.

5.3.2 Edge states

In order to visualize the nature of the band gap, that is, whether it is topological or trivial, we look for the crossings of the edge modes with the Fermi energy. To obtain such edge modes in our calculation, we consider a semi-finite ribbon of the system which breaks the periodicity along one direction, while the translational symmetry remains intact along the perpendicular direction. We take the ribbon [70, 185] to be finite along the y-direction and infinite along the x-direction with armchair edges. Further, the sites along the y-direction are labelled as A_1, B_1, C_1, A_2, B_2, C_2 .... A_N, B_N, C_N etc. Now we Fourier transform the operators along the

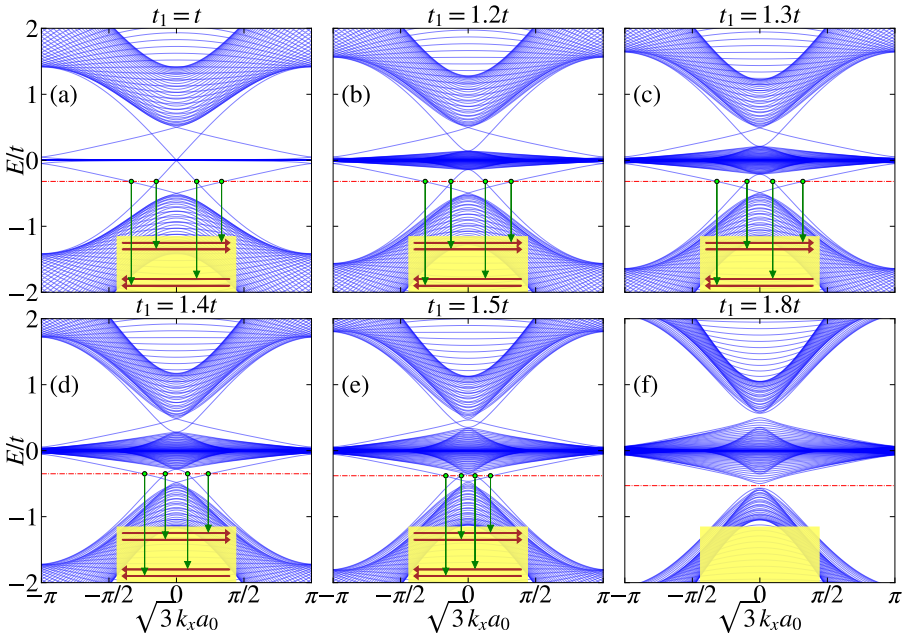

FIG. 5.7: The band structure of the semi-infinite ribbon is shown for (a) $t_1 = t$, (b) $t_1 = 1.2t$, (c) $t_1 = 1.3t$, (d) $t_1 = 1.4t$, (e) $t_1 = 1.5t$, and (f) $t_1 = 1.8t$. The Fermi level is shown via the red dashed line which intersects the edge modes at four distinct points (shown by the green dots). Corresponding to those intersecting points, the edge currents are shown by the red arrows in the yellow panel at the bottom of each figure. The values of t', t_2, ϕ and Δ are taken as t, $0.1t$, $\pi/2$ and zero respectively.

x-direction (k_x being a good quantum number). This yields following sets of three coupled eigenvalue equations for the wave function amplitudes.

$$E_k a_{k,n} = \left[t\left\{b_{k,n+1} + b_{k,n-1}\right\} + t_1 b_{k,n} e^{-i\eta_1 k}\right] + \Delta a_{k,n} + t_2\left[e^{+i\phi}\left\{a_{n-2} + a_{n+1}\left(1 + e^{i(-1)^{n+1}k}\right)\right\} + e^{-i\phi}\left\{a_{n+2} + a_{n-1}\left(1 + e^{i(-1)^{n+1}k}\right)\right\}\right] \tag{5.7}$$

$$E_k b_{k,n} = \left[t\left\{a_{k,n+1} + a_{k,n-1}\right\} + t_1 a_{k,n} e^{+i\eta_1 k}\right] + \left[t c_{k,n+1} + t c_{k,n-1} + t' c_{k,n} e^{-i\eta_2 k}\right] \tag{5.8}$$

$$E_k c_{k,n} = \left[t b_{k,n+1} + t b_{k,n-1} + t' b_{k,n} e^{+i\eta_2 k}\right] - \Delta c_{k,n} + t_2\left[e^{+i\phi}\left\{c_{n+2} + c_{n-1}\left(1 + e^{i(-1)^{n+1}k}\right)\right\} + e^{-i\phi}\left\{c_{n+1} + c_{n-2}\left(1 + e^{i(-1)^{n+1}k}\right)\right\}\right] \tag{5.9}$$

where $a_{k,n}$, $b_{k,n}$ and $c_{k,n}$ are the coefficients of the wave function corresponding to the sublattices A, B and C respectively and n is the site index which takes integer values between $[1 : N]$, with N being the total number of unit cells along the y-direction. Appendix A.2 provides a detailed computation explaining the derivation

of Eqs. 5.7, 5.8 and 5.9. Within the equations, η_1 and η_2 are defined as $\eta_1 = \{1 + (-1)^n\}/2$ and $\eta_2 = \{1 + (-1)^{n+1}\}/2$ respectively. Further, the momentum k is the scaled k_x variable and is defined by $k = \sqrt{3}a_0 k_x$, such that it is rendered dimensionless. The width of the ribbon is related N via $D(N) = \frac{\sqrt{3}a_0}{2}(N-1)$. In our calculation we have taken $N = 80$, which gives the width $D(N) = 79\sqrt{3}a_0/2$.

By solving Eqs. 5.7, 5.8 and 5.9, we have computed the band structure of the semi-infinite ribbon (armchair) corresponding to case-II, that is, for $t' = t$, $t_2 = 0.1t$, $\phi = \pi/2$ and $\Delta = 0$ which is presented in Fig. 5.7. As can be seen, a pair of edge modes from the valence bands crosses over to the middle bands (they are bunched together around the zero energy) and another pair crosses over in the opposite direction. A similar scenario happens corresponding to the modes connecting the conduction bands and the middle bands. Because of these edge modes, the Hall conductivity remains finite, provided the Fermi energy lies in the bulk gap. The Fermi energy in each figure is shown via the red dashed line, which intersects the edge modes at four points (shown by green dots). The edge currents corresponding to those green dots, are shown by the red arrows in the yellow panels in Figs. 5.7(a)-5.7(e). The yellow panels represent a part of the semi-infinite ribbon. Therefore, there are a pair of edge currents along either edges of the ribbon. Since the velocity of the electron is proportional to the slope of the bands, that is, $\partial E/\partial k$, the edge currents along a particular edge move in the same direction, however, along the other edge, each pair moves in the opposite direction. These modes are chiral (and not helical).

Owing to the presence of a pair of edge modes, there will be a quantized Hall conductivity occurring at a value $2e^2/h$, with the factor '2' in front denoting the number of edge modes [189]. This result is consistent with the corresponding Chern numbers of the system as presented in Fig. 5.5. For example, the non-zero edge currents are observed for $t_1 < 1.67t$ (see Fig. 5.7(a) - 5.7(e)) and in this range the Chern number is found to be $|C| = 2$. For $t_1 > 1.67t$, say at $t_1 = 1.8t$, we observe a vanishing Chern number and as well as the edge currents disappear (see Fig. 5.7(f)). The behaviour of the edge states corresponding to case-I, that is, when t_1 and t' are varied simultaneously, are not shown since they are similar to what we observe in Fig. 5.7, with the critical value of t_1 being the only difference,

that is, the edge modes exist till both t_1 and t' remain just below $2t$ (as opposed to $1.67t$).

5.3.3 Hall conductivity

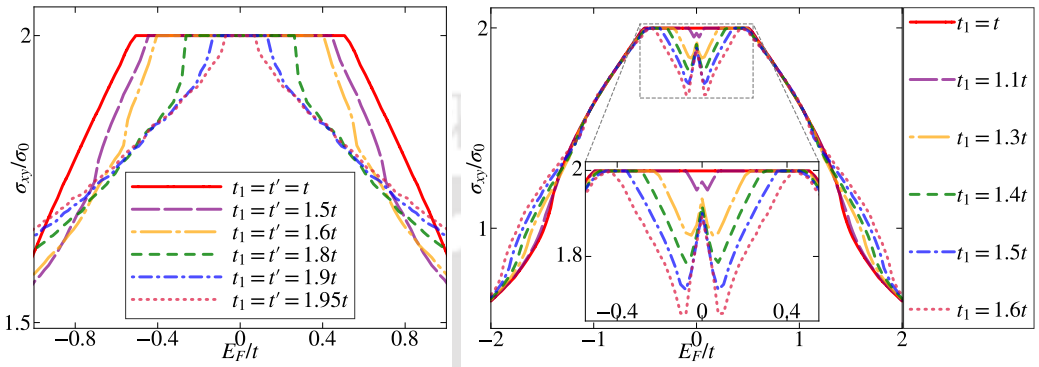

(a) **(b)**

FIG. 5.8: (a) The Hall conductivity is depicted for various values of t_1 and t' shown in the inset. The other parameters are taken as, $t_2 = 0.1t$, $\phi = \pi/2$ and $\Delta = 0$. (b) The Hall conductivity for a fixed t' is depicted for various values of t_1 shown in the panel above. In the inset, a broader view of the regions near zero Fermi energy are shown. The dips in the Hall conductivity are clearly visible. The values of t', t_2, ϕ and Δ are fixed at t, $0.1t$, $\pi/2$ and zero respectively.

In this section we shall compute the Hall conductivity of the system. The Hall conductivity has been calculated using Eq. 1.39 at zero temperature as a function of the Fermi energy E_F and are shown in Figs. 5.8(a) and 5.8(b).

The conductivity plot corresponding to case-I reveals that a plateau quantized at $2e^2/h$ exists as long as E_F remains in the bulk gap of the dispersion spectrum. The value of σ_{xy} starts to decrease when E_F deviates the bulk gap and sinks inside the band (either conduction or the valence bands). This results in diminishing of the plateau width as the values of t_1 and t' increase. This occurs because the gap between the conduction and valence bands shrinks. The Hall conductivity vanishes completely when both t_1 and t' become larger than $2t$. Thus, we observe plateau at $|C|e^2/h$ (also supported by our edge states data) as long as the system remains a non-trivial insulator, which vanishes at the gap closing point at $t_1 = t' = 2t$.

In Fig. 5.8(b), we have presented the Hall conductivity as a function of E_F for

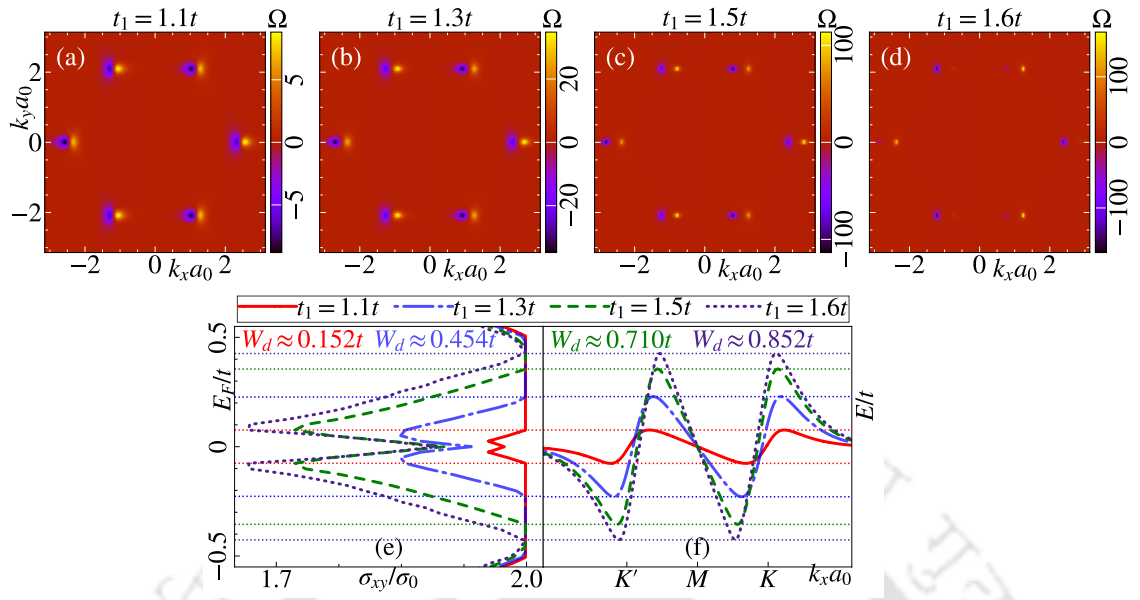

FIG. 5.9: The Berry curvature corresponding to the middle band is presented for (a) $t_1 = 1.1t$, (b) $t_1 = 1.3t$, (c) $t_1 = 1.5t$ and (d) $t_1 = 1.6t$. The values of t', t_2, ϕ and Δ are again taken as t, $0.1t$, $\pi/2$ and zero respectively. A comparison between the dips in the plateau width (W_d) and the bandwidths of the middle band for different values of t_1 are shown in (e) and (f). The Hall conductivities are plotted in (e) along the x-direction, while the middle bands are depicted in (f). Different colours signify different values of t_1. W_d for various values of t_1 are mentioned above the figures.

case-II where only the value of t_1 is tuned, while t' is kept same as t. In this case, the middle band plays an important role in the behaviour of the Hall conductivity as it acquires a dispersive nature. For example, let us fix the value of t_1 at $1.1t$, for which the variation of σ_{xy} is shown in Fig. 5.8(b) via purple color. It shows that there is no longer a smooth plateau in the Hall conductivity, instead, σ_{xy} acquires a dip in the vicinity of zero bias along with a spike occurring at $E_F \simeq 0$. The spike gets more and more prominent with increase of t_1. Further, the dips widen with the increase in the value of t_1 resulting in a diminishing width of the plateau region around the zero Fermi energy. Let us denote the width of the dip as W_d. Notably, W_d becomes very large for $t_1 = 1.6t$. Finally, the plateau and hence the Hall conductivity completely vanish for $t_1 \gtrsim 1.67t$.

The reason of getting a dip in the Hall conductivity can be reconciled from the fact that the dispersive middle band has non-zero Berry curvature, Ω (see Fig. 5.9) which would otherwise be zero for the flat band. Let us say, we set E_F in such a way that some of the states corresponding to the middle band lies

above E_F and others lie below it. So, when we compute the integral of Ω over the occupied states corresponding to the middle band, we get a non-zero value. However, when it is included in the contributions from that of the valence band, the result yields lesser values than $2\sigma_0$ ($\sigma_0 = e^2/h$) for the Hall conductivity. On the other hand, when E_F lies between the gap of the middle and the conduction bands, the integral of Ω corresponding to the middle band completely vanishes. This is consistent with the corresponding value of the Chern number, which is zero for the middle band at $\phi = \pi/2$. Therefore, we observe a plateau at $2\sigma_0$ when E_F lies in the band gap.

In Figs. 5.9(e) and 5.9(f), we have compared the width of the dip (W_d) in the Hall conductivity with the bandwidth of the middle band. The figure clarifies that W_d scales with the bandwidth of the middle band. W_d becomes zero for $t_1 = t$. It increases with increase of t_1, and W_d is maximum below $t_1 = 1.67t$, where the middle band touches both the valence and conduction bands. Beyond $t_1 = 1.67t$, the Hall conductivity vanishes completely.

5.4 Summary

We have presented two schemes through which hopping anisotropies are introduced that induce a band deformation of a Haldane model on dice lattice. In case-I, both t_1 (A-B hopping) and t' (B-C hopping) are varied where the band extrema from the $\mathbf{K}$ and $\mathbf{K}'$ points are shifted. Along with that the band gap diminishes which finally vanishes in the semi-Dirac limit, namely, at $t_1 = t' = 2t$. In contrast, case-II refers to a situation where only t_1 is varied, and the spectrum shows dispersive flat bands. Unlike case-I, the band extremum in case-II located at one of the Dirac points, is displaced slightly in the BZ and the spectral gap closes at $t_1 = 1.67t$. In both the cases we observe the Chern numbers to assume values ± 2 till their respective gap closing transition occurs. However, the shape of the topological lobes in the phase diagrams are distinct in these two cases. Further, a pair of chiral edge modes at each edge are obtained in a nanoribbon geometry which confirms the values of the Chern numbers obtained for these two cases. We have also calculated the anomalous Hall conductivity, which shows

plateaus quantized at $2e^2/h$ as long as t_1 and t' remain less than the semi-Dirac value, namely, $2t$ corresponding to case-I. While in case-II, because of the non-vanishing Berry curvature corresponding to the the middle band, a dip in the plateau appears for $t_1 \neq t$ close to zero Fermi energy. Such dip widens (or the plateau width decreases) with increasing of t_1. The Hall conductivity vanishes for $t_1 \geq 1.67t$ which is in agreement of the vanishing Chern numbers at such values of t_1. Thus, our model of a band-engineered dice lattice presents topological phase transition scenarios from a Chern insulating phase to a trivial insulator across a gap closing point for the hopping amplitude values given by $(t_1, t') = (2t, 2t)$ in case-I and $(t_1, t') = (1.67t, t)$ in case-II.

Chapter 6

Band Engineering of the Quantum Spin Hall Phase: Fate of $\mathbb{Z}_2$ Invariant

So far we have looked at the band-engineered systems with broken TRS, in this chapter, we shall consider restoration of TRS in the system. Such a time-reversal symmetric system in a two-dimensional honeycomb lattice is known as the Kane Mele model [113] which shows quantum spin Hall effect in presence of a Rashba SOC and is characterized by the $\mathbb{Z}_2$ invariant. Further, a band deformation may be achieved via the familiar anisotropic NN hopping t_1. Such an anisotropy shifts the band minima points, which eventually merge onto a single point in the semi-Dirac limit ($t_1 = 2t$), intervening the two Dirac points in the BZ. However, to the best of our knowledge, such shift and merger of the spin bands have not been studied in spin-full systems. Particularly, the band deformation effects are interesting to study in the context of spin transport and evolution of the topological phases in systems where the TRS is intact.

The scenario also motivates us to explore the variation of the $\mathbb{Z}_2$ invariant in the band-deformed Kane-Mele model. The Kane-Mele model belongs to the DII class in the periodic classification of topological insulators [157, 158]. We shall see that such topological invariants vanish as soon as t_1 becomes equal to $2t$, where a trivial phase emerges, thereby indicating a transition from a topological phase to a trivial one through a gap closing point. However, it remains to be seen how the $\mathbb{Z}_2$ number phase diagram vanishes and the spin Hall conductance

respond to the tuning of the band structure across the gap closing (critical) point. To address such questions, we perform a detailed study of the evolution of (spin-resolved) band structure, edge modes in a nanoribbon, the phase diagram and the spin Hall conductivity to study the evolution of the topological properties.

The chapter is organized as follows, in section 6.1 we show our Kane Mele model Hamiltonian in presence of a hopping anisotropy inside a unit cell on a honeycomb lattice. In section 6.2, we have depicted the evolution of the edge states in a nanoribbon and specifically depicted the edge modes and the currents carried by them in relevance to the ongoing discussion. Then, in section 6.3 we investigate the evolution of the phase diagram which characterizes the topological phase and also its disappearance in a quantitative manner. Finally we show the spin Hall conductivity in section 6.4 and conclude with a brief summary of our results in section 6.5.

6.1 Model Hamiltonian

Consider the Kane Mele Hamiltonian on a honeycomb lattice with different nearest neighbour (NN) hopping strengths which we show in Fig. 6.1. The hopping strengths along the $\boldsymbol{\delta}_2$ and $\boldsymbol{\delta}_3$ directions are t, while in the third direction, that is along $\boldsymbol{\delta}_1$, the strength is t_1. The NN vectors are given by $\boldsymbol{\delta}_1 = a_0(0,1)$, $\boldsymbol{\delta}_2 = a_0(\sqrt{3}/2, -1/2)$ and $\boldsymbol{\delta}_3 = a_0(-\sqrt{3}/2, -1/2)$. We assume t_1 is a tunable parameter and is defined in the range, $t \leq t_1 \leq 2t$. The value $t_1 = 2t$ denotes a critical point which we termed as the semi-Dirac case. We have also considered values beyond the semi-Dirac limit, namely $t_1 > 2t$. The Hamiltonian can be written as follows,

$$H = \sum_{\langle ij \rangle} t_{ij} c_i^\dagger c_j + i\lambda_{\rm SO} \sum_{\langle\langle ij \rangle\rangle} \nu_{ij} c_i^\dagger s^z c_j + i\lambda_{\rm R} \sum_{\langle ij \rangle} c_i^\dagger (\mathbf{s} \times \hat{\mathbf{d}}_{ij})_z c_j + \lambda_{\rm v} \sum_i \xi_i c_i^\dagger c_j \qquad 6.1$$

Here $t_{ij} = t_1$ or t when j denotes the neighbours $\boldsymbol{\delta}_1$ or $\boldsymbol{\delta}_{2,3}$ respectively. The first term denotes the direction dependent nearest neighbour hopping. The second term is the complex NNN hopping which encodes a sign difference between the spin-$\uparrow$ and spin-$\downarrow$ electrons. It is usually denoted as the intrinsic spin-orbit cou-

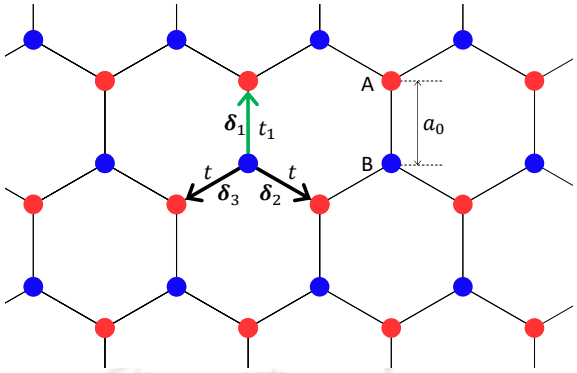

FIG. 6.1: A honeycomb lattice is shown where the red and the blue circles represent the sublattices A and B respectively. In the $\boldsymbol{\delta}_2$ and $\boldsymbol{\delta}_3$ directions the NN hopping strengths are same (t) while in the $\boldsymbol{\delta}_1$ direction it is t_1.

pling with a coupling strength $\lambda_{\rm SO}$. Here, $\nu_{ij} = \text{sgn}(\hat{\mathbf{d}}_1 \times \hat{\mathbf{d}}_2)_z = \pm 1$, where $\hat{\mathbf{d}}_1$ and $\hat{\mathbf{d}}_2$ are the unit vectors along the two bonds that electron traverses while going from site j to NNN site i. s denotes the Pauli matrices describing the electron spin. The third term is the nearest neighbour Rashba spin-orbit interaction with strength $\lambda_{\rm R}$ where $\hat{\mathbf{d}}_{ij}$ is a unit vector of nearest neighbour sites pointing from site i to site j. This term breaks the $z \to -z$ mirror symmetry, and as a result, the spins in the z direction are no longer conserved. The fourth term is the staggered sublattice potential that induces an energy difference between A and B sublattices and $\xi_i = \pm 1$.

Performing a Fourier transform on the Hamiltonian in Eq. 6.1 can be written as,

$$H(\mathbf{k}) = \begin{pmatrix} \gamma(\mathbf{k}) + \lambda_{\rm v} & \zeta(\mathbf{k}) & 0 & \rho(\mathbf{k}) \\ \zeta^*(\mathbf{k}) & -\gamma(\mathbf{k}) - \lambda_{\rm v} & -\rho(-\mathbf{k}) & 0 \\ 0 & -\rho^*(-\mathbf{k}) & -\gamma(\mathbf{k}) + \lambda_{\rm v} & \zeta(\mathbf{k}) \\ \rho^*(\mathbf{k}) & 0 & \zeta^*(\mathbf{k}) & \gamma(\mathbf{k}) - \lambda_{\rm v} \end{pmatrix} \tag{6.2}$$

where,

$$\zeta(\mathbf{k}) = t_1 e^{-ik_y a} + 2te^{\frac{ik_y a}{2}} \cos\frac{\sqrt{3}k_x a}{2}, \tag{6.3a}$$

$$\gamma(\mathbf{k}) = 2\lambda_{\rm SO}\left[2\sin\frac{\sqrt{3}k_x a}{2}\cos\frac{3k_y a}{2} - \sin\sqrt{3}k_x a\right], \tag{6.3b}$$

and,

$$\rho(\mathbf{k}) = i\lambda_{\mathrm{R}}\left[e^{-ik_y a} + e^{\frac{ik_y a}{2}} 2\cos\left(\frac{\sqrt{3}k_x a}{2} + \frac{\pi}{3}\right)\right] \tag{6.3c}$$

The above Hamiltonian obeys the time-reversal symmetry. The corresponding discussion for the low energy Hamiltonian can be found in Sec. 1.7.

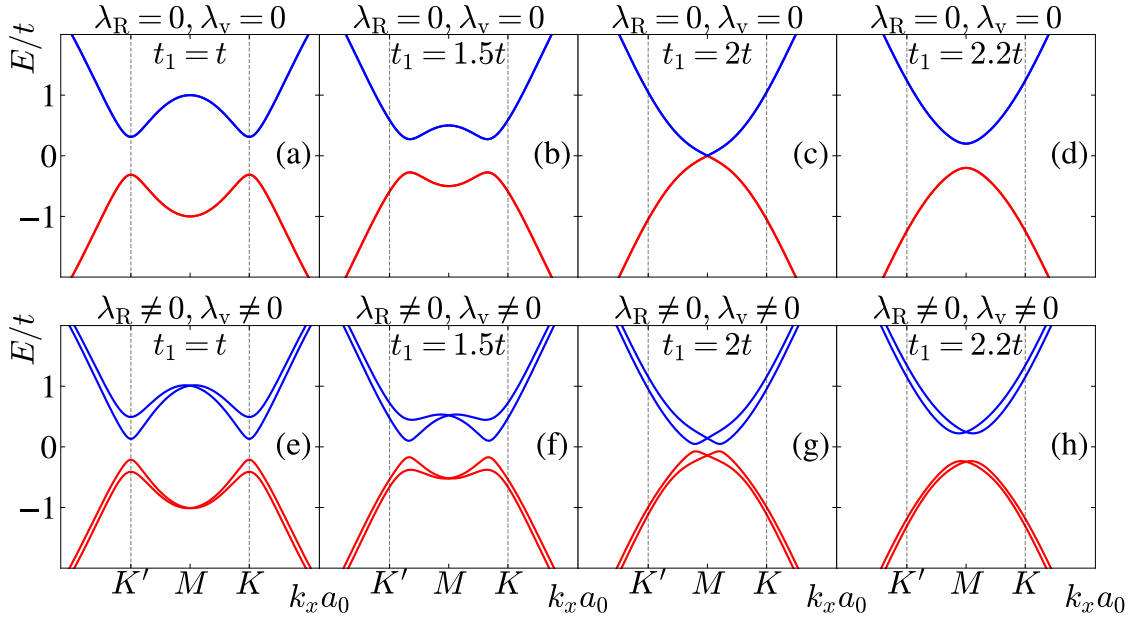

FIG. 6.2: The energy band structure corresponding to the Hamiltonian in Eq. (3.2) along the k_x axis ($k_y a_0$ is fixed at $2\pi/3$) are shown for $t_1/t = 1$ in (a) and (e), $t_1/t = 1.5$ in (b) and (f), $t_1/t = 2$ in (c) and (g), and $t_1/t = 2.2$ in (d) and (h). RSOC and sublattice potential both are zero in (a)-(d), while they have values $\lambda_{\mathrm{R}} = 0.05t$ and $\lambda_{\mathrm{v}} = 0.1t$ in (e)-(h). The non-zero values of λ_{R} (together with λ_{v}) term makes the bands spin resolved and hence distinct as shown in (e)-(h). The intrinsic SOC is fixed at $0.06t$.

The band structure of this Hamiltonian have been calculated numerically and presented in Fig. 6.2 for various values of t_1 in absence of λ_{R} and λ_{v} (λ_{R} and λ_{v} are set to zero for now) so as to demonstrate the effects of the band deformation in presence of the spin dependent Haldane flux. The NNN hopping amplitude is fixed at $0.06t$. For $t_1 = t$ (let us denote this as the Dirac case to distinguish it from the semi-Dirac case where the latter corresponds to $t_1 = 2t$), gaps open up at the two non-equivalent Dirac points, that is, at the $\mathbf{K}$ $(2\pi/3\sqrt{3}a_0, 2\pi/3a_0)$ and the $\mathbf{K}'$ $(-2\pi/3\sqrt{3}a_0, 2\pi/3a_0)$ points as depicted in Fig. 6.2(a). It should be noted that the band dispersion for the spin-$\uparrow$ and spin-$\downarrow$ electrons are identical. There

are, in fact two conduction and two valence bands, one for each of the $\uparrow$ and $\downarrow$ spins. However, in the absence of the Rashba and the Semenoff terms, these bands are degenerate. As t_1 is tuned to larger values, these two points come closer to each other and the band gap decreases. When t_1 becomes equal to $2t$, that is the semi-Dirac limit, the gap vanishes at the M $(0, 2\pi/3a_0)$ point (see Fig. 6.2(c)). Eventually when t_1 exceeds $2t$, the gap again opens up in the spectrum (see Fig. 6.2(d)). The nature of the two gaps are different, and which is what we show below.

Now if we include the Rashba coupling ($\lambda_{\rm R}$) and the sublattice potential ($\lambda_{\rm v}$), then the bands corresponding to the $\uparrow$-spins or $\downarrow$-spins become distinct as shown in Figs. 6.2(e)-6.2(h). Hence, in this case we see a pair of conduction and valence bands for each spin. It should be noted that below the semi-Dirac limit, that is, for $t_1 < 2t$, there exists a certain value of $\lambda_{\rm R}$ and $\lambda_{\rm v}$, where the gap vanishes completely and the bands touch (semi-metallic state). With further increase in the value of $\lambda_{\rm R}$ and $\lambda_{\rm v}$, the gap opens up again. However, such opening and closing of the spectral gaps are different in the semi-Dirac limit ($t_1 = 2t$), where there is no gap for $\lambda_{\rm R}$ and $\lambda_{\rm v}$ to be both zero. With the increase of $\lambda_{\rm R}$ and $\lambda_{\rm v}$, the gap opens up, but unlike the previous case, no closing of the band gap is observed in the dispersion spectrum. For $t_1 > 2t$, the dispersion is always gapped for any finite value of $\lambda_{\rm R}$ or $\lambda_{\rm v}$.

6.2 Edge states

To understand the distinction between the spectral gaps observed for finite values of $\lambda_{\rm R}$ and $\lambda_{\rm v}$ ($\lambda_{\rm SO}$ is always taken to be non-zero in our discussion) corresponding to the Dirac ($t_1 = t$) and the semi-Dirac ($t_1 = 2t$) cases, we ascertain the existence (or absence) of the edge states. To achieve this, we consider a finite strip of the system which breaks the periodicity along a particular direction, but allows translational invariance along the perpendicular direction. Such a system is known as semi-infinite ribbon, which we have taken to be finite along the y-direction and infinite along the x-direction. We label the sites as A_1, B_1, A_2, B_2, ... A_N, B_N etc. along the y-direction. Owing to translational invariance is

the x-direction, we can Fourier transform the operators only in the x-direction, namely, use $c^{\dagger}_{x,y} = \sum_k e^{ikx} c^{\dagger}_{k,y}$. Using such a transformation on the Hamiltonian in Eq. (6.1), we arrive at the following system of eigenvalue equations for the wave functions,

$$\begin{aligned} E_k a_{k,n} = &\left[t\left\{1+e^{(-1)^{n+1}ik}\right\} b_{k,n} + t_1 b_{k,n+1}\right] s_0 + \lambda_v a_{k,n} s_0 \\ &+ 2\lambda_{SO}\left[a_{k,n}\sin k + e^{(-1)^{n+1}\frac{ik}{2}} \sin\frac{k}{2}\left\{a_{k,n-1}+a_{k,n+1}\right\}\right] s_z + \\ i\lambda_R &\left[\left\{-\frac{1}{2}\left(1+e^{(-1)^{n+1}ik}\right) b_{k,n} + b_{k,n+1}\right\} s_y - \left\{(-1)^n \frac{\sqrt{3}}{2}\left(1-e^{(-1)^{n+1}ik}\right) b_{k,n}\right\} s_x\right] \end{aligned} \tag{6.4}$$

$$\begin{aligned} E_k b_{k,n} = &\left[t\left\{1+e^{(-1)^{n}ik}\right\} a_{k,n} + t_1 a_{k,n-1}\right] s_0 - \lambda_v b_{k,n} s_0 \\ &+ 2\lambda_{SO}\left[b_{k,n}\cos k + e^{(-1)^{n}\frac{ik}{2}} \cos\frac{k}{2}\{a_{k,n-1}+a_{k,n+1}\}\right] s_z + \\ &i\lambda_R\left[\left\{\frac{1}{2}\left(1+e^{(-1)^{n}ik}\right) b_{k,n} + b_{k,n-1}\right\} s_y - \left\{(-1)^{n+1}\frac{\sqrt{3}}{2}\left(1-e^{(-1)^{n}ik}\right) a_{k,n}\right\} s_x\right] \end{aligned} \tag{6.5}$$

where n stands for the n-th sublattice which is an integer in the range $[1:N]$ with N being total number of unit cells along the y-direction and k is the dimensionless momentum along the x-direction, such that, $k = \sqrt{3}a_0 k_x$. Also $s_i\,(i = x, y, z)$ denote the Pauli matrices and s_0 is the 2×2 identity matrix. A detailed calculation leading to the Hamiltonian including the Rashba term is presented in Appendix B.2. In the above equations $a_{k,n}$ and $b_{k,n}$ are the coefficients of the wavefunction corresponding to the sublattices A and B respectively, with momentum k. By solving these two equations, one can get the energy band structure for the ribbon for any arbitrary value of t_1. The width of the ribbon, D can be written in terms of N, given by, $D(N) = a_0\left(\frac{3N}{2} - 1\right)$. In our work, we have used $N = 100$ and hence the width of the ribbon is $149a_0$ along the y-direction. As can be seen from the Fig. 6.3, a pair of modes from the lower (valence) band crosses over to the upper (conduction) band, and another pair crosses in the opposite direction. The amplitudes of the wave functions of these modes decay exponentially into the bulk, with their values being maximum at the edges of the ribbon [185, 186]. It should be noted that the velocities have opposite signs (since the velocity is pro-

portional to $\partial E/\partial k$) along these modes, which implies that electrons propagate in opposite directions along each edge. These edge states are called as helical states as opposed to chiral modes corresponding to the quantum Hall case.

Let us scrutinize Fig. 6.3 in more details. In Fig. 6.3(a) we have shown the band structure corresponding to the Dirac case ($t_1 = t$), where the intersection of the edge states with the Fermi energy, E_F (shown via a red dashed line near $E/t = 0$) are represented by the green dots labelled as p, q, r and s. The edge currents (proportional to the velocities) at those points are shown in the yellow panel of Fig. 6.3(e), where the yellow panel represents a part of the ribbon. As can be seen (Fig. 6.3(e)) that there are counter propagating edge currents along either edge of the ribbon, and these edge currents are spin resolved, that is, they are different for spin-$\uparrow$ and spin-$\downarrow$. Since the system possesses TRS, the quantized (charge) Hall conductivity vanishes, however there will be a non-zero spin Hall conductivity, should the Fermi energy lies in the bulk gap. This state is known as the quantum spin Hall (QSH) phase and denotes a topological state of matter, that is, distinct from the familiar quantum Hall state. These edge currents will exist as long as the hopping strength t_1 remains lower than $2t$ (the semi-Dirac limit).

In Fig. 6.3(b), we have shown the band structure for $t_1 = 1.5t$ which is similar to the case $t_1 = t$, except that the bulk band gap being less. So, similar helical edge currents are observed for $t_1 = 1.5t$ (Fig. 6.3(e)). Now if we increase t_1 to $2t$ or even beyond that (Fig. 6.3(c) and 6.3(d)), we see that there are 4 additional intersections of the edge states with the Fermi energy, E_F which are denoted by the points u, v, w and x. Hence there are a total of two pairs of the edge modes along either edge of the ribbon (Fig. 6.3(f)), where for both $\uparrow$ and $\downarrow$ spins, the edge currents flow in opposite directions. Therefore in this case, the spin Hall conductivity vanishes completely and the system is devoid of any topological property [146]. This phenomenon persists for $t_1 > 2t$. Thus the edge states in a finite ribbon endorses a vanishing of the QSH phase in the semi-Dirac limit. The current is cancelled in the semi-Dirac case due to the counter propagating spin resolved edge modes at each edge. This signals a topological phase transition occurring at the critical point, namely, $t_1 = 2t$. Beyond this point, the edge modes

are completely split from the bulk, thereby yielding a trivial insulating state.

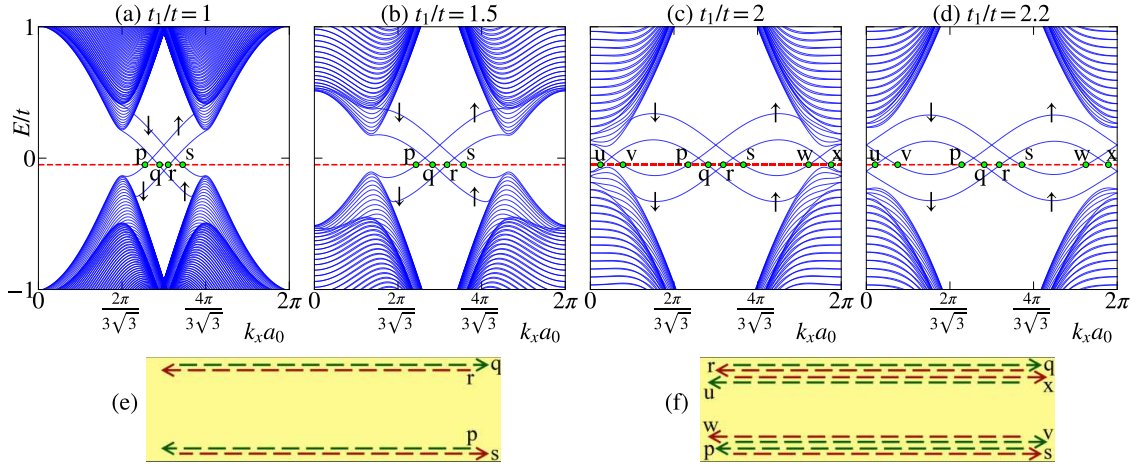

FIG. 6.3: The energy spectra corresponding to a semi-infinite ribbon are shown for (a) $t_1/t = 1$, (b) $t_1/t = 1.5$, (c) $t_1/t = 2$ and (d) $t_1/t = 2.2$. In each figure, the edge modes corresponding to the spin-$\uparrow$ and spin-$\downarrow$ electrons are also depicted. The yellow panels in (e) and (f) represents a part of the semi-infinite ribbon, where the edge currents corresponding to the green dots are shown by arrows. The green dots in each figure signify the intersection of the edge states with the Fermi energy E_F (shown via the red dashed line). Through out the calculations N ($D(N) = 149a_0$), $\lambda_{\rm SO}$, $\lambda_{\rm v}$ and $\lambda_{\rm R}$ are kept fixed at 100, $0.06t$, $0.1t$ and $0.05t$ respectively.

6.3 The Phase diagram

The quantum spin Hall (QSH) phase is characterized by a non-vanishing $\mathbb{Z}_2$ topological invariant (defined below). In this section, we show the variation of the $\mathbb{Z}_2$ invariant as we smoothly migrate from the Dirac to the semi-Dirac limit. For the calculation of this $\mathbb{Z}_2$ index, Eq. 1.32 described in Sec. 1.1.4 can be used. However, for completeness, we present another method to compute such invariant as follows.

Let us consider the Bloch wave functions, $u_i(\mathbf{k}_i)$ of the occupied bands corresponding to a pair of points $\mathbf{k}_1$ and $\mathbf{k}_2$ in the Brillouin zone. These two points denote the locations of the band extrema (minima for the conduction band and maximum for the valence band) in the BZ. Note that corresponding to the Dirac case, $\mathbf{k}_1$ and $\mathbf{k}_2$ denote the Dirac points $\mathbf{K}$ and $\mathbf{K}'$ respectively, however they shift

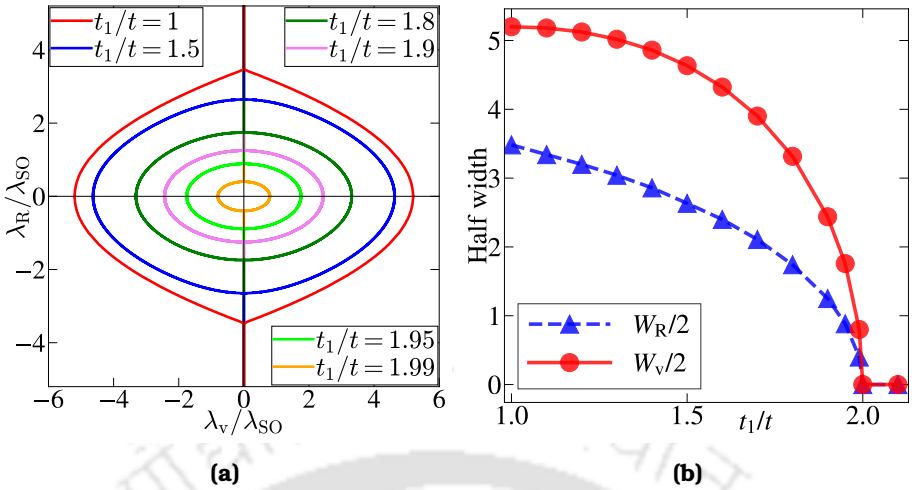

FIG. 6.4: (a) The phase diagram of the system in the λ_R-λ_v plane is shown for several values of t_1. The region enclosed by each curve represents the quantum spin Hall insulating phase where the $\mathbb{Z}_2$ index has a value 1, while the outside region denotes the trivial insulator where the $\mathbb{Z}_2$ index vanishes. The gradual vanishing of the area enclosed by each curve is shown. (b) The half width of the spin Hall insulating regime along the λ_v/λ_{SO} direction is shown by the red curve (denoted by $W_v/2$), while along the λ_R/λ_{SO} direction, it is shown by the blue curve (denoted by $W_R/2$).

for $t_1 \neq t$. The wave function at one of these points can be obtained by time reversing the wave function corresponding to the other one, that is, $|u_i(\mathbf{k}_1)\rangle = \Theta\,|u_i(\mathbf{k}_2)\rangle$ and vice versa where Θ denotes the time reversal operator. Since the Hamiltonian is time reversal invariant, so we can decompose the Hamiltonian, $H(\mathbf{k})$ and its corresponding occupied band wave functions, $|u_i(\mathbf{k})\rangle$ into even and odd subspaces. The even subspace has the property that $\Theta\,|u_i(\mathbf{k})\rangle$ is equivalent to $|u_i(\mathbf{k})\rangle$ upto a $U(2)$ rotation. Whereas, the wave functions corresponding to the odd subspace has the property that the space spanned by $\Theta\,|u_i(\mathbf{k})\rangle$ is orthogonal to that of $|u_i(\mathbf{k})\rangle$. Now the $\mathbb{Z}_2$ invariant [146, 147] can be calculated by considering the momenta which belong to this odd subspace. We compute the expectation value of the time reversal operator between $|u_i(\mathbf{k})\rangle$ and $|u_j(\mathbf{k})\rangle$, namely, $\langle u_i(\mathbf{k})|\Theta|u_j(\mathbf{k})\rangle$. This yields a matrix which is antisymmetric. Hence we have,

$$\langle u_i(\mathbf{k})|\Theta|u_j(\mathbf{k})\rangle = \epsilon_{ij} P(\mathbf{k}), \tag{6.6}$$

where ϵ_{ij} is the Levi-Civita symbol and $P(\mathbf{k})$ is the Pfaffian of the matrix [195, 196]

defined as,

$$P(\mathbf{k}) = \mathrm{Pf}\left[\langle u_i(\mathbf{k})|\Theta|u_j(\mathbf{k})\rangle\right] \tag{6.7}$$

For a 2×2 antisymmetric matrix A_{ij}, the Pfaffian picks up the off-diagonal component. Now the absolute value of this Pfaffian is unity in the even subspace, while it is zero in the odd subspace. So we dissect the BZ into two halves such that the points $\mathbf{k}_1$ and $\mathbf{k}_2$ lie in different halves. Thus the $\mathbb{Z}_2$ index can be computed via performing the integral [113],

$$\mathbb{Z}_2 = \frac{1}{2\pi i}\oint_C \mathrm{d}\mathbf{k}\cdot\boldsymbol{\nabla}\ln\left[P(\mathbf{k})+i\delta\right] \tag{6.8}$$

where δ is a convergence factor and the contour C is the circumference of the halved BZ discussed above. This integral can be used to compute the $\mathbb{Z}_2$ invariant for any values of λ_R and λ_v. Nonetheless, in the subsequent discussion, we shall focus on a more straightforward approach to determine this topological invariant when the system possesses no sublattice potential and no RSOC, that is, when $\lambda_\mathrm{R}=\lambda_\mathrm{v}=0$.

For the above case, first we need to calculate the matrix ω of the time-reversed Bloch states,

$$\omega_{ij}(\mathbf{k}) = \langle u_i(\mathbf{k})|\Theta|u_j(\mathbf{k})\rangle. \tag{6.9}$$

Now, we use the following relation to compute the $\mathbb{Z}_2$ invariant,

$$(-1)^{\mathbb{Z}_2} = \prod_{i=1}^{4}\gamma_i, \quad \text{with} \quad \gamma_i = \frac{\sqrt{\det[\omega(\mathbf{\Gamma}_i)]}}{\mathrm{Pf}[\omega(\mathbf{\Gamma}_i)]}. \tag{6.10}$$

Here, $\mathbf{\Gamma}_i$s are the time-reversal invariant momenta (TRIM) points. The TRIM points for the honeycomb lattice is given by,

$$\mathbf{\Gamma}_1 = a_0(0,0), \mathbf{\Gamma}_2 = \frac{2\pi}{3a_0}\left(\frac{-\sqrt{3}}{2},1\right), \mathbf{\Gamma}_3 = \frac{2\pi}{3a_0}\left(\frac{\sqrt{3}}{2},1\right), \text{ and } \mathbf{\Gamma}_4 = \frac{2\pi}{3a_0}(0,1) \tag{6.11}$$

The Pfaffian $\mathrm{Pf}(\mathbf{\Gamma})$ is the square root of the antisymmetric matrix $\omega(\mathbf{\Gamma}_i)$. As a result, the sign of γ_i depends on the branch of the square root in Eq. 6.10. The branch is chosen in such a way that $|u_i(\mathbf{k})\rangle$ and $\sqrt{\det[\omega(\mathbf{\Gamma}_i)]}$ are continuous at

the TRIM points.

In Fig. 6.4(a) we have shown the phase diagram of the system as it is deformed from the Dirac to the semi-Dirac limit. For a given value of t_1, we have obtained the phase diagram in the λ_R-λ_v plane. As can be seen that there are two regions in the phase diagram for all values of t_1 less than $2t$, comprising of the topological and the trivial phases. The region enclosed by each curve has the $\mathbb{Z}_2$ invariant equal to 1, while it vanishes outside the enclosed region. That means, the system shows non-trivial topology inside the enclosed region ($\mathbb{Z}_2 = 1$) and in the outside region, the system is trivial ($\mathbb{Z}_2 = 0$). It should be noted that the Dirac case ($t_1 = t$) yields the phase diagram obtained by Kane and Mele [113] (red curve in Fig. 6.4(a)) where the phase transition occurs at $\lambda_v = 3\sqrt{3}\lambda_{SO}$ for $\lambda_R = 0$. Whereas, if we look at the phase diagrams for other values of t_1, that is intervening the Dirac and the semi-Dirac cases, the extent of the topological regime gradually shrinks. These results are consistent with the band structure plots (see Fig. 6.2). As the band gap decreases with increasing values of t_1, the phase transition from the topological to trivial phase now occurs for progressively lesser values of λ_v and λ_R. In the semi-Dirac limit ($t_1 = 2t$), the system shows gapless band structure in the absence of both λ_R and λ_v and the $\mathbb{Z}_2$ number is identically equal to zero. Therefore, $t_1 = 2t$ denotes a critical point which demarcates the topological insulator from a band insulating phase. As the value of t_1 becomes larger than $2t$ (say $t_1 = 2.2t$), the system remains a band insulator.

It should be noted that the plots in the phase diagram in Fig. 6.4(a) represent the semi-metallic state of the system, or equivalently, the system shows gapless dispersion. For example, when $\lambda_R = 0$, the spectrum is gapless at $(\lambda_v, t_1) = (3\sqrt{3}\lambda_{SO}, t)$, $(\frac{7}{4}\sqrt{7}\lambda_{SO}, 1.5t)$, $(\frac{19}{25}\sqrt{19}\lambda_{SO}, 1.8t)$, $(\frac{39}{100}\sqrt{39}\lambda_{SO}, 1.9t)$, $(\frac{79}{400}\sqrt{79}\lambda_{SO}, 1.95t)$, $(\frac{399}{10^4}\sqrt{399}\lambda_{SO}, 1.99t)$ and $(0, 2t)$ where the values lie on the x axis in the first quadrant of Fig. 6.4(a). On the other hand, in the absence of λ_v, the semi-metallic states are realized for $(\lambda_R, t_1) = (3.46\lambda_{SO}, t)$, $(2.63\lambda_{SO}, 1.5t)$, $(1.74\lambda_{SO}, 1.8t)$, $(1.25\lambda_{SO}, 1.9t)$, $(0.87\lambda_{SO}, 1.95t)$, $(0.39\lambda_{SO}, 1.99t)$ and $(0, 2t)$ which lie on the positive y-axis of Fig. 6.4(a).

The shrinking of the half width (measured from the center in Fig. 6.4(a)) along the λ_R axis ($\lambda_v = 0$) of the non-trivial insulating region in the phase diagram

is shown in Fig. 6.4(b) (the blue curve). As can be seen, the width ($W_{\rm R}/2$) is maximum at $t_1 = t$ and has a value $2\sqrt{3}\lambda_{\rm SO}$ (non-zero $W_{\rm R}$ implies $\mathbb{Z}_2 = 1$, while $W_{\rm R} = 0$ implies $\mathbb{Z}_2 = 0$), which was obtained by Kane and Mele [113]. Now with increase in the value of t_1, $W_{\rm R}/2$ decreases slowly. However there is a rapid decrease in the width as t_1 approaches $2t$. $W_{\rm R}/2$ eventually vanishes at the critical point (semi-Dirac), namely, $t_1 = 2t$. In the same figure (Fig. 6.4(b)) we have also depicted the variation of the half width along the $\lambda_{\rm v}$ direction ($\lambda_{\rm R} = 0$), namely $W_{\rm v}/2$ as a function of t_1/t. In this case also, the width $W_{\rm v}/2$ falls off slowly near $t_1 = t$ but as t_1 increases, $W_{\rm v}/2$ drops rapidly in the vicinity of $t_1 = 2t$. $W_{\rm v}/2$ vanishes at the critical point, $t_1 = 2t$ and continues to remain at zero for $t_1 > 2t$. The analytic form of the width, say for $W_{\rm v}/2$ as a function of t_1/t can be obtained as,

$$\frac{W_{\rm v}}{2} = \left(2 + \frac{t_1}{t}\right)^{3/2} \sqrt{2 - \frac{t_1}{t}} \qquad 6.12$$

where the equation is valid for $t \leq t_1 < 2t$. From this equation one can get the half width in the phase diagram along the horizontal direction for $t_1 = t$ is $3\sqrt{3}\lambda_{\rm SO}$, which is a well known result in the Kane-Mele model [113] and mentioned earlier. For $t_1 = 2t$, this width vanishes and the topological regime ceases to exist.

6.4 Spin Hall conductivity

In this section we present numerical calculations of the spin Hall conductivity for our system. In order to calculate the spin Hall conductivity, we first obtain the low energy form of the Hamiltonian in Eq. 6.1 for different values of t_1. Such a low energy expansion of the Hamiltonian will be helpful for our purpose, which can be written in a compact notation as,

$$\begin{aligned} H(q_x, q_y) =& \zeta_x(q_x, q_y, t_1)\sigma_x s_0 + \zeta_y(q_x, q_y, t_1)\sigma_y s_0 + \gamma(q_x, q_y, t_1)\sigma_z s_z + \\ & \left[\rho_x(q_x, q_y, t_1)\sigma_x + \rho_y(q_x, q_y, t_1)\sigma_y\right](s_x - s_y) \end{aligned} \qquad 6.13$$

where the coefficients ζ_x, ζ_y, γ and ρ_x and ρ_y are functions of the momentum $\mathbf{q}$ (measured relative to the band extrema) and the hopping strength t_1. s_x, s_y

and s_z are the 2×2 Pauli matrices which represent the real spin of the electrons, while the other 2×2 Pauli matrices σ_x, σ_y and σ_z represent the sublattice degree of freedom and s_0 is the 2×2 identity matrix. We have presented all of these coefficients, namely, ζ_x, ζ_y, γ, ρ_x and ρ_y in Appendix B. It should be noted that the low energy expansions are done at different points in the BZ for different values of t_1, since the band minima shift as we change t_1 relative to t (see Fig. 6.2). For example, at $t_1 = t$, the band minima occur at $\mathbf{K}$ $(2\pi/3\sqrt{3}a_0, 2\pi/3a_0)$ and at $\mathbf{K}'$ $(-2\pi/3\sqrt{3}a_0, 2\pi/3a_0)$ points, whereas at $t_1 = 2t$ the band minima occur at the $\mathbf{M}(0, 2\pi/3a_0)$ point in the BZ. Thus the approximations are done at locations in the BZ where the spectral gap is minimum for all values of t_1.

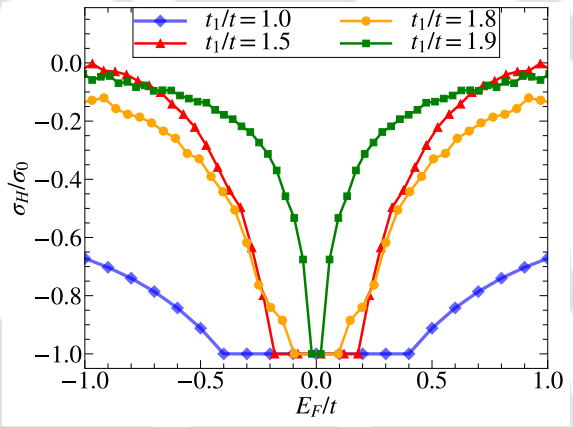

FIG. 6.5: The evolution of the spin Hall conductivity of the system for various values of t_1 as a function of the Fermi energy E_F. The plateau width gets gradually narrower, before vanishing at the semi-Dirac limit.

In order to calculate the Hall conductivity we have used the following formula [197–199],

$$\sigma_H^z = e\hbar \sum_\lambda \int \frac{d\mathbf{q}}{(2\pi)^2} f(E_n)\Omega_{xy}^z(\mathbf{q}) \qquad 6.14$$

where $f(E_n) = [e^{\beta(E_n - E_F)} + 1]^{-1}$ is the Fermi-Dirac distribution function corresponding to a given energy E_n and $\beta(= (K_B T)^{-1})$ is the inverse temperature. Ω_{xy}^z is the Berry curvature which can be evaluated from the following expression,

$$\Omega_H^z(\mathbf{q}) = i \sum_{m \neq n} \frac{\langle n|v_{sx}^z|m\rangle\langle m|v_y|n\rangle - (x \leftrightarrow y)}{[E_n(\mathbf{q}) - E_m(\mathbf{q})]^2} \qquad 6.15$$

where $x \leftrightarrow y$ denotes interchanging x and y variables in the first term. Further, $\Omega_H^z(\mathbf{q})$ is the spin dependent Berry curvature, $\{|n\rangle, E_n\}$ denotes the eigensolutions corresponding to the Hamiltonian in Eq. 6.13, $v_i = \frac{1}{\hbar}\partial H/\partial k_i$ is the velocity operator and $v_{si}^z = \frac{1}{2}\{v_i, \frac{\hbar}{2}s_z\sigma_0\}$ is the velocity operator corresponding to the spin current. The integral is performed over the states which are occupied at a given value of the Fermi energy. Using Eqs. 6.13, 6.14 and 6.15, we have computed the spin Hall conductivity numerically as a function of E_F at a temperature, $T = 0$ for various values of t_1 as shown in Fig. 6.5. We can see that as long as the Fermi energy lies in the bulk gap, the Hall conductivity possesses a plateau and hence quantized in unit of σ_0 ($= e/2\pi$) [114]. The spin Hall conductivity however decreases rapidly as the Fermi energy moves away from the gapped region. With increase in the value of t_1, the quantized plateau stays at $e/2\pi$, except that the plateau width decreases, which eventually vanishes at $t_1 = 2t$. Thus a vanishing of the QSH phase indeed occurs because of the band deformation induced by the hopping anisotropy as discussed throughout the paper. The above scenario also implies that $\mathbb{Z}_2$ invariant vanishes in the semi-Dirac limit.

6.5 Summary

We have investigated the evolution of the electronic dispersion and the topological properties in the semi-Dirac Kane Mele model with the inclusion of a differential hopping between the neighbours on a honeycomb lattice. This causes deformation of the (spin resolved) bands which are evident from our band structure calculations. The electronic band dispersion shows the band minima originally located at the Dirac points to migrate towards each other and finally merge at the M point, where the gap vanishes completely in the semi-Dirac limit. The model shows a topological phase transition from a non-trivial spin Hall insulating phase to a trivial band insulator at the semi-Dirac limit. Further, such a topological phase transition is adequately supported via computing the helical edge modes, $\mathbb{Z}_2$ invariant, phase diagram and the spin Hall conductivity.

Chapter 7

Concluding Remarks

The study of topological properties in systems has been a wide attention in the condensed matter community. It all started with the discovery of quantum Hall effect, however, gained importance after Haldane's groundbreaking work on topological phases in the honeycomb lattice without an external magnetic field. Later on, various other type of topological insulators, namely, the quantum spin Hall insulators, have been discovered which could produce their own magnetic fields through internal interactions between the charges and the nuclei, and are described by the famous Kane-Mele Model. This special type of insulator is relevant because the spin-orbit coupling is the main ingredient here, which can be controlled by an external gate voltage, and hence they are considered potential applications for spintronic devices. Moreover, topological insulators denote a wide variety of systems depending on their symmetries, making them promising candidates for fundamental research. Hence, we have introduced these in Chapter 1, where various topological invariants and their classifications have been included. It also shows a detailed explanation of the method to compute those invariants and the calculation of Hall conductivity.

It is fairly well understood that the topological properties are intimately linked with the band structures. Therefore, band engineering has the potential to alter these topological properties. Consequently, controlled deformation of the band(s) can induce a topological phase transition. The study of such phase transitions is currently being investigated to gain a better understanding of the critical prop-

erties in the vicinity of these transitions. In line with that, we have illustrated electronic properties of two-dimensional Dirac and semi-Dirac systems, where the former shows isotropic linear dispersion, while the latter exhibits quadratic dispersion in one direction and linear in the other direction. The behaviour of the electrons in these systems have been made clear by obtaining the cyclotron effective mass. Moreover, the unique dispersion of semi-Dirac systems makes it a suitable candidate for the development of high-speed electronics and opto-electronics devices, the advancement of topological quantum computing, and the design of innovative materials. This motivation led us to explore the topological properties in the semi-Dirac systems, as demonstrated in the subsequent chapters.

As a first problem, we have studied the Haldane model with deformable band properties in a honeycomb lattice in Chapter 2. We specifically focus on the evolution of the electronic spectrum and the topological characteristics. By introducing an anisotropy in hopping among certain nearest neighbours, we achieve tunable dispersion characteristics. We also observe a topological phase transition from a Chern insulating regime to a trivial insulating phase as the anisotropy is tuned beyond a certain value, which is known as the semi-Dirac limit ($t_1 = 2t$). The computation of the electronic dispersion demonstrates the movement and eventual merging of the Dirac points, resulting in the conduction and the valence bands touching each other at the M point in the BZ at ($t_1 = 2t$). Further, we have computed the density of states (DOS), which provides information about the distribution of energy levels in the system. We have also examined the evolution of Berry curvature and the Berry phase, which support our observed phase transition at the semi-Dirac limit. Furthermore, we have explored the behaviour of the edge modes, which are states localized at the edges of the nanoribbon, and found the existence of chiral edge modes as long as the non-trivial properties are preserved ($t_1 < 2t$). Finally, our calculations of anomalous Hall conductivity demonstrate the existence of the quantized plateaus below the semi-Dirac limit. The subsequent vanishing of these plateaus further supports the observed phase transition present therein [193, 200, 201].

In Chapter 3, we have focused on a semi-Dirac system ($t_1 = 2t$) that incorpo-

rates a real third neighbour (N3) hopping. The reason for the introduction of such longer range hopping is that the semi-Dirac system does not exhibit any non-trivial phase as shown in Chapter 2. We have observed that for a certain range of values of N3 hopping, the system shows higher Chern numbers $C = \pm 2$. This is because the dispersion spectrum demonstrates more number of band touching points (in absence of the Haldane term) inside the BZ and the TRS breaking Haldane term induces spectral gaps at these points. Further, to clarify the picture of non-trivial phases, we have demonstrated the Chern number phase diagram in various parameter spaces, which shows not only the $|C| = 2$ phase, but also the $|C| = 1$ phase. Our investigation of the edge states in a nanoribbon geometry shows either a pair or a single chiral edge modes, which confirms the value of the Chern number in the phase diagram. Additionally, we have calculated the anomalous Hall conductivity for various values of the hopping amplitudes and demonstrated the presence of Hall plateaus quantized at ne^2/h, where n denotes the number of edge modes crossing the Fermi energy [202]. Thus, our model in this Chapter provides a tool for obtaining higher Chern numbers. Such higher Chern numbers finds application in enabling robust and efficient electronic and photonic devices, spintronics, and quantum technologies.

Chapter 4 contains the work on the band-engineered bilayer Haldane system. A bilayer system, specifically the bilayer graphene is interesting since it has significant role in the field of optoelectronic, as it is suitable in photodetectors, LEDs, and solar cells. Also, bilayer graphene-based sensors offer high sensitivity and selectivity, and its inclusion in composites enhances mechanical, electrical, and thermal properties. This motivated us to study the bilayer graphene including a Haldane flux in this chapter, where the two layers have been coupled in such a way that the B sublattice of upper layer lies exactly above the A sublattice of lower layer. This type of arrangement is known as the AB stacking or the Bernal stacking. The dispersion spectrum shows the gap closing at the semi-Dirac limit ($t_1 = 2t$) identical to that of the monolayer system (shown in Chapter 2). However, because of the multiple bands, higher Chern numbers, $C = \pm 2$ have been observed, a feature that is absent in its monolayer counterpart. Interestingly, there is also a band specific behaviour. For example, the lower valence band acquires

only the $C = \pm 1$ phase, while the upper valence band has both $C = \pm 2$ and $C = \pm 1$ phases. The Chern number phase diagram shows multiple topological phase transitions with the Chern numbers changing from $2 \rightarrow 0 \rightarrow 1$, $2 \rightarrow -2$ etc. These phase transitions are supported by the opening and the closing of the energy gaps in the dispersion spectrum. Additionally, we have examined the band structure of a nanoribbon, which revealed the presence of a pair of chiral edge modes along the edges of the ribbon as long as t_1 remains less than $2t$. We have also analyzed the anomalous Hall conductivity and observed that the width of the quantized plateau at ne^2/h (n: number pf chiral edge modes) gradually decreases as t_1 is increased, eventually vanishing at $t_1 = 2t$. Thus, the bilayer Haldane model, similar to its monolayer counterpart, exhibits a topological phase transition at the semi-Dirac point. However, in the bilayer case, the Chern numbers are found to have larger values. Moreover, the edge modes are doubled in a nanoribbon, and the plateaus in the Hall conductivity are quantized at higher values, namely, at $2e^2/h$ [203].

The next chapter, that is, Chapter 5 is based on band-deformed dice lattice, including the Haldane term. The study of dice lattice is very important because the dispersion spectrum contains zero energy flat band where the electrons possess no kinetic energy (owing to its flatness) and hence the electrons do not contribute in transport properties. The flat band has several important consequences, including strong electron localization, electron-electron interactions and the emergence of correlated states. Motivated by the above scenario, in this chapter, we explore the topological properties and the phase transitions in dice lattice. We include the band deformation in a similar fashion as earlier. In particular, the band deformation is introduced via hopping anisotropies in two different ways (labelled them as case-I and case-II). In case-I, we have varied both the A-B hopping (t_1) and the B-C hopping (t'), resulting in the shifting of band extrema from the $\mathbf{K}$ and the $\mathbf{K}'$ points. This variation results in the band gap being diminished, ultimately leading to its closure at the semi-Dirac limit ($t_1 = t' = 2t$). In case-II, only the A-B hopping (t_1) has been varied, leading to dispersive flat bands. However, unlike case-I, the band extremum in case-II, located at one of the Dirac points, is slightly displaced, and the spectral gap closes earlier than the conventional semi-Dirac

limit, that is, at $t_1 = 1.67t$. The crucial point is that, both the cases exhibit Chern numbers of ± 2 until the gap closing transition occur, however, the topological lobes in the phase diagrams and the Hall conductivity have different structure in those two cases. The anomalous Hall conductivity displays quantized plateaus at $2e^2/h$ as long as t_1 and t' remain less than the semi-Dirac value of $2t$ in case-I. However, in case-II, due to the non-vanishing Berry curvature corresponding to the middle band, a dip in the plateau appears in the vicinity of Fermi energy for $t_1 \neq t$. The dip widens with the increase of t_1 and finally vanishes at $t_1 = 1.67t$ signalling the topological phase transition. Also, a pair of chiral edge modes in a nanoribbon has been observed in both the cases which vanishes at the gap closing points. This verifies the observed phase transition, where the Chern number, C drops from $\pm 2 \rightarrow 0$ at the gap closing hopping amplitudes [204].

Finally, we focus on the other class of topological insulators, namely, the quantum spin Hall (QSH) insulators. The QSH insulator has wide range of applications, such as, the spin-orbit torque device, magnetic field sensors owing to its spin-Hall magnetoresistance effect, spintronic devices, quantum computing systems etc. We have explored the topological properties of such a spin Hall insulator via studying the band-engineered Kane-Mele model in Chapter 6. The analysis of the spin resolved band dispersions reveal a migration of the band extrema from the Dirac points, eventually merge into one at the M point. Here the Chern number is zero owing to time-reversal symmetry. The $\mathbb{Z}_2$ topological invariant that characterizes the system, has a value '1', which vanishes at the gap closing semi-Dirac limit, that is, at $t_1 = 2t$. We demonstrate a phase diagram which encodes a gradual decrease in the topological regimes with the increase in t_1 and vanishes completely for $t_1 \geq 2t$. The system has no charge Hall conductivity, however, it has finite spin Hall conductivity. We have obtained a plateau quantized at $e/(2\pi)$ for $t_1 < 2t$. The plateau vanishes for $t_1 \geq 2t$ because of the phase transition occurring at $t_1 = 2t$. Finally, we have obtained the edge states in a ribbon geometry, which shows helical modes (as opposed to chiral ones) for $t_1 \leq 2t$. Therefore, the system exhibits a topological phase transition from a quantum spin Hall insulator to a trivial insulator at the semi-Dirac limit, which is supported by the computation of helical edge modes, $\mathbb{Z}_2$ invariant, and the spin

Hall conductivity [205].

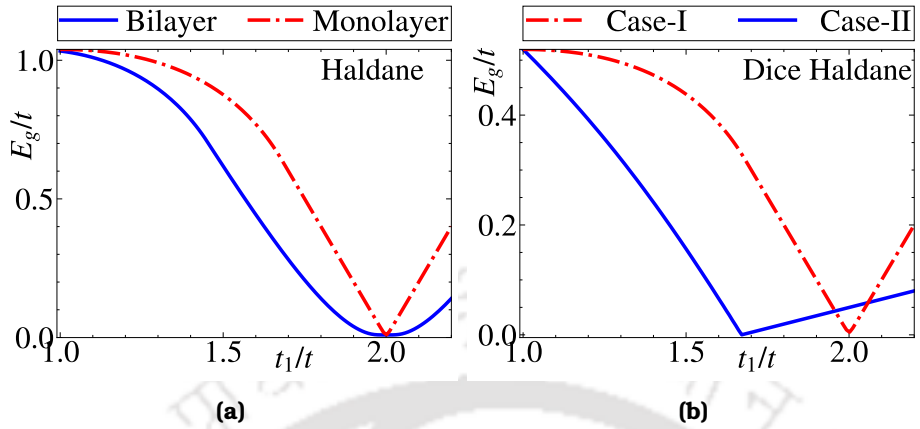

FIG. 7.1: The evolution of the band gap (E_g) as a function of t_1/t is shown for various systems. In (a), the red and blue curves correspond to the monolayer and bilayer Haldane models (discussed in Chapters 2 and 4) respectively. Further, (b) showcases the scenario for case-I (red) and case-II (blue) in the dice Haldane model (discussed in Chapters 5).

Although, in all of the systems, the spectral gap closes at a certain value of the anisotropy parameter, the band gap evolves in distinct ways as shown in Fig. 7.1. The variation of the band gap (E_g) corresponding to the Haldane model is presented in Fig. 7.1(a), where the two curves in different colors signify the bilayer and monolayer systems. As can be seen, both the monolayer and bilayer initially have the same magnitude of E_g at $t_1 = t$, but it deviates as t_1 is increased. In both the cases, E_g decreases slowly near $t_1 = t$ and rapidly drops in the vicinity of $t_1 = 2t$. Finally, the gap, E_g becomes zero at $t_1 = 2t$. The curve shape indicates that E_g varies linearly (almost) before reaching zero in the single layer case, while it deviates from being linear in the bilayer case. The more rapid variation of E_g in a bilayer Haldane may be related to a comparatively more drastic behaviour of the band structure induced by the interlayer coupling (hopping).

Additionally, Fig. 7.1(b) shows the variation of E_g for the dice lattice, with two different curves representing two cases of hopping anisotropies (case-I and case-II as defined in Chapter 5). Here E_g represents the magnitude of band gap between the flat band (or the middle band) and the valence band. The variation of E_g for case-I is identical to that of the monolayer Haldane model because, apart from the flat band, the band structures are same in both the cases. However, the scenario for case-II is significantly different. E_g decreases almost linearly as the

value of t_1 increases. E_g becomes zero at $t_1 = 1.67t$ and then becomes non-zero again. The gap-closing scenarios for the two cases indicate that the vanishing of band gap and hence the deformation of the band structure are not an universal phenomenon. The spectral gap may close at $t_1 = 2t$ for case-I or at $t_1 = 1.67t$ in case-II of the dice lattice, but the variations of E_g with respect to t_1/t differ. It should be noted that in the case of band deformed Kane-Mele model, the variation of E_g is identical to that of the monolayer Haldane model. Hence, we have skipped it for brevity.

Overall, our investigations pertaining to the evolution of electronic spectra and topological properties in these systems provided valuable insights into the behaviour of these systems under different conditions. The manipulation of hopping anisotropies and the introduction of Haldane flux allowed us to observe and analyze topological phase transitions, edge modes, anomalous Hall conductivity, and the spin Hall conductivity. These findings contribute to the fundamental understanding of topological insulators subjected to band deformation and may have potential applications in the development of electronic devices and technologies. Further, the scenario at the critical point ($t_1 = 2t$) could be interesting and may lead to potentially important outcome. Preliminary analysis reveals fractional Chern numbers at the critical point, however, the corresponding results need deeper scrutiny.

Appendices

Appendix A

Band Structure and Edge States of a Dice Lattice

A.1 Band structure: Analytic Expression

Here we show analytic calculations for the energy spectrum corresponding to the Hamiltonian in Eq. 5.2. We diagonalize the matrix which yields an eigenvalue equation of the form,

$$E^3 - (h_z^+ + h_z^-)E^2 + (h_z^+ h_z^- - |f_{xy}|^2 - |g_{xy}|^2)E + (h_z^+|g_{xy}|^2 + h_z^-|f_{xy}|^2) = 0 \quad \text{A.1}$$

where $f_{xy} = h_x(\mathbf{k}, t_1) - ih_y(\mathbf{k}, t_1)$ and $g_{xy} = h_x(\mathbf{k}, t') - ih_y(\mathbf{k}, t')$. Thus one gets a cubical equation, such as,

$$\xi_3 E^3 + \xi_2 E^2 + \xi_1 E + \xi_0 = 0 \quad \text{A.2}$$

with the coefficients ξ_i defined via,

$$\xi_0 = (h_z^+|g_{xy}|^2 + h_z^-|f_{xy}|^2),$$
$$\xi_1 = (h_z^+ h_z^- - |f_{xy}|^2 - |g_{xy}|^2)$$
$$\xi_2 = -(h_z^+ + h_z^-) \text{ and } \xi_3 = 1.$$

Transformation of Eq. A.2 into a depressed cubic equation by substituting $E = \bar{E} - \frac{\xi_2}{3\xi_3}$ will aid in its solution, and is given by,

$$\bar{E}^3 + \zeta_1 \bar{E} + \zeta_0 = 0 \tag{A.3}$$

where,

$$\zeta_1 = \frac{3\xi_3\xi_1 - \xi_2^2}{3\xi_3^2}, \text{ and } \zeta_0 = \frac{2\xi_2^3 + 27\xi_3^2\xi_0 - 9\xi_3\xi_2\xi_1}{27\xi_3^3}$$

For all values of $\mathbf{k}$, $\zeta_1 < 0$. Further, since all the roots of Eq. A.3 are real, the solutions are of the trigonometric form and can be written as,

$$\bar{E}_l = 2\sqrt{\frac{-\zeta_1}{3}} \cos\left\{\frac{1}{3}\cos^{-1}\left(\frac{3\zeta_0}{2\zeta_1}\sqrt{\frac{-3}{\zeta_1}}\right) - \frac{2\pi l}{3}\right\} \tag{A.4}$$

with $l = 0, 1$ and 2 are the indices corresponding to the conduction, middle and the valence bands respectively. Finally, the energy spectrum for different values of l are given by,

$$E_l = \bar{E}_l - \frac{\xi_2}{3\xi_3} \tag{A.5}$$

A.2 Edge States of a Dice Nanoribbon

In order to obtain the Hamiltonian for edge states, we first calculate the non-zero elements of the Hamiltonian corresponding to each atoms of the nanoribbon. Those atoms are denoted by n $(n = 1, 2, 3, ...N)$ as shown in Fig. A.1. Now, to find such non-zero elements, the following NN tight-binding eigenvalue equation can be used.

$$Eb_m = \sum_{(n,\mathbf{R})\in\sigma_m} t_{n,\mathbf{R}} b_n e^{i\,\mathbf{k}\cdot\mathbf{R}} \tag{A.6}$$

Now, we find the NN hoppings related to nth atom which we write as σ_n in the following fashion.

$$\begin{aligned}
\sigma_4 =&\{(8,0)t, (2,0)t, (6,\vec{a}_1)t_1\}, \{(3,0)t_c, (5,0)t_c, (9,0)t_c\}\\
\sigma_5 =&\{(7,0)t_c, (4,0)t_c, (1,0)t_c\}\\
\sigma_6 =&\{(1,0)t, (7,0)t, (4,-\vec{a}_1)t_1\}\\
\sigma_7 =&\{(12,0)t, (6,0)t, (8,0)t_1\}, \{(5,0)t_c, (11,0)t_c, (9,-\vec{a}_1)t_c\}\\
\sigma_8 =&\{(10,0)t, (4,0)t, (7,0)t_1\}\\
\sigma_9 =&\{(10,0)t_c, (4,0)t_c, (7,\vec{a}_1)t_c\}
\end{aligned} \tag{A.7}$$

where we have used the tuple notation $(m, \mathbf{R})$. For example, the 4th atom has six neighbours. Only one atom is located outside the region enclosed by the red dashed lines (lies beyond the red dashed line on the right hand side). However, because of the translational invariant along the x-direction, we can assume that 6th atom is equivalent to that one, the position should be transformed by $\vec{a}_1$. Hence, we have used the tuple $(6, \vec{a}_1)$ to denote such atom. The remaining five atoms are inside the unit cell which are denoted by $(m, 0)$. The respective hoppings are written outside each tuple. The NN hopping between the B and C sublattices is t_c which is different from the one used in Chapter 5 to distinguish it from the other hoppings for better understanding.

Now, the eigenvalue equation corresponding to σ_4 is given by,

$$E\,b_4 = t\,b_8 + t\,b_2 + t_1 e^{-ik_x a_1} b_6 + t_c(b_3 + b_5 + b_9). \tag{A.8}$$

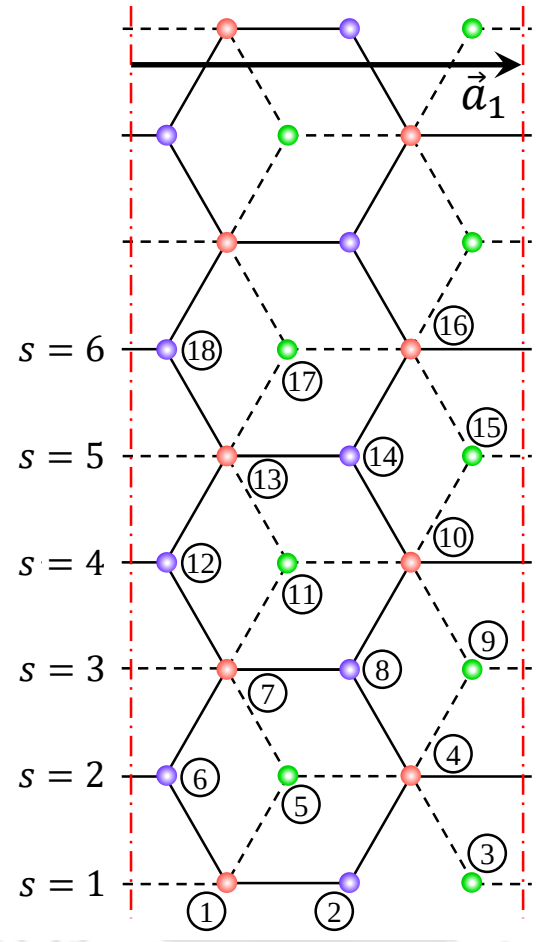

FIG. A.1: An armchair dice nanoribbon is depicted, which is infinite along the x-direction and finite along the y-direction. The A, B, and C sublattices are represented by blue, red, and green circles, respectively. The translational vector is denoted as $\vec{a}_1$. The section between the two red dashed lines is repeated on both sides of that section.

It can be noted that only the coefficient of b_6 is multiplied by $e^{-ik_x a_1}$, while the rest do not possess any exponential factor. For them $\vec{R} = 0$, which makes $e^{-ik_x|\vec{R}|} = 1$. The equations for other tuples can be written in the similar way and is skipped for brevity. Since, we have obtained all of the equations for each atoms, we can write the following equation.

$$H_{NN} \begin{bmatrix} b_1 \\ b_2 \\ b_3 \\ b_4 \\ \vdots \end{bmatrix} = E \begin{bmatrix} b_1 \\ b_2 \\ b_3 \\ b_4 \\ \vdots \end{bmatrix} \tag{A.9}$$

where the Hamiltonian H_{NN} is shown in table A.1. It may be noted that only 12 rows and columns are shown. The first six rows and columns repeat in the next six rows and columns, that is, $H_{NN}[i,j] = H_{NN}[i+6, j+6]$. This repetition is better clarified from Fig. A.1, where the 4th and 10th atoms, or the 5th and 11th atoms are located at an identical environment.

Now for the next nearest neighbour hopping, the following tuples can be obtained.

$$\begin{aligned}
\sigma_2 =& \{(6,0),(6,\vec{a}_1)\}e^{i\phi}, \quad \{(8,0)\}e^{-i\phi} \\
\sigma_3 =& \{(9,0)\}e^{i\phi}, \quad \{(5,0),(5,\vec{a}_1)\}e^{-i\phi} \\
\sigma_5 =& \{(11,0),(3,0),(3,-\vec{a}_1)\}e^{i\phi}, \quad \{(9,0),(9,-\vec{a}_1)\}e^{-i\phi} \\
\sigma_6 =& \{(8,0),(8,-\vec{a}_1)\}e^{i\phi}, \quad \{(12,0),(2,0),(2,-\vec{a}_1)\}e^{-i\phi}
\end{aligned} \tag{A.10}$$

Following the procedure for obtaining the NN Hamiltonian, the NNN Hamiltonian (H_{NNN}) of the dice nanoribbon have been obtained and shown in table A.2. The total Hamiltonian is $H_{NN} + H_{NNN}$ which can be diagonalize to calculate the edge states.

Further, we have demonstrated the coupled eigenvalue equations for a dice nanoribbon in Chapter 5 which were obtained by combining the eigenvalue equations for identical sublattices. For example, the equations for the 4th and 7th

TABLE. A.1: The Hamiltonian corresponding to the NN hopping (H_{NN}) is shown. Here $\rho = te^{-ika_1}$ and $\rho_1 = t_1 e^{-ika_1}$.

	1	2	3	4	5	6	7	8	9	10	11	12
1	0	t_1	ρ		t	t						
2	t_1	0	0	t		0	0					
3	ρ^*	0	0	t	0		0	0				
4		t	t	0	t	ρ_1^*		t	t			
5	t		0	t	0	0	t		0	0		
6	t	0		ρ_1	0	0	t	0		0	0	
7		0	0		t	t	0	t_1	ρ		t	t
8			0	t		0	t_1	0	0	t		0
9				t	0		ρ^*	0	0	t	0	
10					0	0		t	t	0	t	ρ_1^*
11						0	t		0	t	0	0
12							t	0		ρ_1		0

atoms (both belonging to sublattice B) are distinct, but can be expressed as a single equation:

$$E_k b_{k,s} = \left[t\left\{a_{k,s+1} + a_{k,s-1}\right\} + t_1 a_{k,s} e^{+i\eta_1 k}\right] + \left[tc_{k,s+1} + tc_{k,s-1} + t' c_{k,s} e^{-i\eta_2 k}\right] \tag{A.11}$$

where a, b and c refer to the coefficients corresponding to A, B, and C sublattices respectively. η_1 and η_2 are defined as $\eta_1 = \{1 + (-1)^s\}/2$ and $\eta_2 = \{1 + (-1)^{s+1}\}/2$ respectively. Here, s denotes the unit cell as shown in Fig. A.1. Hence, $s = 2$ and $s = 3$ in the above equation yield the equations for the 4th and 7th atoms respectively. Similarly, the equations for sublattices A and C can also be derived and are given in Eqs. 5.7 and 5.9 respectively.

TABLE. A.2: The Hamiltonian corresponding to the NNN hopping (H_{NNN}) is shown. Here $\alpha = t_2 e^{i\phi}$ and $\beta = (1 + e^{ika_1})$.

	1	2	3	4	5	6	7	8	9	10	11	12
1	0		0		0		0					
2		Δ		0		$\alpha\beta$		α^*				
3	0		$-\Delta$		$\alpha^*\beta$		0		α			
4		0		0		0		0		0		
5	0		$\alpha\beta^*$		$-\Delta$		0		$\alpha^*\beta^*$		α	
6		$\alpha^*\beta^*$		0		Δ		$\alpha\beta^*$		0		α^*
7			0		0		0		0		0	
8				0		$\alpha^*\beta$		Δ		0		$\alpha\beta$
9					$\alpha\beta$		0		$-\Delta$		$\alpha^*\beta$	
10						0		0		0		0
11							0		$\alpha\beta^*$		$-\Delta$	
12								$\alpha^*\beta^*$		0		Δ

Appendix B

Band-Engineered Kane-Mele Model

B.1 Low Energy Hamiltonian

Here we present the low energy Hamiltonian of the band-engineered Kane-Mele model. In order to do it, first we write the coefficients of each term on the right hand side of Eq. 6.2 as in the following,

$$\zeta_x = \alpha_0 + \alpha_x q_x + \alpha_y q_y + \alpha_{x^2} q_x^2 + \alpha_{y^2} q_y^2 + \alpha_{xy} q_x q_y \tag{B.1}$$

The other coefficients, namely, ζ_y, γ, ρ_x and ρ_y have similar forms. The coefficients of various terms associated with the momenta indices q_x and q_y for different values of t_1 are shown in Tables B.1-B.4.

TABLE. B.1: The coefficients, α_0, α_x, α_y, α_{x^2}, α_{y^2} and α_{xy} as appear in Eq. (B.1) corresponding to $t_1 = t$ (Dirac case) are shown.

	α_0	α_x	α_y	α_{x^2}	α_{y^2}	α_{xy}
ζ_x/t	0	1.5	0	0	0	0
ζ_y/t	0	0	1.5	0	0	0
$\gamma/\lambda_{\mathrm{SO}}$	$-3\sqrt{3}$	0	0	0	0	0
$\rho_x/(i\lambda_{\mathrm{SO}})$	1	0	0	0	0	0
$\rho_y/(i\lambda_{\mathrm{SO}})$	-1	0	0	0	0	0

TABLE. B.2: The coefficients, α_0, α_x, α_y, α_{x^2}, α_{y^2} and α_{xy} as appear in Eq. (B.1) corresponding to $t_1 = 1.5t$ are shown.

	α_0	α_x	α_y	α_{x^2}	α_{y^2}	α_{xy}
ζ_x/t	0	1.14567	0	0.5625	-0.5625	0
ζ_y/t	0	0.5728	-2.25	0	0	0
$\gamma/\lambda_{\mathrm{SO}}$	-4.6300	-3.0310	0	3.9686	2.9765	0
$\rho_x/(i\lambda_{\mathrm{SO}})$	1.75	-0.5728	$0.625i$	-0.2813	0.5938	$0.2864i$
$\rho_y/(i\lambda_{\mathrm{SO}})$	-1.1456	-1.125	$0.5728i$	0.4296	0.1432	$0.5625i$

TABLE. B.3: The coefficients, α_0, α_x, α_y, α_{x^2}, α_{y^2} and α_{xy} as appear in Eq. (B.1) corresponding to $t_1 = 1.8t$ are shown.

	α_0	α_x	α_y	α_{x^2}	α_{y^2}	α_{xy}
ζ_x/t	0	0.5408	0	0.7125	-0.7125	0
ζ_y/t	0	0	-2.85	0	0	0.2704
$\gamma/\lambda_{\mathrm{SO}}$	-2.4356	-6.0795	0	2.2482	1.4051	0
$\rho_x/(i\lambda_{\mathrm{SO}})$	1.9	-0.3775	$0.55i$	0.3375	0.6125	$0.1887i$
$\rho_y/(i\lambda_{\mathrm{SO}})$	-0.7549	-1.35	$0.3775i$	0.2832	0.0944	$0.675i$

TABLE. B.4: The coefficients, α_0, α_x, α_y, α_{x^2}, α_{y^2} and α_{xy} as appear in Eq. (B.1) corresponding to $t_1 = 1.9t$ are shown.

	α_0	α_x	α_y	α_{x^2}	α_{y^2}	α_{xy}
ζ_x/t	0	0.7549	0	0.675	-0.675	0
ζ_y/t	0	0	-2.7	0	0	0.3775
$\gamma/\lambda_{\mathrm{SO}}$	-3.3128	-5.2654	0	3.0076	1.9615	0
$\rho_x/(i\lambda_{\mathrm{SO}})$	1.95	-0.2701	$0.525i$	-0.3563	-0.6188	$0.1352i$
$\rho_y/(i\lambda_{\mathrm{SO}})$	-0.5408	-1.425	$0.2704i$	0.2028	0.0676	$0.7125i$

B.2 Edge States including the Rashba term

The Hamiltonian corresponding to the Rashba term defined in Eq. 6.1 is rewritten here.

$$H_R = i\lambda_{\rm R} \sum_{\langle ij \rangle} c_i^\dagger \left[s_y d_x^{ij} - s_x d_y^{ij} \right] c_j \tag{B.2}$$

For the first term on the right hand side, we find the following tuples.

$$\begin{aligned}
\sigma_2 &= \{(1,0)d_1^x, \quad (1,\vec{a})(d_1^x)\} \\
\sigma_3 &= \{(4,0)d_4^x, \quad (4,\vec{a})(d_4^x)\} \\
\sigma_4 &= \{(3,0)d_3^x, \quad (3,-\vec{a})(d_3^x)\} \\
\sigma_5 &= \{(6,0)d_6^x, \quad (6,-\vec{a})(d_6^x)\}
\end{aligned} \tag{B.3}$$

where σ_ns are written in the $(m, \vec{R})$ notation with m being the NN site corresponding to nth atom and $\vec{R}$ is the position of the site (see Fig. B.1). A detailed description to find such tuples has been illustrated in Sec. A.2. Here, the constants d_i^xs are given by,

$$d_1^x = d_4^x = -\sqrt{3}/2, \quad d_3^x = d_6^x = +\sqrt{3}/2$$

.

Similarly, for the second term, we find the following tuples.

$$\begin{aligned}
\sigma_2 &= \{(1,0)d_1^y, \quad (1,\vec{a})d_1^y, \quad (3,0)d_{32}^y\} \\
\sigma_3 &= \{(4,0)d_{43}^y, \quad (4,\vec{a})d_{43}^y, \quad (2,0)d_2^y\} \\
\sigma_4 &= \{(3,0)d_{34}^y, \quad (3,-\vec{a})d_{34}^y, \quad (5,0)d_5^y\} \\
\sigma_5 &= \{(6,0)d_6^y, \quad (6,-\vec{a})d_6^y, \quad (4,0)d_{45}^y\}
\end{aligned} \tag{B.4}$$

The values for d_i^ys are given by,

$$d_1^y = d_{34}^y = -1/2, \quad d_{43}^y = d_6^y = +1/2$$

$$d_{32}^y = d_5^y = 1, \quad d_2^y = d_{45}^y = -1$$

Using Eqs. B.3 and B.4, we can write the following eigenvalue equation.

$$E_R \begin{pmatrix} b_1 \\ b_2 \\ \vdots \end{pmatrix} = H_R \begin{pmatrix} b_1 \\ b_2 \\ \vdots \end{pmatrix} \tag{B.5}$$

where the Hamiltonian H_R is shown in Eq. B.6 with α being $(1 + \exp[-ik_x a_1])$.

$$H_{\mathrm{R}} = i\lambda_{\mathrm{R}} s_y \left(\frac{\sqrt{3}}{2}\right) \begin{pmatrix} 0 & \alpha & & & & & & \\ -\alpha^* & 0 & 0 & & & & & \\ & 0 & 0 & -\alpha^* & & & & \\ & & \alpha & 0 & 0 & & & \\ & & & 0 & 0 & \alpha & & \\ & & & & -\alpha^* & 0 & 0 & \\ & & & & & 0 & 0 & -\alpha^* \\ & & & & & & \alpha & 0 \end{pmatrix}$$

$$- i\lambda_{\mathrm{R}} s_x \begin{pmatrix} 0 & \frac{1}{2}\alpha & & & & & & \\ \frac{-1}{2}\alpha^* & 0 & 1 & & & & & \\ & -1 & 0 & \frac{1}{2}\alpha^* & & & & \\ & & \frac{-1}{2}\alpha & 0 & 1 & & & \\ & & & -1 & 0 & \frac{1}{2}\alpha & & \\ & & & & \frac{-1}{2}\alpha^* & 0 & 1 & \\ & & & & & -1 & 0 & \frac{1}{2}\alpha^* \\ & & & & & & \frac{-1}{2}\alpha & 0 \end{pmatrix} \tag{B.6}$$

Here only an 8×8 matrix is shown. If we consider a ribbon with N atoms, the matrix size would be $2N \times 2N$, where the factor '2' arises to account for the

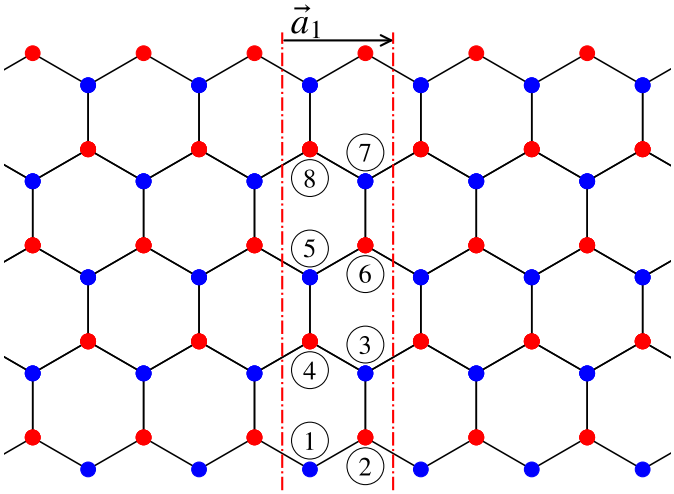

FIG. B.1: A zigzag honeycomb nanoribbon is depicted. The section between the two red dashed lines repeats on both the right and left hand sides of that section. The translational vector is denoted by $\vec{a}_1$.

presence of spin-$1/2$ Pauli matrices s_x and s_y. The Hamiltonian associated with the NN and NNN hoppings can also be obtained using a similar approach (see Sec. A.2). The eigenvalues of the total Hamiltonian are plotted as a function of k_x in Fig. 6.3.

Bibliography

[1] K. v. Klitzing, G. Dorda, and M. Pepper, Phys. Rev. Lett. **45**, 494 (1980).

[2] D. J. Thouless, M. Kohmoto, M. P. Nightingale, and M. den Nijs, Phys. Rev. Lett. **49**, 405 (1982).

[3] D. J. Thouless, Phys. Rev. B **27**, 6083 (1983).

[4] J. E. Avron, R. Seiler, and B. Simon, Phys. Rev. Lett. **51**, 51 (1983).

[5] M. Kohmoto, Ann. Phys. (Berlin) **160**, 343 (1985).

[6] Q. Niu, D. J. Thouless, and Yong-ShiWu, Phys. Rev. B **31**, 3372 (1985).

[7] R. E. Prange and S. M. Girvin (eds.), *The Quantum Hall Effect* (Springer-Verlag, Berlin, 1990).

[8] R. B. Laughlin, Phys. Rev. B **23**, 5632(R) (1981).

[9] S. A. Trugman, Phys. Rev. B **27**, 7539 (1983).

[10] S. Ilani, J. Martin, E. Teitelbaum, J. H. Smet, D. Mahalu, V. Umansky, and A. Yacoby, Nature **427**, 328 (2004).

[11] P. Vasilopoulos, Phys. Rev. B **32**, 771 (1985).

[12] C. -Z. Chang *et al*, Science **340**, 167 (2013).

[13] C. Z. Chang, W. Zhao, D. Kim, *et al*. Nature Mater **14**, 473 (2015).

[14] Y. Deng, Y. Yu, M. Z. Shi, Z. Guo, Z. Xu, J. Wang, X. H. Chen, Y. Zhang, Science **367**, 895 (2020).

[15] N. Nagaosa, J. Sinova, S. Onoda, A. H. MacDonald, and N. P. Ong Rev. Mod. Phys. **82**, 1539 (2010).

[16] F. D. M. Haldane, Phys. Rev. Lett. **61**, 2015 (1988).

[17] M. Z. Hasan and C. L. Kane, Rev. Mod. Phys. **82**, 3045 (2010).

[18] Y. Ando, J. Phys. Soc. Jpn. **82**, 102001 (2013).

[19] X.-L. Qi and S.-C. Zhang, Rev. Mod. Phys. **83**, 1057 (2011).

[20] J. E. Moore, Nature (London) **464**, 194 (2010).

[21] M. V. Berry, Proc. R. Soc. A **392**, 45 (1984).

[22] C. Weeks and M. Franz, Phys. Rev. B **82**, 085310 (2010).

[23] V. Apaja, M. Hyrkäs, and M. Manninen, Phys. Rev. A **82**, 041402(R) (2010).

[24] N. Goldman, D. F. Urban, and D. Bercioux, Phys. Rev. A **83**, 063601 (2011).

[25] W. -F. Tsai, C. Fang, H. Yao, and J. Hu, New J. Phys. **17**, 055016 (2015).

[26] K. Sun, H. Yao, E. Fradkin, and S. A. Kivelson Phys. Rev. Lett. **103**, 046811 (2009).

[27] K Ohgushi, S. Murakami, and N. Nagaosa, Phys. Rev. B **62**, R6065(R) (2000).

[28] Y. Xiao, V. Pelletier, P. M. Chaikin, and D. A. Huse, Phys. Rev. B **67**, 104505 (2003).

[29] H. -M. Guo and M. Franz, Phys. Rev. B **80**, 113102 (2009).

[30] X. -P. Liu, W. -C. Chen, Y. -F. Wang and C. -D. Gong J. Phys. Condens. Matter **25**, 305602 (2013).

[31] A. Wright, Sci. Rep. **3**, 2736 (2013).

[32] Y. Ding, Y. Peng, Y. Zhu, X. Fan, J. Yang, B. Liang, X. Zhu, X. Wan, and J. Cheng, Phys. Rev. Lett. **122**, 014302 (2019).

[33] H. S. Kim and H. Y. Kee, npj Quant Mater **2**, 20 (2017).

[34] K. F. Garrity and D. Vanderbilt, Phys. Rev. B **90**, 121103(R) (2014).

[35] L. B. Shao, S. -L. Zhu, L. Sheng, D. Y. Xing, and Z. D. Wang, Phys. Rev. Lett. **101**, 246810 (2008).

[36] E. Alba, X. F. -Gonzalvo, J. M. -Petit, J. K. Pachos, and J. J. G. -Ripoll, Phys. Rev. Lett. **107**, 235301 (2011).

[37] L. Tarruell, D. Greif, T. Uehlinger, G. Jotzu and T. Esslinger, Nature **483**, 302 (2012).

[38] G. Jotzu, M. Messer, R. Desbuquois, M. Lebrat, T. Uehlinger, D. Greif and T. Esslinger, Nature **515**, 237 (2014).

[39] T. Andrijauskas, E. Anisimovas, M. Račiūnas, A. Mekys, V. Kudriašov, I. B. Spielman, and G. Juzeliūnas Phys. Rev. A **92**, 033617 (2015).

[40] P. Dietl, F. Pichon, and G. Montambaux, Phys. Rev. Lett. **100**, 236405 (2008).

[41] S. Banerjee, R. R. P. Singh, V. Pardo, and W. E. Pickett, Phys. Rev. Lett. **103**, 016402 (2009).

[42] V. Pardo and W.E. Pickett, Phys. Rev. Lett. **102**, 166803 (2009).

[43] V. Pardo, W.E. Pickett, Phys. Rev. B **81**, 035111 (2010).

[44] A. N. Rudenko, Shengjun Yuan, and M. I. Katsnelson, Phys. Rev. B **92**, 085419 (2015).

[45] C. Dutreix, E. A. Stepanov, and M. I. Katsnelson, Phys. Rev. B **92**, 241404(R) (2016).

[46] A. S. Rodin, A. Carvalho, and A. H. Castro Neto, Phys. Rev. Lett. **112**, 176801 (2014).

[47] A. S. Rodin, A. Carvalho, and A. H. Castro Neto, Phys. Rev. Lett. **112**, 176801 (2014).

[48] J. Guan, Z. Zhu, and D. Tománek, Phys. Rev. Lett. **113**, 046804 (2014).

[49] G. Montambaux, F. Piéchon, J.-N. Fuchs, and M. O. Goerbig, Phys. Rev. B **80**, 153412 (2009).

[50] Y. Suzumura, T. Morinari, and F. Piéchon, J. Phys. Soc. Jpn. **82**, 023708 (2013).

[51] Y. Hasegawa, R. Konno, H. Nakano, and M. Kohmoto, Phys. Rev. B **74**, 033413 (2006).

[52] C. Zhong, Y. Chen, Y. Xie, Y.-Y. Sun, and S. Zhang, Phys. Chem. Chem. Phys. **19**, 3820 (2017).

[53] J. Kim, S. S. Baik, S. H. Ryu, Y. Sohn, S. Park, B.-G. Park, J. Denlinger, Y. Yi, H. J. Choi, and K. S. Kim, Science **349**, 723 (2015).

[54] J. P. Carbotte, K. R. Bryenton, and E. J. Nicol Phys. Rev. B **99**, 115406 (2019).

[55] A. Mawrie and B. Muralidharan, Phys. Rev. B **99**, 075415 (2019).

[56] A. Narayan, Phys. Rev. B **91**, 205445 (2015).

[57] Q. Chen, L. Du, and G. Fiete, Phys. Rev. B **97**, 035422 (2018).

[58] S. K. F. Islam and A. Saha, Phys. Rev. B **98**, 235424 (2018).

[59] I. Mandal and K. Saha, Phys. Rev. B **101**, 045101 (2020).

[60] S. Banerjee and W.E. Pickett, Phys. Rev. B **86**, 075124 (2012).

[61] X. Y. Zhou, R. Zhang, J. P. Sun, Y. L. Zou, D. Zhang, W. K. Lou, F. Cheng, G. H. Zhou, F. Zhai, and K. Chang, Sci. Rep. **5**, 12295 (2015).

[62] S. Yuan, E. v. Veen, M. I. Katsnelson, and R. Roldan, Phys. Rev. B **93**, 245433

(2016).

[63] P. Sinha, S. Murakami and S. Basu, Phys. Rev. B **102**, 085416 (2020).

[64] Z. Ni, E. Minamitani, Y. Ando, and S. Watanabe, Phys. Rev. B 96, 075427 (2017)

[65] N. B. M. Schröter, M. D. Watson, L. B. Duffy, M. Hoesch, Y. Chen, T. Hesjedal and T. K. Kim, 2D Mater. **4** 031005 (2017).

[66] L. Wu, P. Lu, J. Bi, C. Yang, Y. Song, P. Guan and S. Wang, Nanoscale Res Lett **11**, 525 (2016).

[67] R. H. Baughman and H. Eckhardt, J. Chem. Phys. **87**, 6687 (1987).

[68] K. Zieglar and A. Sinner, EPL, **119**, 27001 (2017).

[69] P. Delplace and G. Montambaux, Phys. Rev. B **82**, 035438 (2010).

[70] D. Sticlet, F. Piéchon, J.-N. Fuchs, P. Kalugin, and P. Simon, Phys. Rev. B **85**, 165456 (2012).

[71] W. -C. Chen, R. Liu, Y. -F. Wang, and C. -D. Gong, Phys. Rev. B **86**, 085311 (2012).

[72] S. Yang, Z. -C. Gu, K. Sun, and S. D. Sarma, Phys. Rev. B **86**, 241112(R) (2012).

[73] Y. Yang, Y. F. Zhang, L. Sheng and D. Y. Xing, EPL **105**, 27005 (2014).

[74] Y. Yang, X. Li, and D. Xing, Eur. Phys. J. B **89**, 217 (2016).

[75] A. Alase and D. L. Feder, Phys. Rev. A **103**, 053305 (2021).

[76] M. Lacki, J. Zarkrzewski and N. Goldman, SciPost Phys. **10**, 112 (2021).

[77] C. Fang, M. J. Gilbert, and B. A. Bernevig, Phys. Rev. Lett. **112**, 046801 (2014).

[78] J. Wang, B. Lian, H. Zhang, Y. Xu, and S.-C. Zhang Phys. Rev. Lett. **111**, 136801 (2013).

[79] H. Zhao, T. Zhang, X. Zhang, M. -H. Lu, Y. -F. Chen, Front. Phys. 10 (2022).

[80] Y. F. Zhao, R. Zhang, R. Mei, L. Zhou, H. Yi, Y. Q. Zhang, J. Yu, R. Xiao, K. Wang, N. Samarth, M. H. W. Chan, C. X. Liu, and C. Z. Chang, Nature (London) **588**, 419 (2020).

[81] W. Zhu, C. Song, H. Bai, L. Liao, and F. Pan Phys. Rev. B **105**, 155122 (2022).

[82] J. Ge, Y. Liu, J. Li, H. Li, T. Luo, Y. Wu, Y. Xu, J. Wang National Science

Review **8**, 1280 (2020).

[83] S. Spurrier and N. R. Cooper, Phys. Rev. Research **2**, 033071 (2020).

[84] P. Cheng, P. W. Klein, K. Plekhanov, K. Sengstock, M. Aidelsburger, C. Weitenberg, and K. Le. Hur, Phys. Rev. B **100**, 081107(R) (2019).

[85] S. Sorn, Phys. Rev. B 98, 125145 (2018).

[86] J. Panas, B. Irsigler, J.-H. Zheng, and W. Hofstetter, Phys. Rev. B **102**, 075403 (2020).

[87] Y. Xiao, J. Liu, and L. Fu, Matter **3**, 1142 (2020).

[88] Y. -Z. You and A. Vishwanath, npj Quantum Mater. **4**, 16 (2019).

[89] Q. Tong, H. Yu, Q. Zhu, Y. Wang, X. Xu, and W. Yao, Nature Phys **13**, 356 (2017).

[90] C. N. Lau, M. W. Bockrath, K. F. Mak, and F. Zhang, Nature **602**, 41 (2022).

[91] E. Y. Andrei, D. K. Efetov, P. J. Herrero, A. H. MacDonald, K. F. Mak, T. Senthil, E. Tutuc, A. Yazdani, and A. F. Young, Nat Rev Mater **6**, 201 (2021).

[92] B. Dey, P. Kapri, O. Pal, and T. K. Ghosh, Phys. Rev. B **101**, 235406 (2020).

[93] B. Sutherland, Phys. Rev. B **34**, 5208 (1986).

[94] J. Vidal, R. Mosseri, and B. Doucot, Phys. Rev. Lett. **81**, 5888 (1998).

[95] S. E. Korshunov, Phys. Rev. B **63**, 134503 (2001).

[96] M. Rizzi, V. Cataudella, and R. Fazio, Phys. Rev. B **73**, 144511 (2006).

[97] A. A. Burkov and E. Demler Phys. Rev. Lett. **96**, 180406 (2006).

[98] D. Bercioux, D. F. Urban, H. Grabert, and W. Hausler, Phys. Rev. A **80**, 063603 (2009).

[99] D. Bercioux, N. Goldman, and D. F. Urban, Phys. Rev. A **83**, 023609 (2011).

[100] G. Möller and N. R. Cooper, Phys. Rev. Lett. **108**, 045306 (2012).

[101] M. Vigh, L. Oroszlány, S. Vajna, P. San-Jose, G. Dávid, J. Cserti, and B. Dora, Phys. Rev. B **88**, 161413(R) (2013).

[102] J. D. Malcolm and E. J. Nicol, Phys. Rev. B **93**, 165433 (2016).

[103] H. Aoki, M. Ando, and H. Matsumura, Phys. Rev. B **54**, R17296(R) (1996).

[104] R. Khomeriki and S. Flach, Phys. Rev. Lett. **116**, 245301 (2016).

[105] Y. Cao, V. Fatemi, S. Fang, K. Watanabe, T. Taniguchi, E. Kaxiras and P. J. -Herrero, Nature **556**, 43{50 (2018).

[106] C. Wu, D. Bergman, L. Balents, and S. D. Sarma Phys. Rev. Lett. **99**, 070401

(2007).

[107] T. T. Heikkilä, and G. E. Volovik, *Basic Physics of Functionalized Graphite* Springer, (2016).

[108] E. Tang, J. -W. Mei, and X. -G. Wen, Phys. Rev. Lett. **106**, 236802 (2011).

[109] K. Sun, Z. Gu, H. Katsura, and S. D. Sarma Phys. Rev. Lett. **106**, 236803 (2011).

[110] S. Mukherjee, A. Spracklen, D. Choudhury, N. Goldman, P. Öhberg, E. Andersson, and R. R. Thomson, Phys. Rev. Lett. **114**, 245504 (2015).

[111] M. Hyrkäs, V. Apaja, and M. Manninen, Phys. Rev. A **87**, 023614 (2013).

[112] Y. Nakata, T. Okada, T. Nakanishi, and M, Kitano, Phys. Rev. B **85**, 205128 (2012).

[113] C. L. Kane and E. J. Mele, Phys. Rev. Lett. **95**, 146802 (2005).

[114] C. L. Kane and E. J. Mele, Phys. Rev. Lett. **95**, 226801 (2005).

[115] E. I. Rashba, Sov. Phys. Solid State **2**, 1109 (1960).

[116] E. A. de Andrada e Silva, G. C. La Rocca, and F. Bassani, Phys. Rev. B **55**, 16293 (1997).

[117] E. A. de Andrada e Silva, G. C. La Rocca, and F. Bassani, Phys. Rev. B **50**, 8523 (1994).

[118] G. Engels, J. Lange, T. Schäpers, and H. Lüth Phys. Rev. B **55**, R1958 (1997).

[119] J. Nitta, T. Akazaki, H. Takayanagi, and T. Enoki, Phys. Rev. Lett. **78**, 1335 (1997).

[120] D. Liang and X. P.A. Gao, Nano Lett. **12**, 3263 (2012).

[121] D. Frustaglia and K. Richter, Phys. Rev. B **69**, 235310 (2004).

[122] R. Ionicioiu and I. D'Amico, Phys. Rev. B **67**, 041307(R) (2003).

[123] S. Datta and B. Das, Appl. Phys. Lett. **56**, 665 (1990).

[124] M. Gmitra and J. Fabian Phys. Rev. B **92**, 155403 (2015)

[125] M. Peralta, L. Colmenarez, A. López, B. Berche, and E. Medina, Phys. Rev. B **94**, 235407 (2016).

[126] Z. Qiao, S. A. Yang, W. Feng, W.-K. Tse, J. Ding, Y. G. Yao, J. Wang, and Q. Niu, Phys. Rev. B **82**, 161414(R) (2010).

[127] A. López, L. Colmenárez, M. Peralta, F. Mireles, and E. Medina, Phys. Rev.

B **99**, 085411 (2019).

[128] M. Peralta, E. Medina, and F. Mireles, Phys. Rev. B **99**, 195452 (2019).

[129] A. Varykhalov, J. S.-Barriga, A. M. Shikin, C. Biswas, E. Vescovo, A. Rybkin, D. Marchenko, and O. Rader, Phys. Rev. Lett. **101**, 157601 (2008).

[130] D. Marchenko, A. Varykhalov, M. R. Scholz, G. Bihlmayer, E. I. Rashba, A. Rybkin, A. M. Shikin and O. Rader, Nat Commun **3**, 1232 (2012)

[131] M. Krivenkov, E. Golias, D. Marchenko, J. S.-Barriga, G. Bihlmayer, O. Rader, and A Varykhalov, 2D Mater. **4** 035010 (2017).

[132] M. M. Otrokov, I. I. Klimovskikh, F. Calleja, A. M. Shikin, O. Vilkov, A. G. Rybkin, D. Estyunin, S. Muff, J. H. Dil, A. L. V. de Parga, R. Miranda, H. Ochoa, F. Guinea, J. I. Cerdá, E. V. Chulkov, and A Arnau, 2D Mater. **5** 035029 (2018).

[133] O. Rader, A. Varykhalov, J. S´anchez-Barriga, D. Marchenko, A. Rybkin, and A. M. Shikin, Phys. Rev. Lett. **102**, 057602 (2009).

[134] B. A. Bernevig T. L. Hughes and S. C. Zhang, Science **314** 1757-1761 (2006).

[135] M. König, S. Wiedmann, C. Brüne, A. Roth, H. Buhmann, L. W. Molenkamp, X.-L. Qi, and S.-C. Zhang, Science **318**, 766 (2007).

[136] N. P. Stern, S. Ghosh, G. Xiang, M. Zhu, N. Samarth, and D. D. Awschalom, Phys. Rev. Lett. **97**, 126603 (2006).

[137] T. Seki, Y. Hasegawa, S. Mitani, S. Takahashi, H. Imamura, S. Maekawa, J. Nitta and K. Takanashi, Nature Mater **7**, 125 (2008).

[138] T. Kimura, Y. Otani, T. Sato, S. Takahashi, and S. Maekawa, Phys. Rev. Lett. **98**, 156601, (2007).

[139] H. Zhao, E. J. Loren, H. M. van Driel, and A. L. Smirl Phys. Rev. Lett. **96**, 246601 (2006).

[140] M. Isasa, E. Villamor, L. E. Hueso, M. Gradhand, and F. Casanova Phys. Rev. B **91**, 024402 (2015).

[141] D. J. Thouless, *Topological Quantum Numbers in Nonrelativistic Physics* (World Scientific, Singapore, 1998).

[142] J. E. Avron, L. Sadun, J. Segert, and B. Simon, Phys. Rev. Lett. **61**, 1329 (1988).

[143] C. -X. Liu, S. -C. Zhang, and X. -L. Qi Annu. Rev. Condens. Matter Phys. **7** 301 (2016).

[144] W. -Y. Hsiang and D. -H. Lee, Phys. Rev. A **64**, 052101 (2001).

[145] T. Fukui, Y. Hatsugai and H. Suzuki, J. Phys. Soc. Jpn. **74**, 1674 (2005).

[146] C. L. Kane, *Contemporary Concepts of Condensed Matter Science,* Elsevier **6**, 3 (2013).

[147] L. Fu and C. L. Kane, Phys. Rev. B **74**, 195312 (2006).

[148] S. -C. Zhang and J. Hu, Science **294**, 823 (2001).

[149] G. E. Volovik, *The Universe in a Helium Droplet*, Clarendon, Oxford (2003).

[150] G. E. Volovik, Jetp Lett. **90**, 587 (2009).

[151] R. Roy, arXiv:0803.2868 (2008).

[152] A. P. Schnyder, S. Ryu, A. Furusaki, and A. W. W. Ludwig, Phys. Rev. B **78**, 195125 (2008).

[153] Y. Nagato, S. Higashitani, and K. Nagai, J. Phys. Soc. Jpn. **78**, 123603 (2009).

[154] X. -L. Qi, T. L. Hughes, S. Raghu, and S. -C. Zhang, Phys. Rev. Lett. **102**, 187001 (2009).

[155] W. P. Su, J. R. Schrieffer, and A. J. Heeger, Phys. Rev. Lett. **42**, 1698 (1979).

[156] S. Ono, H. C. Po, and K. Shiozaki, Phys. Rev. Research **3**, 023086 (2021).

[157] M. Z. Hasan and C. L. Kane, Rev. Mod. Phys. **82**, 3045 (2010).

[158] A. Altland and M. R. Zirnbauer Phys. Rev. B **55**, 1142 (1997).

[159] D. J. Griffiths, *Introduction to Quantum Mechanics*, Prentice-Hall, New Jersey, 1994.

[160] W. Greiner, *Relativistic quantum mechanics*, Springer, Germany, 1987.

[161] R. Winkler, *Spin-Orbit Coupling effects in Two-Dimensional Electron and Hole Systems*, Springer, Germany, 2003.

[162] M. I. D'yakonov, Sov. Phys. Semicond. **20**, 110 (1986).

[163] N. A. Sinitsyn, E. M. Hankiewicz, W. Teizer, and J. Sinova, Phys. Rev. B **70**, 081312(R) (2004).

[164] D. Bercioux and P. Lucignano, Rep. Prog. Phys. **78**, 106001 (2015).

[165] D. Xiao, M.-C. Chang, and Q. Niu, Rev. Mod. Phys. **82**, 1959 (2010).

[166] D. Culcer, A.MacDonald, and Q. Niu, Phys. Rev. B **68**, 045327 (2003).

[167] K. Saha, Phys. Rev. B **94**, 081103(R) (2016).

[168] K. S. Novoselov, A. K. Geim, S. V. Morozov, D. Jiang, Y. Zhang, S. V. Dubonos, I. V. Grigorieva, and A. A. Firsov Science **306**, 666-669 (2004).

[169] T. Shao, B. Wen, R. Melnik, S. Yao, Y. Kawazoe, and Y. Tian, J. Chem. Phys. **137**, 194901 (2012).

[170] A. A. Balandin, S. Ghosh, W. Bao, I. Calizo, D. Teweldebrhan, F. Miao, and C. N. Lau Nano Lett. **8**, 902 (2008).

[171] K. S. Novoselov, A. K. Geim, S. V. Morozov, D. Jiang, M. I. Katsnelson, I. V. Grigorieva, S. V. Dubonos, and A. A. Firsov, Nature **438**, 197 (2005).

[172] F. Schwierz, Nature Nanotech **5**, 487 (2010).

[173] Y.-M. Lin, A. Valdes-Garcia, S.-J. Han, D. B. Farmer, I. Meric, Y. Sun, Y. Wu, C. Dimitrakopoulos, A. Grill, P. Avouris, and K. A. Jenkins, Science, **332**, 1294 (2010).

[174] G. Eda and M. Chhowalla, Adv. Mater. **22**, 2392 (2010).

[175] F. Bonaccorso, Z. Sun, T. Hasan, and A. C. Ferrari, Nature Photon **4**, 611 (2010).

[176] R. Raccichini, A. Varzi, S. Passerini, and B. Scrosati, Nature Mater **14**, 271 (2015).

[177] T. Kuila, S. Bose, P. Khanra, A. K. Mishra, N. H. Kim, and J. H. Lee, Biosens. Bioelectron. **26**, 4637 (2011).

[178] M. F. El-Kady, Y. Shao, and R. B. Kaner, Nat Rev Mater **1**, 16033 (2016).

[179] D. C. Elias, R. R. Nair, T. M. G. Mohiuddin, S. V. Morozov, P. Blake, M. P. Halsall, A. C. Ferrari, D. W. Boukhvalov, M. I. Katsnelson, A. K. Geim, and K. S. Novoselov, Science **323**, 610 (2009).

[180] Sayan Mondal, Sudin Ganguly, and Saurabh Basu, *Topology and applications of 2D Dirac and semi-Dirac materials*, De Gruyter, (2023).

[181] N. W. Ashcroft and N. D. Mermin, *Solid State Physics* (Saunders College, Philadelphia, PA, 1976)

[182] O. Ciftja, V. Livingston, and E. Thomas, Am. J. Phys. **85**, 359 (2017).

[183] S. Bhandari, G.-H. Lee, A. Klales, K. Watanabe, T. Taniguchi, E. Heller, P. Kim, and M. Westervelt, Nano Lett. 2016, 16, 3, 1690{1694

[184] A. H. Castro Neto, F. Guinea, N. M. R. Peres, K. S. Novoselov, and A. K.

Geim, Rev. Mod. Phys. **81**, 109 (2009).

[185] K. Nakada, M. Fujita, G. Dresselhaus, and M. S. Dresselhaus, Phys. Rev. B **54**, 17954 (1996).

[186] P. Sinha, S. Ganguly and S. Basu, Physica E **103**, 314 (2018).

[187] T. Thonhauser and D. Vanderbilt, Phys. Rev. B **74**, 235111 (2006).

[188] G. Semenoff, Phys. Rev. Lett. **53**, 2449 (1984).

[189] Y. Hatsugai Phys. Rev. B **48**, 11851 (1988).

[190] S. Saha, T. Nag, and S. Mandal, Phys. Rev. B **103**, 235154 (2021).

[191] C. Bena and L. Simon, Phys. Rev. B **83**, 115404 (2011).

[192] D. Sticlet and F. Piéchon, Phys. Rev. B **87**, 115402 (2013).

[193] S. Mondal, P. Kapri, B. Dey, T. K. Ghosh, and S. Basu, J. Phys.: Condens. Matter **33**, 225504, (2021).

[194] M. Mannaï, J. -N. Fuchs, F. Piéchon, and S. Haddad Phys. Rev. B **107**, 045117 (2023).

[195] A. C. Aitken, *Determinants and Matrices*. Edinburgh: Oliver and Boyd, 1939.

[196] M. I. Krivoruchenko, Mathematics and Computer Science, **1**, 21-28, (2016).

[197] R. Raimondi and P. Schwab, Phys. Rev. B **71**, 033311 (2004)

[198] T. Tanaka, H. Kontani, M. Naito, T. Naito, D. S. Hirashima, K. Yamada, and J. Inoue Phys. Rev. B **77**, 165117 (2008)

[199] K. Taguchi, D. Oshima, Y. Yamaguchi, T. Hashimoto, Y. Tanaka, and M. Sato, Phys. Rev. B 101, 235201 (2020).

[200] S. Mondal and S. Basu, Eur. Phys. J. B **94**, 207 (2021).

[201] S. Mondal and S. Basu, Physica E **138**, 115048 (2022).

[202] S. Mondal and S. Basu, Phys. Rev. B **105**, 235409 (2022).

[203] S. Mondal and S. Basu, arXiv:2304.02880.

[204] S. Mondal and S. Basu, Phys. Rev. B **107**, 035421 (2023).

[205] S. Mondal and S. Basu, Phys. Rev. B **105**, 235441 (2022).

Vita

Sayan Mondal was born on 5th January 1995 in West Bengal, India. He completed his B.Sc. with Physics Honours in 2012 from Abhedananda Mahavidyalaya, Sainthia, under University of Burdwan and M.Sc. in physics from the Indian Institute of Technology Kharagpur in 2017. He had enrolled into the Ph.D programme at Indian Institute of Technology Guwahati in 2018 (July). He had qualified for CSIR-UGC NET in June 2016 and December 2018, Joint entrance screening test (JEST) in 2017 and 2018, and Graduate Aptitude Test in Engineering (GATE) in 2017 and 2018.